

**Graduate thesis**

Aadne Eide

# Structural damping estimation for floating welded steel structures

Graduate thesis in Marine Technology  
January 2022

**NTNU**  
Norwegian University of Science and Technology  
Faculty of Engineering  
Department of Marine Technology



Norwegian University of  
Science and Technology



Aadne Eide

# **Structural damping estimation for floating welded steel structures**

Graduate thesis in Marine Technology  
January 2022

Norwegian University of Science and Technology  
Faculty of Engineering  
Department of Marine Technology







## **MASTER THESIS WORK SPRING 2022**

**for**

**Stud. Tech. Aadne Eide**

### **Structural damping estimation for floating welded steel structures**

*Estimering av strukturdemping for flytende sveiste stålkonstruksjoner*

For large floating structures for aquaculture, transportation, and energy harvesting at sea, good estimates of damping are needed in order to accurately predict resonant responses across the wide range of frequencies that could be excited. In addition to hydrodynamic damping, aerodynamic damping, and soil damping, contributions from structural (or material) damping may also be significant. Rules of thumb are often used when setting the value of this damping in dynamic analysis, without a strong basis in empirical results or material models. There is thus a knowledge gap related to damping in welded steel shell structures relevant for many marine technology applications. The master thesis work is intended to investigate this knowledge gap and improve understanding of structural damping. The master thesis work is to be carried out as a continuation of the project performed during Fall 2021 as follows:

1. Supplementary literature review regarding empirical and numerical approaches for estimating structural (material) damping, hydrodynamic damping, and soil damping, provided values for structural damping in design standards, and structural damping for similar structures. This also includes available full-scale data and existing numerical models of the full scale structure, and estimation of uncertainty in sources of damping.
2. On the basis of the laboratory test procedure proposed during the project which could improve the understanding of material damping and the effect of welds for relevant full-scale structures, perform laboratory test to estimate the structural damping for different support conditions in terms of weld geometries. Assess the repeatability and uncertainties in the laboratory experiment.
3. Based on further developing the FE model established during the project period, perform simulations of the experimental setup and correlation analyses to understand and explain the observed damping performance.
4. Propose a procedure for estimating structural damping parameters based on numerical/analytical approaches supported by small- or mid-scale testing.
5. Conclusions and recommendations for further work.

The work scope may prove to be larger than initially anticipated. Subject to approval from the supervisors, topics may be deleted from the list above or reduced in extent.

In the master thesis report, the candidate shall present his personal contribution to the resolution of problems within the scope of the master thesis work

Theories and conclusions should be based on mathematical derivations and/or logic reasoning identifying the various steps in the deduction.



The candidate should utilise the existing possibilities for obtaining relevant literature.

### **Master thesis report format**

The master thesis report should be organised in a rational manner to give a clear exposition of results, assessments, and conclusions. The text should be brief and to the point, with a clear language. Telegraphic language should be avoided.

The report shall contain the following elements: A text defining the scope, preface, list of contents, summary, main body of thesis, conclusions with recommendations for further work, list of symbols and acronyms, references and (optional) appendices. All figures, tables and equations shall be numerated.

The supervisors may require that the candidate, in an early stage of the work, presents a written plan for the completion of the work.

The original contribution of the candidate and material taken from other sources shall be clearly defined. Work from other sources shall be properly referenced using an acknowledged referencing system.

The fact that parts of the report were written as part of the project period, shall be clearly stated in the introduction.

The report shall be submitted in electronic format (.pdf):

- Signed by the candidate
- The text defining the scope shall be included (this document)
- Drawings and/or computer models that are not suited to be part of the report in terms of appendices shall be provided on separate (.zip) files.

### **Ownership**

NTNU has according to the present rules the ownership of the master thesis reports. Any use of the report has to be approved by NTNU (or external partner when this applies). The department has the right to use the report as if the work was carried out by a NTNU employee, if nothing else has been agreed in advance.

### **Thesis supervisors:**


Svein Sævik, NTNU, [svein.savik@ntnu.no](mailto:svein.savik@ntnu.no)

Prof. Erin Bachynski-Polić, NTNU, [erin.bachynski@ntnu.no](mailto:erin.bachynski@ntnu.no)

**Deadline: June 19th, 2022**

Trondheim, January, 2022

  
Svein Sævik

  
Erin Bachynski-Polić



Candidate – date and signature:

*Adam Eide* 16.06.2022



# Preface

This master thesis summarizes the work conducted for a master's degree in marine technology. The work was done from January 2022 to June 2022 at the Department of Marine Technology at the Norwegian University of Science and Technology(NTNU). The thesis is a continuation of the project work conducted in Fall 2021.

The motivation behind the topic was to learn more about structural damping in marine structures as this is an important but not well-explored area. The work has resulted in well appreciated experience in project work, problem solving, laboratory testing and finite element modelling.

I would like to thank Erin Bachynski-Polić for all the help she has offered as one of my supervisor. I would also like to thank my other supervisor, Svein Sævik for very useful guidance during the whole project. In addition, I would like to express my gratitude to Emil Bratlie and all the technicians at the marine structures lab for the help with building and mending the laboratory setup. All the tips I received while running the experiments are also appreciated.

*Aadne Eide 16.06.2022*

---

Aadne Eide, 16.06.2022



# Abstract

In the design of large floating welded structures, the damping level is significant in deciding the response at frequencies of interest. The current engineering practice is based on rules of thumb, meaning the need for accurate representation of the damping levels might not always be achieved. In addition to hydrodynamic damping, aerodynamic damping, and soil damping, contributions from structural damping may also play a significant role in the behaviour of the structure. Structural damping can be divided into internal material damping and frictional damping in connections.

This thesis presents a report of analytical, experimental, and numerical work done in order to increase the understanding of the structural damping in welded steel structures. The main approach of the work was to conduct laboratory tests on a cantilever steel beam. Experiments were conducted on the beam with different support conditions in the form of a partly welded clamped end and a fully welded clamped end. In addition, a finite element (FE) model was created using Abaqus CAE with the purpose of replicating the beam in the experiments. In this numerical model, the steel-on-steel contact between the beam and plate was modelled using the augmented Lagrange contact formulation.

To assess the accuracy of the different methods, a static deflection test was conducted. The analytical results, experimental results, and numerical results were used in the assessment of assumed material properties in the experimental setup, and the mesh and contact formulation in the numerical. Furthermore, free vibration tests and forced vibration tests were conducted to establish the damping ratios of the beam with different support conditions. Damping ratios were measured using the logarithmic decrement and half-power point method.

The experimental results indicated that the damping increased as the clamped end went from partly welded to fully welded. However, the repeatably was seen as not satisfactory. For the forced vibration tests, there was a clear change in the behaviour of the beam during testing, these were observed as a reduction in the resonant frequency. The most consistent results came from the free vibration tests. Given that these seemed to coincide with the forced vibration, a rough estimate of the damping level of the physical was decided. The numerical model showed similar behaviour to the free vibration tests with the partially welded clamped end. However, there was not enough evidence to make a conclusion on the separation of material damping and frictional damping.





# Sammendrag

Dempingsnivået er viktig for å bestemme responsen ved nyttige frekvenser i design av store flytende sveiste stålstrukturer. Nåværende praksis er basert på *tommelfingerregler*, noe som betyr at nøyaktige estimeringer ikke alltid er tilfellet. I tillegg til hydrodynamisk demping, aerodynamisk demping og fundamentdemping kan bidragene fra strukturdemping også være sentrale i oppførselen til strukturen. Strukturdemping kan bli delt inn i den interne materialdempingen og friksjonsdempingen mellom sammenføyninger.

Denne oppgaven er en rapport på analytisk arbeid, eksperimentelt arbeid og numerisk arbeid som ble gjort for å øke forståelsen om strukturedemping i sveiste stålstrukturer. Det ble gjennomført eksperimenter på en bjelke med forskjellige innfestninger. Innfestningene bestod av en delvis sveist fast innspent ende og en helt sveist fast innspent ende. I tillegg ble en endelig element modell laget ved hjelp av Abaqus CAE. Denne var tiltenkt å gjenskape oppførselen til bjelken i eksperimentet. I den numeriske modellen ble *augmented Lagrange* kontaktformulering benyttet på stål mot stål kontaktflaten mellom bjelken og platen.

For å kunne bedømme nøyaktigheten til de forskjellige metodene ble det utført en statistisk nedbøyingstest. De analytiske resultatene, eksperimentelle resultatene og numeriske resultatene ble brukt under vurdering av de antatte materialgenskapene i det eksperimentelle oppsette. I tillegg ble det gjort vurderinger av *mesh* og kontaktformuleringen i den numeriske modellen. Videre ble fri vibrasjonstester og tvungen vibrasjonstester gjennomført for å etablere dempingsratioer. Dempingsratioene ble estimert ved bruk av logaritmisk dekkrement og *Half-power point* metoden.

De eksperimentelle resultatene indikerer at dempingen øker når den fast innspente enden går fra delvis sveis til helt sveist. Repeterbarheten var derimot ikke bra nok for disse testene. For forsøkene med tvungen vibrasjon var det en klar endring i oppførselen til bjelken under testing, hvor det var observert en reduksjon av resonansfrekvensen underveis. De mest konsekvente resultatene kom fra testene med fri vibrasjon. Siden disse tilsynelatende stemte med tvungen vibrasjon ble et grovt anslag på dempingen funnet. Den numeriske modellen viste lignende oppførsel som under frivibrasjonstestene for delvis sveiset fast innspent ende. Det var derimot ikke nok grunnlag til å trekke en konklusjon om fordelingen av materialdemping og friksjonsdemping.



# Table of Contents

<b>List of Figures</b>	<b>xv</b>
<b>List of Tables</b>	<b>xviii</b>
<b>Nomenclature</b>	<b>xx</b>
<b>1 Introduction</b>	<b>1</b>
<b>2 Theory and literature review</b>	<b>3</b>
2.1 Static deflection of cantilever beam . . . . .	3
2.2 Natural frequency of 2-DOF system . . . . .	4
2.2.1 Energy methods . . . . .	5
2.2.2 Eigenvalue problem . . . . .	8
2.3 Material damping . . . . .	9
2.3.1 Fundamentals of material damping . . . . .	9
2.3.2 Approaches to understanding material damping . . . . .	11
2.3.3 Linear micromechanisms causing damping in structural materials . . . . .	11
2.3.4 Nonlinear micromechanisms . . . . .	13
2.3.5 Damping of members . . . . .	14
2.4 Mathematical models of structural damping . . . . .	15
2.4.1 Linear viscous damping . . . . .	16
2.4.2 Coulomb damping . . . . .	17
2.4.3 Nonlinear viscous damping . . . . .	18
2.4.4 Equivalent viscous damping . . . . .	18

---

2.5	Forced vibration . . . . .	19
2.6	Dynamic amplification factor . . . . .	20
2.7	Multi-degree-of-freedom system . . . . .	20
2.8	Methods for establishing the damping matrix . . . . .	22
2.8.1	Rayleigh damping matrix . . . . .	22
2.8.2	Caughey series . . . . .	24
2.8.3	Direct evaluation of damping matrix . . . . .	25
2.9	Measurement of structural damping . . . . .	25
2.9.1	Logarithmic decrement . . . . .	25
2.9.2	Half-power point method . . . . .	26
2.10	Structural damping in welded marine structured . . . . .	28
2.10.1	Commonly used damping levels . . . . .	28
2.10.2	Previously conducted experiments . . . . .	29
<b>3</b>	<b>Experiment</b>	<b>31</b>
3.1	Context and hypothesis . . . . .	31
3.2	Experimental setup . . . . .	31
3.3	Welding . . . . .	32
3.4	Hardware . . . . .	34
3.5	Experimental methods . . . . .	36
3.5.1	Static deflection . . . . .	36
3.5.2	Free vibration . . . . .	37
3.5.3	Forced vibration . . . . .	37
3.6	Post processing . . . . .	37
3.6.1	Static deflection . . . . .	37
3.6.2	Natural frequency . . . . .	38
3.6.3	Logarithmic decrement . . . . .	38
3.6.4	Half-power point . . . . .	38
3.7	Sources of error . . . . .	38
3.7.1	Material and geometry . . . . .	38

---

---

3.7.2	Welds . . . . .	39
3.7.3	Measurements . . . . .	39
<b>4</b>	<b>Finite element analysis</b>	<b>41</b>
4.1	Model description . . . . .	41
4.2	Elements . . . . .	42
4.3	Mesh . . . . .	42
4.4	Dynamic analysis . . . . .	43
4.5	Constraints . . . . .	44
4.6	Damping in Abaqus . . . . .	44
4.7	Contact formulation . . . . .	44
4.8	Analysis procedures . . . . .	45
4.8.1	Static deflection . . . . .	45
4.8.2	Numerical eigenfrequency . . . . .	46
4.8.3	Numerical free vibration . . . . .	46
4.9	Methodology . . . . .	47
<b>5</b>	<b>Results and discussion</b>	<b>48</b>
5.1	Static deflection . . . . .	48
5.1.1	Analytical results . . . . .	48
5.1.2	Experimental results . . . . .	49
5.1.3	Numerical results . . . . .	50
5.2	Damping during free vibration . . . . .	53
5.2.1	Analytical natural frequency . . . . .	53
5.2.2	Experimental natural frequency and damping . . . . .	54
5.3	Damping during forced vibration . . . . .	59
5.3.1	Experimental results . . . . .	59
5.4	Assessment of repeatability . . . . .	67
5.5	Numerical damping results . . . . .	67
5.5.1	Numerical eigenfrequency . . . . .	67

---

5.5.2	Numerical free vibration for weld configuration 1 . . . . .	68
5.5.3	Accuracy of FE analyses . . . . .	70
<b>6</b>	<b>Conclusion and further work</b>	<b>72</b>
6.1	Conclusion . . . . .	72
6.2	Recommendations for further work . . . . .	73
	<b>Bibliography</b>	<b>74</b>
	Appendix . . . . .	i
A	Theory . . . . .	i
B	Python code . . . . .	iv
C	Experimental results . . . . .	xvi

# List of Figures

2.1	Beam model and 2DOF cantilever system . . . . .	4
2.2	2 DOF system . . . . .	5
2.3	Hysteresis loops (Lazan, 1968) . . . . .	10
2.4	Rate dependence of damping due to micromechanisms (Lazan, 1968)	12
2.5	Grain structure in carbon steel (Cuevas-Arteaga et al., 2012) . . . . .	12
2.6	Model and hysteresis loop for Coulomb damping (Langen and Sigbjörns- son, 1979) . . . . .	18
2.7	Rayleigh damping from (Hall, 2006). . . . .	24
2.8	Response-frequency curve in half-power bandwidth method (Olmos and Roesset, 2010) . . . . .	27
3.1	Cantilever beam with exciter . . . . .	32
3.2	Weld configuration 1 . . . . .	33
3.3	Sketch with numbering of welds as seen from tip towards clamped end.	33
3.4	Welds along all of beam . . . . .	34
3.5	Acceleration sensors . . . . .	35
3.6	Sketch of beam with hardware . . . . .	35
3.7	Measurement of tip deflection . . . . .	36
4.1	Profile of welds . . . . .	41
4.2	FE model . . . . .	42
4.3	Mesh near clamped end . . . . .	43
4.4	Beam with static pressure load . . . . .	46
5.1	Displacement along beam with all weights . . . . .	50

---

5.2	Stress in weld during static loading, weld configuration 1 . . . . .	51
5.3	Weld at top flange . . . . .	51
5.4	Static deflection, 5.5 cm from tip . . . . .	52
5.5	Time series of vertical acceleration . . . . .	54
5.6	Frequency domain plot of acceleration . . . . .	55
5.7	Identified peaks, test 1 . . . . .	56
5.8	Convergence, weld configuration 1 . . . . .	56
5.9	Convergence, weld configuration 2 . . . . .	58
5.10	Vertical acceleration, max strain at 31.9 $Hz$ . . . . .	59
5.11	vertical -and horizontal acceleration, max strain at 31.9 Hz . . . . .	60
5.12	Maximum strain at 30.2 Hz . . . . .	61
5.13	Maximum strain at 31.9 Hz . . . . .	62
5.14	Damping ratios for weld configuration 1 . . . . .	62
5.15	Time-series during forced vibration . . . . .	63
5.16	Horizontal and vertical acceleration . . . . .	64
5.17	Strain at top flange . . . . .	64
5.18	Frequency vs. damping . . . . .	66
5.19	Natural frequency in bending mode . . . . .	67
5.20	Transition between static and implicit dynamic analysis . . . . .	68
5.21	Transition between static and implicit dynamic analysis . . . . .	68
5.22	Opening and contact area . . . . .	69
5.23	Vertical motion of top and bottom . . . . .	69
5.24	Vertical motion of bottom flange and web at bottom weld . . . . .	70
5.25	Measured peaks for different time steps . . . . .	71
C.1	Weld configuration 1, test 1 . . . . .	xvi
C.2	Weld configuration 1, test 2 . . . . .	xvii
C.3	Weld configuration 1, test 3 . . . . .	xvii
C.4	Weld configuration 1, test 4 . . . . .	xvii
C.5	Weld configuration 1, test 5 . . . . .	xviii

---



---

C.6 Weld configuration 1, test 6 . . . . .	xviii
C.7 Weld configuration 2, test 1 . . . . .	xviii
C.8 Weld configuration 2, test 2 . . . . .	xix
C.9 Weld configuration 2, test 3 . . . . .	xix
C.10 Weld configuration 2, test 4 . . . . .	xix
C.11 Weld configuration 2, test 5 . . . . .	xx
C.12 Weld configuration 2, test 6 . . . . .	xx
C.13 Weld configuration 2, test 7 . . . . .	xx
C.14 Weld configuration 1, test 2 . . . . .	xxi
C.15 Weld configuration 1, test 3 . . . . .	xxi
C.16 Weld configuration 1, test 4 . . . . .	xxi
C.17 Weld configuration 1, test 5 . . . . .	xxii
C.18 Weld configuration 1, test 6 . . . . .	xxii
C.19 Weld configuration 1, test 7 . . . . .	xxii
C.20 Weld configuration 1, test 8 . . . . .	xxiii
C.21 Weld configuration 2, test 1 . . . . .	xxiii
C.22 Weld configuration 2, test 2 . . . . .	xxiii
C.23 Weld configuration 2, test 3 . . . . .	xxiv
C.24 Weld configuration 2, test 4 . . . . .	xxiv
C.25 Weld configuration 2, test 5 . . . . .	xxiv
C.26 Weld configuration 2, test 6 . . . . .	xxv
C.27 Weld configuration 2, test 7 . . . . .	xxv
C.28 Weld configuration 2, test 8 . . . . .	xxv

# List of Tables

2.1	Equivalent viscous damping ratios . . . . .	19
2.2	DAF for different damping ratios at resonance . . . . .	20
3.1	Beam dimensions . . . . .	32
3.2	Weld measurements, weld configuration 1 . . . . .	33
3.3	Weights . . . . .	36
5.1	Dimensions . . . . .	48
5.2	Analytical results for static loading. $\delta$ is the analytical deflection at the tip. $\varepsilon$ is the analytical strain 0.4m from the clamped end. . . . .	49
5.3	Deflection 5.5 cm from tip. $\delta_1$ is the deflection for weld configuration 1. $\delta_2$ is the deflection for weld configuration 2. $\Delta\delta_1$ and $\Delta\delta_2$ are the changes in deflection. . . . .	49
5.4	Strain in top flange 0.4 m from clamped end. $\varepsilon_1$ is the strain for weld configuration 1. $\varepsilon_2$ is the strain for weld configuration 2. $\Delta\varepsilon_1$ and $\Delta\varepsilon_2$ are the changes in strain. . . . .	49
5.5	Results, numerical static deflection for weld configuration 1 . . . . .	50
5.6	Horizontal displacement at weld . . . . .	52
5.7	Contact opening at top flange and bottom flange . . . . .	52
5.8	Measured natural frequency, weld configuration 1 . . . . .	55
5.9	Measured natural frequency and damping, weld configuration 1 . . . . .	57
5.10	Measured natural frequency and damping, weld configuration 2. $f_n$ is the natural frequency. $n$ is the number of peaks counted. $\zeta$ is the damping ratio. $\varepsilon_m$ is the maximum measured strain. . . . .	58
5.11	Results: Weld configuration 1 . . . . .	61
5.12	Results weld configuration 2 . . . . .	65

---

C.1 Convergence, weld configuration 1 . . . . .	xvi
---	-----

# Nomenclature

$\alpha_1, \alpha_2$  mass -and stiffness proportionality coefficients

$\beta$  Frequency ratio

$\ddot{\mathbf{r}}$  Acceleration vector

$\dot{\mathbf{r}}$  Velocity vector

$\mathbf{C}, \overline{\mathbf{C}}, \overline{\overline{\mathbf{C}}}$  Damping matrix

$\mathbf{K}, \overline{\mathbf{K}}$  Stiffness matrix

$\mathbf{M}, \overline{\mathbf{M}}$  Mass matrix

$\mathbf{Q}$  Load vector

$\mathbf{r}$  Displacement vector

$\mathbf{y}$  Amplitude vector

$\delta$  Deflection

$\Delta\delta$  Change in deflection

$\Delta\varepsilon$  Change in strain

$\delta$  Logarithmic decrement

$\delta_1$  Deflection, weld configuration 1

$\delta_2$  Deflection, weld configuration 2

$\eta$  Loss coefficient

$\kappa$  Curvature

$\mu$  Coefficient of friction

$\nu$  Poisson ratio

$\omega, \hat{\omega}$  Angular frequency

$\omega_d$  Damped natural angular frequency

$\omega_n$  Natural angular frequency

---

$\phi$	Shape function
$\psi$	Specific damping coefficient
$\rho$	Density
$\sigma$	Stress
$\sigma_a$	Stress amplitude
$\sigma_m$	Maximum stress at any point in specimen
$\theta$	Angle
$\varepsilon$	Strain
$\varepsilon_m$	Maximum observed strain
$\zeta$	Damping ratio
$A, B$	Constants
$a$	Damping coefficient
$c, a, q$	Damping coefficients
$C_D$	Drag coefficient
$c_{cr}$	Critical damping coefficient
$D$	Unit damping energy
$D_s$	Total damping energy
$D_{av}$	Average damping energy
$E$	Young's modulus
$E$	Young's modulus
$F$	Applied load
$f$	Frequency
$F^D$	Damping force
$g$	Gravitational acceleration
$H$	Magnitude of frequency response function
$I$	Moment of inertia
$i, j$	Indices
$J$	Damping constant
$k$	Stiffness coefficient

---

---

$k_\theta$	Rotational stiffness
$L$	Length
$l$	Number of degrees of freedom
$M$	Moment
$m$	Mass coefficient
$N$	Normal force
$n$	Damping exponent
$P$	Point load
$q, Q$	Load
$R$	Frequency range
$s_{1,2}$	Roots of homogeneous solution of equation of motion
$t$	Time
$T_d$	Damped natural period
$U$	Maximum potential energy
$u$	Displacement
$V_s$	Volume
$X$	Displacement

## Acronyms

<b>DAF</b>	Dynamic amplification factor
<b>DOF</b>	Degree of freedom
<b>FE</b>	Finite element
<b>MDOF</b>	Multi-degree-of-freedom
<b>SDOF</b>	Single-degree-of-freedom
<b>VLFS</b>	Very Large Floating Structure

# Chapter 1

## Introduction

In the maritime industry, steel structures are a crucial part of the infrastructure. For some purposes it is more cost-effective and safe to build large structures. Some of these are classified as very large floating structures (VLFS). Compared to traditional ships and offshore rigs, the flexible modes of larger structures may lead to lower stiffness and consequently longer natural periods (Mobron et al., 2021). Accurate estimation of the dynamic response is desired as an overestimation will lead to very large plate thicknesses, again leading to increased steel weight and manufacturing costs. The structural dynamics are also part of the global strength documentation, which are required to be approved by classification societies.

In the offshore industry methods using dynamic amplification factors (DAF) are well-known and proven (Horn et al., 2015). Here, the intention is to include inertia forces by relating the dynamic response to the static response. In order to utilize these methods in the design of large structures for aquaculture, transportation and energy harvesting at sea, accurate estimations are needed in order to predict the resonant response. The choice of structural damping ratio will effect the DAF, meaning a high accuracy of the damping ratio will give better and more accurate results. The current way of assigning damping ratios to marine structures is to use typical values. These come from measurements, meaning there is no known method of estimating the damping of a structure before it is built. In addition, it is difficult to distinguish structural damping from hydrodynamic damping, aerodynamic damping and other sources. The need to establish methods of predicting the structural damping of welded steel structures is therefore present in the maritime industry.

Currently, rules of thumb are often used when setting values for structural damping in dynamic analysis. These are often established without a strong basis in empirical results or material models, resulting in a knowledge gap in the determination of damping values in welded steel shell structures relevant for many marine applications. This master thesis work is intended to investigate this knowledge gap and to improve the understanding of structural damping in such structures.

The scope of the work goes as follows. Literature review of the present empirical and numerical approaches of estimating both material and structural damping. In addition, full scale data and numerical models are to be familiarized with. Given

---

that the knowledge on structural damping in marine structures is rather limited, literature from civil engineering is also reviewed. In addition laboratory test are conducted in order to improve the understanding of material damping and the effects of welds in relevant scale structures. Experiments will be conducted on a welded cantilever I-beam where in addition the determination of the damping, the effect of different support conditions in the form of weld geometries is investigated. Lastly, the development of an FE model in order to perform simulations of the experimental setup and explain the observed damping performance.

The report is divided into the following section. First, relevant theory and a review of the current literature is presented. Parts of this review was done during the project work in Fall 2021. Furthermore, the experimental setup and experimental procedures are presented. Next, the Abaqus CAE model and procedures are presented. Afterwards, the results are presented and discussed. Lastly, a conclusion and recommendation for further work given.



# Chapter 2

## Theory and literature review

In order to obtain a greater understanding of the importance of damping in steel structures one can look at the known theory. The following section presents relevant theory for analytical calculations and post-processing of experimental results. As the experimental setup is a cantilever beam, the analytical static deflection and natural frequency of beams are presented first. Furthermore, a presentation of structural damping phenomena and the mathematical models are presented. In addition, the results from a literature review of commonly used damping ratios and previously conducted experiments are presented. Since damping can be regarded as a niche area, this section is quite comprehensive as the reader might not be familiar with all the theory.

### 2.1 Static deflection of cantilever beam

When considering a cantilever beam, the static deflection of the tip due to a point load is written as:

$$\delta = \frac{P}{K} \quad (2.1)$$

In Equation 2.1,  $\delta$  is the tip deflection,  $P$  is the point load and  $K$  is the beam stiffness. The tip deflection for a cantilever is known to be:

$$\delta = \frac{Pl^3}{3EI} \quad (2.2)$$

In Equation 2.2,  $EI$  is the beam bending stiffness and  $l$  is the length of the beam. Note that the clamped end is assumed to be completely rigid in Equation 2.2. If this is not the case, a rotational spring with stiffness  $K_\theta$  is introduced. Considering the moment around the clamped end, one can account for the rotational spring stiffness in the expression for tip deflection:

$$\delta = \frac{PL^3}{3EI} + \frac{PL^2}{K_\theta} \quad (2.3)$$

Solving for the spring stiffness leads to the following expression:

$$K_\theta = \frac{PL^2}{\delta} - \frac{3EI}{L} \quad (2.4)$$

A practical way of measuring the behaviour along the beam is the strain during deflection. The following expression can be used to calculate the strain at a given point along the beam:

$$\varepsilon(x, z) = \frac{M(x) \cdot z}{EI} = \frac{P \cdot (L - x) \cdot z}{EI} \quad (2.5)$$

## 2.2 Natural frequency of 2-DOF system

Another topic for interest is the analytical natural frequency. In order to obtain the natural frequency, the mass and stiffness matrices of the system have to be determined. Two possible methods for obtaining the natural frequency are presented below.

### Euler Bernoulli beam theory with consistent mass matrix

A way to find an estimate of the natural frequency of a cantilever beam is to consider the elastic 2D Euler beam in matrix form.

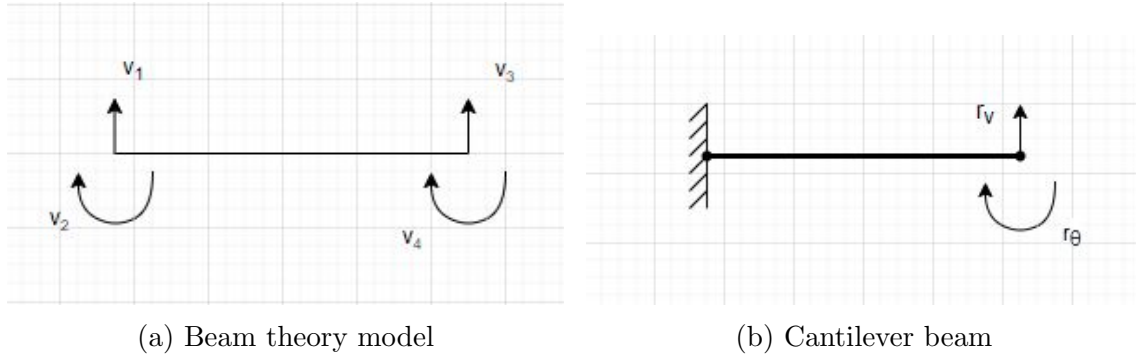


Figure 2.1: Beam model and 2DOF cantilever system

The full mass matrix and stiffness matrix for the beam element shown in Figure 2.1a are given in Section A.

Considering the boundary conditions results in the following  $2 \times 2$  matrices system.

$$\mathbf{M} = \frac{ml}{420} \begin{bmatrix} 156 & 22l \\ 22l & 4l^2 \end{bmatrix} \quad (2.6)$$

---


$$\mathbf{K} = \frac{2EI}{l^3} \begin{bmatrix} 6 & 3l \\ 3l & 2l^2 \end{bmatrix} \quad (2.7)$$

If a point mass  $m$  is to introduced to the system at a given DOF this is done by adding it to the respective placement in the mass matrix. The mass matrix for the system in Figure 2.1 with a point mass on the tip becomes:

$$\mathbf{M} = \frac{ml}{420} \begin{bmatrix} 156 & 22l \\ 22l & 4l^2 + m \end{bmatrix} \quad (2.8)$$

### 2.2.1 Energy methods

If the system has some rotation at the clamped end, another possible way to establish the mass matrix and stiffness matrix is to use energy methods. A system with rotation is shown in Figure 2.2.

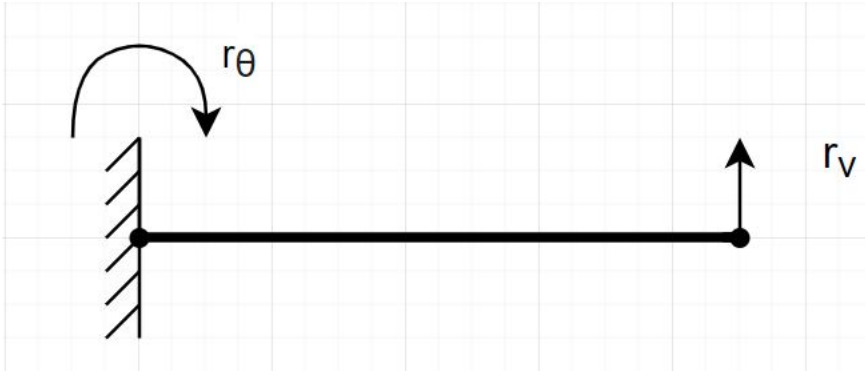


Figure 2.2: 2 DOF system

In general, one can use the following equation to express the displacement of a beam:

$$\mathbf{r}(\mathbf{x}) = C_0 + C_1 \cdot x + C_2 \cdot x^2 + C_3 x^3 \quad (2.9)$$

In Equation 2.9  $\mathbf{r}(\mathbf{x})$  is the displacement along the beam.  $C_0, C_1, C_2$  and  $C_3$  are constants.  $x$  is the horizontal position of along the beam.

For the system in Figure 2.2, the following equation is also valid.

$$\mathbf{r} = r^1 + r^2 = \mathbf{N}^T \mathbf{r} = \begin{bmatrix} \phi_v & \phi_\theta \end{bmatrix} \begin{bmatrix} r_v \\ r_\theta \end{bmatrix} \quad (2.10)$$

---

In Equation 2.10  $r_v$  and  $r_\theta$  are the displacement in the respective degrees of freedom whereas  $\phi_v$  and  $\phi_\theta$  are the shape functions. The shape functions are found by applying a unit load to on degree of freedom while assuming the other to be stationary. Firstly, one can find  $\phi_v$  by considering the bending moment along the beam.

$$M = P(L - x) \quad (2.11)$$

The relation between moment and curvature is given by:

$$M = EI\kappa \quad (2.12)$$

By considering a unit load, the curvature is given by:

$$\kappa = r_{v,xx} = \frac{1(L - x)}{EI} \quad (2.13)$$

The displacement function is thereby found from double integration, with constants found from the following boundary conditions.

- $r_v(0) = 0$
- $r_{v,x}(0) = 0$
- $r_v(L) = 1$
- $r_{v,xx}(L) = 0$

The double integration goes as follows.

$$r_{v,x} = \frac{1}{EI} \int (L - x) dx = \frac{1}{EI} \left( Lx - \frac{1}{2}x^2 \right) + C_1 \quad (2.14)$$

$C_1 = 0$  since the angle  $r_{v,x} = 0$  at  $x = 0$ . The deformation can be found by another integration.

$$r_v = \frac{1}{EI} \int \left( Lx - \frac{1}{2}x^2 \right) dx = \frac{1}{EI} \left( \frac{1}{2}Lx^2 - \frac{1}{6}x^3 \right) + C_2 \quad (2.15)$$

$C_2 = 0$  since  $r_v(0) = 0$ . The shape function is then given by:

$$\phi_v = \left( \frac{1}{2}Lx^2 - \frac{1}{6}x^3 \right) \quad (2.16)$$

It is noted that in order to obtain the unit deflection, one need to scale the shape function by  $\frac{3}{L^3}$ , resulting in the following.

$$\phi_v = \frac{3}{L^3} \left( \frac{1}{2}Lx^2 - \frac{1}{6}x^3 \right) \quad (2.17)$$

A similar procedure is performed in order to find the shape function for  $\phi_\theta$ . Initially, it is known that a moment,  $M_0$ , applied in  $r_\theta$  must satisfy the following conditions.

- 
- $M(0) = M$
  - $M(L) = 0$

The resulting function for the moment then become:

$$M(x) = M_0 \left(1 - \frac{x}{L}\right)$$

The following boundary conditions are applied in the calculation.

- $r_\theta(0) = 0$
- $r_\theta(L) = 0$
- $r_{\theta,x}(0) = 1$
- $r_{\theta,xx}(L) = 0$

The resulting shape function is given as:

$$\phi_\theta = \left(\frac{-3}{L}\right) \cdot \left(\frac{x^2}{2} - \frac{x^3}{6L} - \frac{L}{3}x\right) \quad (2.18)$$

When the shape functions are know one can establish the consistent mass matrix and stiffness matrix. They are given as the following.

$$\mathbf{M} = \begin{bmatrix} m_v & m_{v\theta} \\ m_{v\theta} & m_\theta \end{bmatrix} = \rho A \int_0^L \begin{bmatrix} \phi_v \phi_v & \phi_v \phi_\theta \\ \phi_\theta \phi_v & \phi_\theta \phi_\theta \end{bmatrix} dx \quad (2.19)$$

$$\mathbf{K} = \begin{bmatrix} k_v & k_{v\theta} \\ k_{v\theta} & k_\theta \end{bmatrix} = EI \int_0^L \begin{bmatrix} \phi_{v,xx} \phi_{v,xx} & \phi_{v,xx} \phi_{\theta,xx} \\ \phi_{\theta,xx} \phi_{v,xx} & \phi_{\theta,xx} \phi_{\theta,xx} \end{bmatrix} dx \quad (2.20)$$

The integration of the elements in Equation 2.19 is given in Section A.

The resulting consistent mass matrix is presented in the following.

$$\mathbf{M} = \begin{bmatrix} \frac{99}{420}mL & \frac{67}{280}mL^2 \\ \frac{67}{280}mL^2 & \frac{2}{105}mL^3 \end{bmatrix} \quad (2.21)$$

The stiffness matrix is found in the following manner. First, the elements in the matrix in Equation 2.20 are found.

---


$$\phi_{v,xx} = x \quad (2.22a)$$

$$\phi_{\theta,xx} = 1 - \frac{1}{x} \quad (2.22b)$$

By inserting the relations in Equation 2.22 into Equation 2.20 the following results are obtained.

$$\mathbf{K} = EI \int_0^L \begin{bmatrix} x^2 & x - \frac{x^2}{L} \\ \frac{x^2}{L} & 1 - \frac{2x}{L} + \frac{x^2}{L^2} \end{bmatrix} dx = EI \begin{bmatrix} \frac{L^3}{3} & \frac{L^2}{6} \\ \frac{L^2}{6} & \frac{L}{3} \end{bmatrix} \quad (2.23)$$

By including a lumped mass  $m_e$  in the vertical DOF and a spring stiffness  $k_\theta$  in the rotational DOF the final matrices for the 2 DOF system in Figure 2.2 becomes:

$$\mathbf{M} = \begin{bmatrix} \frac{99}{420}mL + m_e & \frac{67}{280}mL^2 \\ \frac{67}{280}mL^2 & \frac{2}{105}mL^3 \end{bmatrix} \quad (2.24)$$

$$\mathbf{K} = EI \begin{bmatrix} \frac{L^3}{3} & \frac{L^2}{6} \\ \frac{L^2}{6} & \frac{L}{3} + k_\theta \end{bmatrix} \quad (2.25)$$

## 2.2.2 Eigenvalue problem

Considering free undamped vibration and assuming both degrees of freedom to have the same frequency and phase yields the following equation of motion:

$$\mathbf{M}\ddot{\mathbf{r}} + \mathbf{K}\mathbf{r} = 0 \quad (2.26)$$

Where  $\mathbf{M}$  is the mass matrix,  $\mathbf{K}$  is the stiffness matrix, and  $\mathbf{r}$  is the displacement vector. By setting  $\mathbf{r} = \boldsymbol{\phi} \sin(\omega t)$  the general eigenvalue problem can be obtained.

$$[\mathbf{K} - \omega^2 \mathbf{M}] \boldsymbol{\phi} = 0 \quad (2.27)$$

In order to not get a trivial solution when solving  $[\mathbf{K} - \omega^2 \mathbf{M}]$ , the matrix determinant is set to zero.

$$\text{Det}([\mathbf{K} - \omega^2 \mathbf{M}]) = 0 \quad (2.28)$$

This matrix will be singular and a non-trivial solution can be found. The square root of the eigenvalues are the eigenfrequencies of the system, and the eigenvectors are the mode shapes. The mode shape can be describe as the response to a corresponding eigenfrequency. For a 2-DOF system it is possible to find the analytical values of  $\omega_1$  and  $\omega_2$ . More on multi-degrees-of-freedom (MDOF) systems in Section 2.7.

---

---

## 2.3 Material damping

When a structure is subjected to oscillatory deformations, the potential and kinetic energy can describe the state of the structure. For a real structure some of the energy is lost during oscillation, and converted to thermal energy. This conversion is known as damping. Structural damping can be divided into two parts. Material damping and friction damping in connections. A possible way of obtaining a deeper understanding of the damping in large structures is to look at the underlying theory of the microscopical processes in the material itself. In this subsection, the concept of material damping will be presented by looking at mechanisms and mathematical models.

An in-depth study of damping in different structural materials was done by B.J. Lazan in the 1960's. These models are still regarded as valid today, as not much additional research has been done since. The work is presented in the book *Damping of materials and Members in Structural Mechanics*(Lazan, 1968). Section 2.3.1, Section 2.3.2, Section 2.3.3, Section 2.3.4 and Section 2.3.5 are based on the theory found in this book.

### 2.3.1 Fundamentals of material damping

In general, the material damping is described as dependent on many factors, where the main ones are type of material, stress amplitude, internal force, number of cycles, size of geometry and temperature. The quantification of the damping energy is done by assessing the hysteresis loops during cyclic loading. The following figure show examples of hysteresis loops are from Lazan's book.

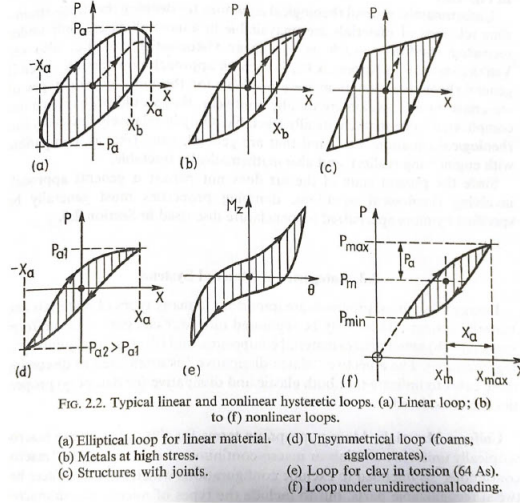


Figure 2.3: Hysteresis loops (Lazan, 1968)

The general equations for the damping of complete members and for materials are given as:

$$D_s = \oint P \cdot dX \quad (2.29)$$

$$D = \oint \sigma \cdot d\varepsilon \quad (2.30)$$

The integral given in Equation 2.29 represents the area within the hysteresis loop of the complete specimen/part.  $D_s$  is the absorbed energy per cycle of loading.  $P$  is the applied load and  $X$  is the displacement. Equation 2.30 describes the damping in the material.  $D$  is the unit energy absorbed by a macroscopically uniform material per unit volume during cyclic loading.  $\sigma$  is the unit stress and  $\varepsilon$  is the unit strain.

Lazan saw that the internal damping of structural materials can be described in the following way:

$$D = J \cdot \sigma_a^n \quad (2.31)$$

where  $J$  and  $n$  are constants and  $\sigma_a$  is the stress amplitude.  $n$  is normally between 2 and 4.  $n = 2.3$  is a typical value (Orban, 2011).



---

A quantification of the damping in a material is given by the specific damping capacity,  $\psi$ . This is the energy loss per cycle divided by the maximum potential (strain) energy during one cycle:

$$\psi = \frac{D}{U} \quad (2.32)$$

Another used measure of damping is the loss coefficient,  $\eta$ . This is defined as the specific damping capacity for each cycle.

$$\eta = \frac{\psi}{2\pi} \quad (2.33)$$

### 2.3.2 Approaches to understanding material damping

Lazan (1968) presented three different methods for understanding damping. First, the micromechanisms in the material from a research point of view give a greater understanding of why and how damping happens. However, this method has its problems of being utilized as an engineering tool as many variables in the given material and environment makes it hard to predict the behaviour of the micromechanisms. Nevertheless, it is mentioned that correlations can be useful. Secondly, ad hoc testing may provide data on a specific material under certain stress and environmental conditions. Again, for engineering purposes this will be hard to utilize as the conditions for the data obtained are very specific. The macroanalytical approach starts with determining the unit properties of the material. These can later be used to express the properties of the whole member and mathematical models can be developed.

Useful classifications of damping phenomena in materials are rate-dependency and rate-independency. "Perfectly elastic" is used for materials where the stress-strain curve is linear. Any deviation from this will be characterized as "inelasticity". This can be from rate-dependent behaviour, meaning the frequency of the loading is important. However, it can also be dependent on the recoverability, which means the materials ability to return to previous deformation, i.e no plastic deformation. For quantifying the damping, Equation 2.31 can be used with different values of  $n$ . An example here is  $n = 2$ , giving linear damping and an elliptical hysteresis loop.

### 2.3.3 Linear micromechanisms causing damping in structural materials

The observed damping behaviour is better understood by assessing the micromechanisms that are present in the material. For metals at low and intermediate applied stress, some of the material damping mechanisms show a linear behaviour with respect to the stress. This stress range is relevant when considering welded structures as stresses close to yield are not expected because of fatigue considerations. These physical mechanisms are generally frequency (or temperature) dependent,

with peaks in the internal damping at different frequencies. Some important mechanisms will be presented, and the rate-dependence of the loss coefficient is shown in Figure 2.4.

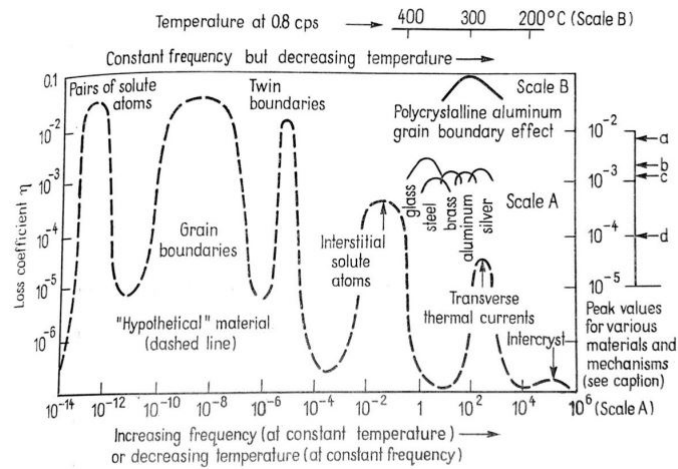


Figure 2.4: Rate dependence of damping due to micromechanisms (Lazan, 1968)

The grains of carbon steel are shown in Figure 2.5. It is clear that the size, shape and environment of the grains all vary from point to point. Macroscopic behaviour therefore depends on the distribution of these features. Grain boundary viscosity is a form of damping that comes from the disordered state of the grains. Under cyclic loading, the energy dissipation from internal friction between grains will be larger at the boundaries than within the grains. This type of internal friction is frequency and temperature dependent. For low temperature or high frequency, the energy dissipation will be low as a result of the shear strain along the boundary only relaxing slightly. This will lead to a narrow hysteresis loop. For high temperature or low frequency there will be full relaxation during the cycles, and the cyclic strain is also reduced giving a narrow loop. It is during an intermediate state that the largest area under the hysteresis loop is present, i.e maximum damping is produced.

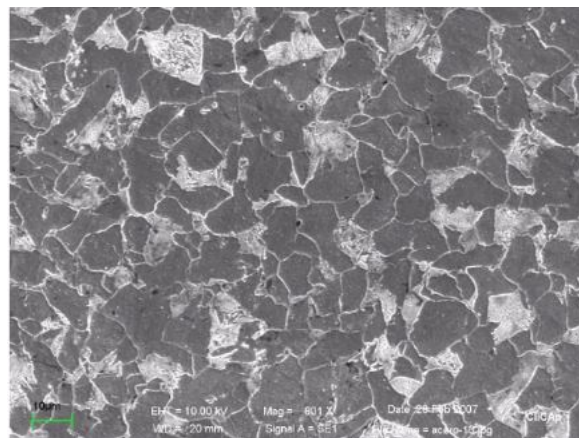


Figure 2.5: Grain structure in carbon steel (Cuevas-Arteaga et al., 2012)

---

Another damping mechanism is the heat transfer during loading. On a macroscopic level, if the specimen is loaded non-uniformly, a heat gradient will be produced between the local stresses. If the load frequency is higher or lower than the time of heat flow along temperature gradients, the process is reversible and there will be no damping. However, when the load frequency is close to the heat flow we have the transformation of mechanical energy to heat. i.e damping. This mechanism can also appear on a smaller scale between the grains. Since the grains are oriented in different directions, heat gradients can be formed even under uniform axial loading of the material.

Another microscopic damping phenomena is the dislocation motion between slip-planes. The dislocation components will under alternating stress lag behind the applied stress. This forms a hysteric loop, which again means dissipation of energy. This type of mechanism can happen with relatively low applied stress, as the local stresses can be large on a microscopic level.

### 2.3.4 Nonlinear micromechanisms

There are also nonlinear micromechanisms present in metals. One type of nonlinear and rate-independent damping is known as plastic slip. On a microscopic scale, inhomogeneity in the stress distribution will lead to high local stresses that may cause local plastic strain. This phenomena can happen even though the macroscopic stress is low, with increasing occurrence as the stress gets closer to yield. Since dislocations and their features(kind,role, number dispercion and lattice anchorage) are not well understood, they are lumped under the term *plastic strain damping*.

The most important damping mechanism in metals is pointed out to be the magnetoelastic mechanism in ferromagnetic materials e.g steel. The previously mentioned contributions from linear damping (anelastic and dislocation mechanisms) are generally small if the frequency does not coincide with the peaks in Figure 2.4. The plastic-strain mechanism can provide large damping, but this is at high stresses near the fatigue limit. However, magnetoelastic damping is shown to have large values at low and intermediate stress.

This mechanism can be explained in the following way. Firstly, ferromagnetic substances are composed of small domains that are individually magnetized to saturation. When the metal is demagnetized, the result is random directions of the magnetization vector for each domain. However, a magnetic field may affect the direction of the vector field. This change in magnification gives movement in the walls of the domain. A stress field (or strain) will also change the state of magnetization of the material. This leads to rotation of the domain vectors and wall movements similar to those from a magnetic field. If the material is under cyclic stress there will be a cyclic elastic strain, but also a cyclic magnetostrictive stress component. The latter is an irreversible process, leading to damping. At low and intermediate stress, exposing a ferromagnetic material to a magnetic field or magnetized it to saturation will lead to low measured damping. This indicates that the dominating mechanism is related to magnetorestriction.

---

Most materials also show a decrease in magnetoelastic damping with increasing temperature, however the decrease is small until the curie temperature is reached. This is the temperature where materials lose their magnetism. Given a static mean stress the damping can be reduced by suppressing the motion of the domain walls. In addition, the magnetoelastic damping is independent of frequency in the ranges present in structural mechanics.

### 2.3.5 Damping of members

The mechanisms described in Section 2.3.3 and Section 2.3.4 will often be "lumped" together in idealized models which can be applied for calculations. For members, three different damping units are usually used. The total damping energy  $D_s$  [Nm/cycle], the average damping energy  $D_{av} = D_s/V_s$  [N/m<sup>2</sup>cycle] and the unit damping energy  $D$  [N/m<sup>2</sup>cycle]. The unit damping  $D$  is a true material property that is not dependent on shape, stress or volume of part. The average damping energy unit  $D_{av}$  is defined by total damping energy  $D_s$  divided by the volume  $V_s$ . It is shown to be dependent on both the stress and and shape, meaning it will not be a good material property to base further calculations on. However, this is a common way to present damping data.  $D_s$  is the total damping of a whole member, and is usually of interest in structural analysis. The main goal is therefore to express this total damping as a function of the general material property  $D$ . Lazan (1968) presented the following equations:

$$\begin{aligned}
 D_s &= \int_{V=0}^{V_s} D dV = \frac{V_s}{\sigma_{am}} \int_{\sigma=0}^{\sigma_{am}} D \frac{d(V/V_s)}{d(\sigma_a/\sigma_{am})} d\sigma_a \\
 &= D_{am} V_s \int_{\sigma_a/\sigma_{am}=0}^1 \left( \frac{D}{D_{am}} \right) \frac{d(V/V_s)}{d(\sigma_a/\sigma_{am})} d(\sigma_a/\sigma_{am}) \\
 &= D_{am} V_s \alpha
 \end{aligned} \tag{2.34}$$

$$D_{av} = \frac{D_s}{V_s} = \alpha D_{am} \tag{2.35}$$

Above, the following is used:

- The normalized damping integral:  $\alpha = \int_{\sigma_a/\sigma_{am}=0}^1 \left( \frac{D}{D_{am}} \right) \frac{d(V/V_s)}{d(\sigma_a/\sigma_{am})} d(\sigma_a/\sigma_{am})$
- $D_{am}$ =unit damping energy at  $\sigma_a = \sigma_{am}$
- $V_s$ =total effective volume of specimen or part contributing to dissipation.
- $V$ =volume of specimen or part subjected to stress less than  $\sigma_a$
- $\sigma_a$ =amplitude of stress at any point in specimen, where  $0 < \sigma_a < \sigma_{am}$
- $\sigma_{am}$ =maximum stress at any point in specimen.
- $D_{av}$ =average damping energy.

---

In order to calculate the material damping of a member,  $\alpha$  and  $D_{am}$  need to be found.  $\alpha$  is found by Equation 2.34. This is dependent on two functions. The volume-stress function:

$$\frac{V}{(V_s)} \quad (2.36)$$

and the damping function:

$$D/D_{am} \quad (2.37)$$

The volume-stress function for a cantilever beam with bending moment  $M_x = \frac{x}{L}M_0$ , is given by:

$$\frac{V}{V_s} = \frac{\sigma_a}{\sigma_{am}} \left[ 1 - \ln \frac{\sigma_a}{\sigma_{am}} \right] \quad (2.38)$$

The stress distribution function to be used in Equation 2.34 is then defined:

$$\frac{d(V/V_s)}{d(\sigma_a/\sigma_{am})} = -\ln \frac{\sigma_a}{\sigma_{am}} \quad (2.39)$$

Assuming the general case of  $D = J\sigma_a^n$ , gives the function  $\alpha$  the following definition for a cantilever beam:

$$\alpha = \frac{1}{(n+1)^2} \quad (2.40)$$

Considering the theory and mathematical models presented in this section it is clear that the damping for a given structural material is possible to obtain. In *Damping of materials and Members in Structural Mechanics* the damping properties of steel in bending is given by the loss coefficient under certain loading. During cyclic loading with a frequency of  $f = 2$  Hz and a mean longitudinal stress of  $\sigma_m = 20.68$  MPa, the loss coefficient is given as  $\eta_s = 4.8 \cdot 10^{-4}$ .

## 2.4 Mathematical models of structural damping

The damping mechanisms described in Section 2.3 are microscopic phenomena. However, the equation of motion used in structural analysis describes macroscopic behaviour creating a conflict of scale (Kareem and Gurley, 1996). The term structural damping is used to describe the energy dissipation of the whole structure. In the following subsection, some important mathematical models for structural damping is presented.

The real damping of a system may be difficult to model correctly as different types of damping may be present. It is therefore convenient to introduce simplified models. Some common damping models can be described by the following:

$$F^D(\dot{u}) = a\dot{u}|\dot{u}|^{\theta-1} \quad (2.41)$$

Above,  $F^D(\dot{u})$  is the damping force,  $\dot{u}$  is the velocity and  $a$  is a damping coefficient (Kareem and Gurley, 1996).

---

### 2.4.1 Linear viscous damping

Linear viscous damping is commonly used in the dynamic equilibrium equation and has proven sufficient accuracy (Langen and Sigbjörnsson, 1979). It is normally represented by a dashpot, where the damping force is in-phase and proportional to the velocity. The function is found by setting  $\theta = 1$  in Equation 2.41.

$$F^D(\dot{u}) = c\dot{u} \quad (2.42)$$

This model is typically used in engineering practice as it results in a linear equation of motion, which is mathematically convenient (Hall, 2006). A good way to explain the properties of this model is to consider the equation of motion for a single-degree-of-freedom (SDOF) system:

$$m\ddot{u} + c\dot{u} + ku = q(t) \quad (2.43)$$

Here  $m$  is the mass coefficient,  $c$  is the damping coefficient,  $k$  is the stiffness coefficient and  $q(t)$  is the applied load. For free vibration only the homogeneous solution is considered.

$$m\ddot{u} + c\dot{u} + ku = 0 \quad (2.44)$$

Assuming  $u = e^{st}$  yields the solution:

$$u = Ae^{s_1 t} + Be^{s_2 t} \quad (2.45)$$

The two roots of this characteristic equation is:

$$s_{1,2} = -\frac{c}{2m} \pm \sqrt{\left(\frac{c}{2m}\right)^2 - \frac{k}{m}} \quad (2.46)$$

$A$  and  $B$  are dependent on the initial conditions. Combining Equation 2.45 and Equation 2.46 results in:

$$u(t) = e^{(-c/2m)t} \left( Ae^{\left(\sqrt{(c/2m)^2 - k/m}\right)t} + Be^{-\left(\sqrt{(c/2m)^2 - k/m}\right)t} \right) \quad (2.47)$$

Now the critical damping coefficient can be defined as:

$$c_{cr} = 2m\sqrt{\frac{k}{m}} = 2m\omega_n \quad (2.48)$$

where  $\omega_n$  is the natural frequency. The damping is often expressed as the ratio of  $c_{cr}$ . It is defined as:

$$\zeta = \frac{c}{c_{cr}} = \frac{c}{2m\omega_n} \quad (2.49)$$

- Supercritical damping  $c > c_{cr}$ : Here, the exponent is real and there is no oscillatory motion.

- 
- Subcritical damping  $c < c_{cr}$ : Here the exponents are imaginary and there will be oscillatory motion. This is the most common case for structural systems (Langen and Sigbjörnsson, 1979).

For subcritical damping the roots of Equation 2.46 will be complex and given as:

$$s = -\zeta\omega_n \pm i\omega_d \quad (2.50)$$

The damped natural frequency is given as:

$$\omega_d = \omega_n \sqrt{1 - \zeta^2} \quad (2.51)$$

The differential equation of motion given in Equation 2.43, now becomes:

$$\ddot{u} + 2\zeta\omega_n\dot{u} + \omega_n^2 u = \frac{1}{m}q(t) \quad (2.52)$$

As mentioned in Section 2.3, the damping is defined by the energy dissipation during one cycle. If a steady state harmonic load is assumed, it can be shown that the hysteresis loop for a linear viscous damper will form an ellipse. Inserting the linear damping force in Equation 2.29 yields:

$$D = \oint F^D du = \pi c \omega u_0^2 \quad (2.53)$$

Combining Equation 2.32 and Equation 2.48 we get a specific damping capacity:

$$\psi = \frac{D}{U} = \frac{\pi c \omega u_0^2}{\frac{1}{2} k u_0^2} = \frac{2\pi c \omega}{k} = 4\pi\zeta \quad (2.54)$$

The loss coefficient is found by combining Equation 2.33 and Equation 2.48:

$$\eta = \frac{D}{2\pi U_{max}} = \frac{\pi c \omega u_0^2}{2\pi \frac{1}{2} k u_0^2} = \frac{c \omega}{k} = 2\zeta \quad (2.55)$$

## 2.4.2 Coulomb damping

Coulomb damping is normally used to model dry friction e.g steel on steel contact. This is a nonlinear model where the damping force is constant and in-phase with the velocity. The force is assumed to be proportional to the normal force  $N$  which acts between two surfaces. The expression for Coulomb damping is found by setting  $\theta = 0$  in Equation 2.41.

$$F_D(\dot{u}) = \mu N \operatorname{sgn}(\dot{u}) \quad (2.56)$$

$\mu$  is the coefficient of friction. For steel on steel contact, the kinematic coefficient is given as  $\mu = 0.57$  (Grigoriev et al., 1997). Figure 2.6 shows the model and the corresponding hysteresis loop.

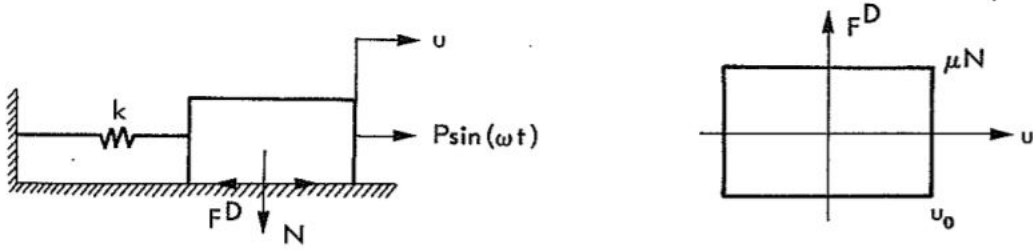


Figure 2.6: Model and hysteresis loop for Coulomb damping (Langen and Sigbjörns-son, 1979)

### 2.4.3 Nonlinear viscous damping

Nonlinear viscous damping means that the damping force is not proportional to the velocity. By setting  $\theta = 2$  in Equation 2.41 the following is obtained:

$$F_D(\dot{u}) = q\dot{u}|\dot{u}| \quad (2.57)$$

This is known as quadratic damping. For marine application an example is the drag force on a slender cylinder found by the Morison equation (Morison et al., 1950). When only considering the drag term the following nonlinear drag force is obtained.

$$dF(t) = \frac{1}{2}\rho C_D D u(\dot{t})|u(\dot{t})| \quad (2.58)$$

### 2.4.4 Equivalent viscous damping

The linear viscous damping model given in Section 2.4.1 is an approximation used for its simplicity during calculations. However, real damping often exhibits a different dependency on frequency and displacement. The equivalent viscous damping is a method of approximating the steady state solution of a nonlinear SDOF system. This is done by evaluating the linear system with respect to the energy dissipation during one cycle of sinusoidal response (Jacobsen, 1930). The damping models mentioned in Section 2.4.1-Section 2.4.3 have following equivalent damping ratios:



Mathematical model	Equivalent damping ratio, $\zeta_{eq}$
Linear viscous damping	$\frac{c}{2m\omega}$
Coulomb damping	$\frac{4\mu N}{\pi m\omega^2 u_0}$
Nonlinear viscous (quadratic) damping	$\frac{4}{3} \frac{qu_0}{\pi m}$

Table 2.1: Equivalent viscous damping ratios

This method is often used for the seismic response of buildings. Studies have shown that use of the equivalent damping ratio can be a good approximation for sinusoidal response (Dwairi, 2004). However, for real earthquakes the method seem to be more unreliable and overestimate the damping.

## 2.5 Forced vibration

So far, free vibration has been assumed with regards to the equation of motion given in Equation 2.43. When a structure is subjected to harmonic loading, one can use the frequency-response method to obtain the natural frequency of the structure. For a linear system, there is a linear relationship between the input and output signal. This is known as the Frequency Response Function,  $H(\omega)$ . Again, if a SDOF system is considered, the equation of motion is given by Equation 2.43. In order to solve the differential equation, the harmonic load  $q(t) = q_0 \cdot \cos(\omega t + \theta)$  is assumed. The frequency response function for a SDOF system is then given by:

$$H(\omega) = \frac{1}{k} \frac{1}{(1 - \beta^2 + i(2\zeta\beta))} \quad (2.59)$$

The derivation of Equation 2.59 is given in Section A. Above, the frequency ratio  $\beta = \frac{\omega}{\omega_n}$  is introduced. For a given load  $F(t) = \Re[X \cdot e^{i\omega t}]$ , the response will be:

$$u_0 = |H(\omega)| \cdot |X| \quad (2.60)$$

Where:

$$|H(\omega)| = \sqrt{\Re(H(\omega))^2 + \Im(H(\omega))^2} = \frac{1}{k} \frac{1}{\sqrt{(1 - \beta^2)^2 + (2\zeta\beta)^2}} \quad (2.61)$$

For a multi-degree-of-freedom system(MDOF) Equation 2.59 can not be simplified, so  $H(\omega)$  will be defined as follows:

$$\mathbf{H}(\omega) = [-\omega^2 \mathbf{M} + i\omega \mathbf{C} + \mathbf{K}]^{-1} \quad (2.62)$$

More on MDOF systems in Section 2.7.

---

## 2.6 Dynamic amplification factor

When structural dynamics in marine structures are considered, the dynamic amplification factor (DAF) is essential in the estimation of the response when using certain methods. The DAF is defined as the ratio between the dynamic response and the static response (Horn et al., 2015). In terms of the frequency response function it can be written as:

$$DAF = \frac{u_d}{u_s} = \frac{|H(\omega)|X}{X/k} = \frac{|H(\omega)|}{|H(0)|} = \frac{1}{\sqrt{(1-\beta^2)^2 + (2\zeta\beta)^2}} \quad (2.63)$$

It is clear from Equation 2.63 that the damping ratio is essential for the accuracy of the structural analysis where the DAF is employed. As an example, the DAFs of a system at resonance ( $\beta = 1$ ) are given with different damping ratios:

Damping ratio $\zeta$ [-]	DAF [-]
0.005	100
0.01	50
0.015	33.333
0.02	25

Table 2.2: DAF for different damping ratios at resonance

The importance of accurate damping ratios becomes explicit as damping clearly affects the estimate of dynamic response at resonance.

## 2.7 Multi-degree-of-freedom system

The equation of motion for a multi-degrees-of-freedom (MDOF) system can be written on matrix form as:

$$\mathbf{M}\ddot{\mathbf{r}} + \mathbf{C}\dot{\mathbf{r}} + \mathbf{K}\mathbf{r} = \mathbf{Q} \quad (2.64)$$

The mass matrix  $\mathbf{M}$ , linear damping matrix  $\mathbf{C}$  and stiffness matrix  $\mathbf{K}$  have the dimensions  $l \times l$ , and the acceleration vector  $\ddot{\mathbf{r}}$ , velocity vector  $\dot{\mathbf{r}}$  and displacement vector  $\mathbf{r}$  have dimensions  $l \times 1$ , where  $l$  is the number of degrees of freedom in the system. This system has  $l$  eigenfrequencies and  $l$  corresponding mode shapes which can be found by solving Equation 2.28. Since the  $l$  different eigenvectors are linearly independent, a linear combination can be used to find the displacement:

$$\mathbf{r} = \sum_{i=1}^l \Phi_i y_i(t) = \Phi \mathbf{y} \quad (2.65)$$

Above,  $\mathbf{y}$  is a vector of  $l$  time-dependent amplitudes, and  $\Phi$  is a matrix containing the mode shapes:

$$\Phi = [\phi_1 \phi_2 \dots \phi_l] \quad (2.66)$$

---

Inserting the transformation in Equation 2.65 into the equation of motion and premultiply by  $\Phi_i^T$  yields the following results:

$$\Phi_i^T \mathbf{M} \Phi \ddot{\mathbf{y}} + \Phi_i^T \mathbf{C} \Phi \dot{\mathbf{y}} + \Phi_i^T \mathbf{K} \Phi \mathbf{y} = \Phi_i^T \mathbf{Q}(t) \quad (2.67)$$

It can be shown that the modes have certain orthogonality properties with regard to the mass matrix and stiffness matrix. Assuming that the same orthogonality properties apply for the damping matrix gives the following characteristics:

$$\begin{aligned} \Phi_i^T \mathbf{M} \Phi_j &= 0 \\ \Phi_i^T \mathbf{C} \Phi_j &= 0 \\ \Phi_i^T \mathbf{K} \Phi_j &= 0 \end{aligned} \quad (2.68)$$

This is valid for  $i \neq j$ , and it results in  $l$  linearly independent equations that can be solved independently. It is noted that the orthogonality property in the damping matrix is only valid under certain conditions. The total system now becomes:

$$\Phi^T \mathbf{M} \Phi \ddot{\mathbf{y}} + \Phi^T \mathbf{C} \Phi \dot{\mathbf{y}} + \Phi^T \mathbf{K} \Phi \mathbf{y} = \Phi^T \mathbf{Q}(t) \quad (2.69)$$

Using the properties from Equation 2.68 in Equation 2.69, the following uncoupled equation system is obtained.

$$\overline{\mathbf{M}} \ddot{\mathbf{y}} + \overline{\mathbf{C}} \dot{\mathbf{y}} + \overline{\mathbf{K}} \mathbf{y} = \overline{\mathbf{F}}(t) \quad (2.70)$$

This can be solved for each degree of freedom. The damping ratio for a given mode shape can therefore be found by solving the corresponding uncoupled equation of motion. The result is the following:

$$\begin{aligned} \bar{m}_i &= \Phi_i^T \mathbf{M} \Phi_i \\ \bar{k}_i &= \Phi_i^T \mathbf{K} \Phi_i \\ \bar{c}_i &= \Phi_i^T \mathbf{C} \Phi_i = 2\bar{m}_i \omega_i \zeta_i \end{aligned} \quad (2.71)$$

$$\zeta_i = \frac{\bar{c}_i}{2\bar{m}_i \omega_i} \quad (2.72)$$

The typical way to represent the damping in a structure is to use the mode shapes, which is done for convenience (Lanzi and Luco, 2017). Previously it has been assumed that Equation 2.68 holds, meaning the undamped mode shapes are orthogonal with respect to  $\mathbf{C}$ . If this is the case, the modal damping coefficient can be found by solving the uncoupled equation system given in Equation 2.70. The more common case is that the orthogonality condition is not satisfied. This will lead to the following:

$$\begin{aligned} \overline{\mathbf{C}} &= \Phi^T \mathbf{C} \Phi \\ \bar{c}_{ij} &= \Phi_i^T \mathbf{C} \Phi_j \neq 0 \end{aligned} \quad (2.73)$$

In order to employ the modal damping coefficient in Equation 2.71 it is implied that the coupling terms  $\bar{c}_i$  are neglected for  $i \neq j$ . The equivalent modal damping

---

---

coefficient  $\bar{c}_i$  is still possible to find from  $\bar{\mathbf{C}}$ . This is done by the Least square method (Malhotra and Joseph Penzien, 1970). The following is a short summary of this procedure.

Assuming that  $\bar{\bar{\mathbf{C}}}$  is a diagonal matrix containing  $\bar{c}_i$  one can write  $\bar{\mathbf{C}}$  as a function of an error vector  $e$ :

$$\bar{\mathbf{C}}\dot{\mathbf{y}} = \bar{\bar{\mathbf{C}}}\dot{\mathbf{y}} + e \quad (2.74)$$

This can be rewritten:

$$e_i^2 = \dot{\mathbf{y}}^T \left( \bar{\mathbf{C}}_i - \bar{\bar{\mathbf{C}}}_i \right)^T \left( \bar{\mathbf{C}}_i - \bar{\bar{\mathbf{C}}}_i \right) \dot{\mathbf{y}} \quad (2.75)$$

Above,  $\mathbf{C}_i$  is row  $i$  in  $\mathbf{C}$ . The smallest time average of the function is then found.

$$\begin{aligned} \left\langle \frac{\partial e_i^2}{\partial \bar{c}_i} \right\rangle &= \left\langle 2 \left( \bar{\mathbf{C}}_i - \bar{\bar{\mathbf{C}}}_i \right) \dot{\mathbf{y}} \dot{y}_i \right\rangle = 0 \\ &\Rightarrow \left\langle \left( \bar{\mathbf{C}}_i \dot{\mathbf{y}} - \bar{\bar{\mathbf{C}}}_i \dot{y}_i \right) \dot{y}_i \right\rangle = 0 \end{aligned} \quad (2.76)$$

This can be solved for  $\bar{c}_i$ :

$$\bar{c}_i = \bar{c}_i + \sum_{j=1, j \neq i}^n c_{ij} \frac{\langle \dot{y}_j \dot{y}_i \rangle}{\langle \dot{y}_i^2 \rangle} \quad (2.77)$$

The equation above is solved iteratively where  $\dot{y}_i$  is found by solving Equation 2.70 for the given mode, and then an improved  $\bar{c}_i$  is obtained.

## 2.8 Methods for establishing the damping matrix

In the previous subsection, the damping matrix was assumed to be known for the modal damping. In order to establish the modal damping matrix, a linear combination of  $\mathbf{M}$  and  $\mathbf{K}$  is used. According to Lanzi and Luco (2017) three different methods are normally used for this purpose.

### 2.8.1 Rayleigh damping matrix

The common way of establishing a orthogonal damping matrix is by representing it as a Rayleigh damping matrix (Rayleigh and Lindsay, 1945). The damping matrix  $\mathbf{C}$ , is assumed to be proportional to the mass matrix  $\mathbf{M}$ . This can be written as:

$$\mathbf{C} = \alpha_1 \mathbf{M} \quad (2.78)$$

The same is assumed for the stiffness matrix:

$$\mathbf{C} = \alpha_2 \mathbf{K} \quad (2.79)$$

---

The coupled relation between the two equations above is given as:

$$\mathbf{C} = \alpha_1 \mathbf{M} + \alpha_2 \mathbf{K} \quad (2.80)$$

This is called Rayleigh damping or proportional damping. The damping matrix will be accurate for low levels of damping (Liu and Gorman, 1995). Similarly to  $\mathbf{M}$  and  $\mathbf{K}$ , the damping matrix  $\mathbf{C}$  has orthogonal properties. Consequently the coefficients will become:

$$\bar{c}_i = \Phi_i^T \mathbf{C} \Phi_i = \alpha_1 \bar{m}_i + \alpha_2 \bar{k}_i \quad (2.81)$$

Moreover, the damping ratio of a given mode  $i$  can be found if  $\alpha_1$  and  $\alpha_2$  are known.

$$\zeta_i = \frac{\bar{c}_i}{2\bar{m}_i\omega_i} = \frac{1}{2} \left( \frac{\alpha_1}{\omega_1} + \alpha_2\omega_2 \right) \quad (2.82)$$

If the damping ratio for two frequencies are known in the domain of interest, it is possible to determine  $\alpha_1$  and  $\alpha_2$ .

$$\begin{aligned} \alpha_1 &= \frac{2\omega_1\omega_2}{\omega_2^2 - \omega_1^2} (\zeta_1\omega_2 - \zeta_2\omega_1) \\ \alpha_2 &= \frac{2(\omega_2\zeta_2 - \omega_1\zeta_1)}{\omega_2^2 - \omega_1^2} \end{aligned} \quad (2.83)$$

Hall (2006) presented a method which aims for a constant damping ratio within a given frequency range. The method is consistent with field data and goes as follows.

Select a desired damping ratio  $\zeta$ , and a frequency range from  $\hat{\omega}$  to  $R\hat{\omega}$ , where  $R > 1$  and the frequency range covers modes important to the response.  $\Delta$  is introduced as the bounds of the damping ratios important to the modes in the specified frequency range.

$$\Delta = \zeta \frac{1 + R - 2\sqrt{R}}{1 + R + 2\sqrt{R}} \quad (2.84)$$

All the modes in the range will be bound by  $\zeta_{bound} = \zeta \pm \Delta$ . If the bounds are narrow enough,  $\alpha_1$  and  $\alpha_2$  can be found by:

$$\begin{aligned} \alpha_1 &= 2\zeta\hat{\omega} \frac{2R}{1 + R + 2\sqrt{R}} \\ \alpha_2 &= 2\zeta \frac{1}{\hat{\omega}} \frac{2R}{1 + R + 2\sqrt{R}} \end{aligned} \quad (2.85)$$

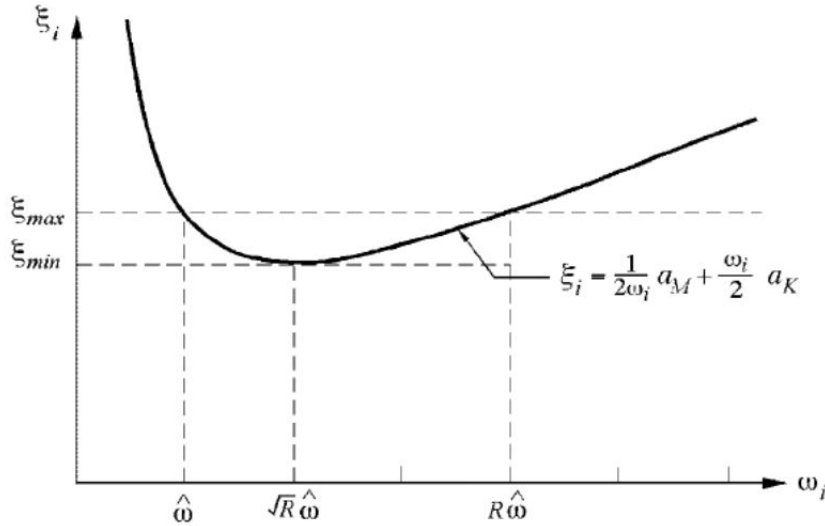


Figure 2.7: Rayleigh damping from (Hall, 2006).

The advantage of Rayleigh damping is that it does not alter the mode shape, making calculations fairly simple (Liu and Gorman, 1995).

## 2.8.2 Caughey series

Caughey (1960) derived the general form of a viscous damping matrix with orthogonal properties for a discrete system. Later, Caughey and O'Kelly (1965) presented Caughey series involving negative or zero powers as a representation of the damping matrix. This is given in the following equation.

$$\mathbf{C} = \mathbf{M} \sum_{l=0}^{M-1} a_l (\mathbf{M}^{-1} \mathbf{K})^l \quad (2.86)$$

Here,  $a_l$  are arbitrary coefficients to be determined, and  $M \leq l$  is the number of terms in the series. As before,  $\mathbf{M}$  and  $\mathbf{K}$  are  $l \times l$  matrices with  $l$  DOF and any desired number of terms can be used in the Caughey series (Wilson and J. Penzien, 1972). It should also be noted that the two first terms of Equation 2.86 give Rayleigh damping.

The coefficient  $a_l$  are evaluated by looking at each mode,  $i$ . This can be done by combining Equation 2.86 and Equation 2.68 (Wilson and J. Penzien, 1972). The result is:

$$\bar{c}_i = \sum_{l=0}^{M-1} a_l \bar{m}_i \omega_i^{2l} = 2\bar{m}_i \omega_i \zeta_i \quad (2.87)$$

Solving for  $\zeta_i$  show that if the damping ratios for all the modes are known, then the coefficients  $a_l$ , can be found from:

---


$$\zeta_i = \frac{1}{2} \left( \frac{a_0}{\omega_i} + a_1\omega_i + a_2\omega_i^3 + \cdots + a_{M-1}\omega_i^{2N-3} \right) \quad (2.88)$$

One important note is that the application of the Caughey series approach is intended for structures with a moderate amount of DOFs, a part of the reason is the numerical difficulties when  $\omega_i^n$  becomes large in Equation 2.88 (Wilson and J. Penzien, 1972). However, the Caughey series approaches can be used at element or substructure level in complex structures (Lanzi and Luco, 2017).

### 2.8.3 Direct evaluation of damping matrix

As a proposal to solve the numerical difficulties Wilson and J. Penzien (1972) presented a method which uses the superposition of modal damping matrices. This method starts by evaluating the normal damping matrix  $\bar{\mathbf{C}}$  from Equation 2.70. The damping matrix then determined from modal damping ratios. The result is:

$$\mathbf{C} = \mathbf{M} \left( \sum_i^N \frac{2\zeta_i\omega_i}{\bar{m}_i} \phi_i\phi_i^T \right) \mathbf{M} \quad (2.89)$$

Term  $i$  represents the contribution from mode  $\phi_i$  in the damping matrix. When a term is not included, it is implied that the given mode has zero damping. In practical analysis, the matrix from Equation 2.89 has not been popular as it is a fully populated matrix and requires all frequencies and modes (Chopra and McKenna, 2016). However, if all these are known, it is less computationally demanding than using Caughey series (Wilson and J. Penzien, 1972).

## 2.9 Measurement of structural damping

There are several ways to measure the damping of structures. This section presents methods for estimation of damping during free vibration and during forced oscillation.

### 2.9.1 Logarithmic decrement

The logarithmic decrement is a common way of obtaining the viscous damping ratio during free vibration. This is done by measuring two successive peak values,  $u_j$  and  $u_{j+1}$ . These instances can be described as functions of the damped natural period.

$$\begin{aligned} u_j &= u(t) \\ u_{j+1} &= u(t + T_d) \end{aligned} \quad (2.90)$$

The damped natural frequency is given in Equation 2.51, and the damped natural period then becomes:

$$T_d = \frac{2\pi}{\omega_d} = 2\frac{\pi}{\omega_n} \frac{1}{\sqrt{1-\zeta^2}} \quad (2.91)$$

---

The solution for the equation of motion given in 2.47, can be rewritten for the subcritical case:

$$u(t) = e^{-\zeta\omega_n t} (A \sin(\omega_d t) + B \cos(\omega_d t)) \quad (2.92)$$

The ratio between two consecutive peaks can now be given:

$$\frac{u_j}{u_{j+1}} = \frac{e^{-\zeta\omega_n t}}{e^{-\zeta\omega_n(t+T_d)}} = e^{\zeta\omega_n T_d} \quad (2.93)$$

Taking the natural logarithm on both sides yields the decrement:

$$\delta = \ln \left( \frac{u_j}{u_{j+1}} \right) = \frac{2\pi\zeta\omega_n}{\omega_d} \quad (2.94)$$

For low levels of damping, the following approximation used:

$$\delta \cong 2\pi\zeta \quad (2.95)$$

Abbreviated series expansion of  $\frac{u_j}{u_{j+1}}$  yields:

$$\delta \cong \frac{u_j - u_{j+1}}{2\pi u_{j+1}} \quad (2.96)$$

The logarithmic decrement is typically applied to estimate the damping of the first vibration mode, which can be modeled as a SDOF system (Liao and Wells, 2011). By comparing an uncertainty analysis with experimental results, it is shown that the number of measured periods effect the uncertainty of the result. In simple terms, the larger the damping the fewer periods should be measured (Tweten et al., 2014).

## 2.9.2 Half-power point method

The half-power point method is a way of determining the damping ratio experimentally during forced vibration. The method uses the width of the peak value of the frequency response function for a given structure (Papagiannopoulos and Hatzigeorgiou, 2011). The approach is based on obtaining the maximum amplitude related to the natural frequency of the system. In addition, the two frequencies that corresponds to the maximum amplitude divided on the square root of two (Olmos and Roesset, 2010). These are shown in Figure 2.8.



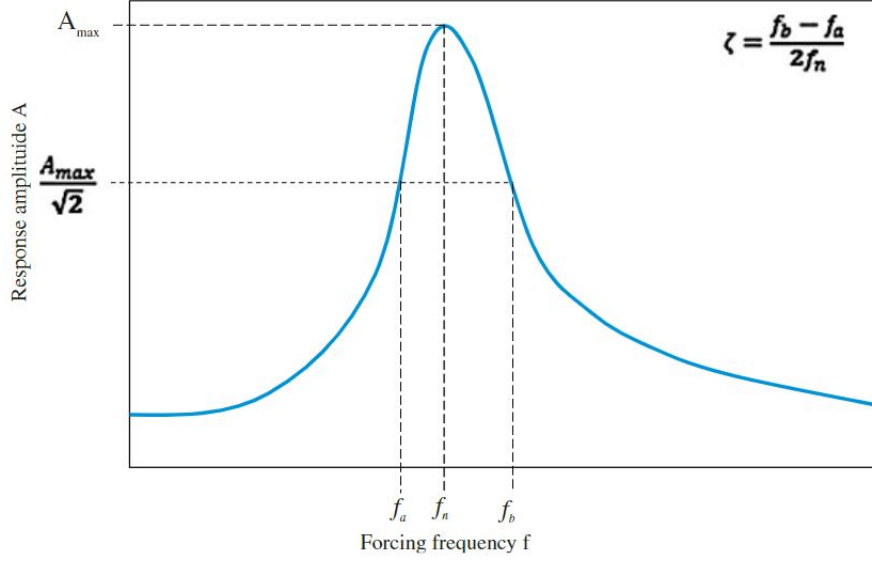


Figure 2.8: Response-frequency curve in half-power bandwidth method (Olmos and Roesset, 2010)

From the magnitude of the frequency response function Equation 2.59, one can derive the damping ratio:

$$H = \frac{1}{\sqrt{\left[1 - \left(\frac{\omega}{\omega_n}\right)^2\right]^2 + \left[2\zeta \left(\frac{\omega}{\omega_n}\right)\right]^2}} \quad (2.97)$$

The magnitude of the frequency response at resonance is therefore  $H = \frac{1}{2\zeta}$ . By taking the square on both sides of Equation 2.97, the following is obtained:

$$\begin{aligned} \left(\frac{1}{2\zeta}\right)^2 &= \frac{1}{\left[1 - \left(\frac{\omega}{\omega_n}\right)^2\right]^2 + \left[2\zeta \left(\frac{\omega}{\omega_n}\right)\right]^2} \\ \Rightarrow \left(\frac{\omega}{\omega_0}\right)^4 - 2(1 - \zeta^2) \left(\frac{\omega}{\omega_n}\right)^2 + (1 - 8\zeta^2) &= 0 \end{aligned} \quad (2.98)$$

Solving for  $\left(\frac{\omega}{\omega_n}\right)$  gives the result:

$$\left(\frac{\omega}{\omega_n}\right)^2 = (1 - 2\zeta^2) \pm 2\zeta\sqrt{1 - \zeta^2} \quad (2.99)$$

By assuming  $\zeta \ll 1$ , the higher order terms can be neglected:

$$\left(\frac{\omega}{\omega_n}\right)^2 = 1 \pm 2\zeta \quad (2.100)$$

---

The roots of Equation 2.100 are now  $\omega_a$  and  $\omega_b$ . Given that  $\omega_a < \omega_b$  the following is obtained:

$$4\zeta = \frac{\omega_b^2 - \omega_a^2}{\omega_n} \cong 2 \left( \frac{\omega_b - \omega_a}{\omega_n} \right) \Rightarrow \zeta = \frac{\omega_b - \omega_a}{2\omega_n} = \frac{f_b - f_a}{2f_n} \quad (2.101)$$

The half-power method can be used for SDOF structures and MDOF structures with linear viscous damping. This also includes structures that do not have classical normal modes, meaning that the damping matrix is not uncoupled. The method is proven to provide accurate results in both field and laboratory tests (Olmos and Roesset, 2010).

## 2.10 Structural damping in welded marine structures

So far the known theory around damping mechanisms and the mathematical modeling of damping is covered. However there are parts of the damping phenomena that are still unknown and highly relying on observations and conservatism. Especially regarding the connection between the material damping and the damping ratio for real structures. Here, the damping ratio,  $\zeta$ , is of main interest as this determines the DAF. The following section presents a literature review of common damping ratios used in welded marine structures. Other comparable structures are also investigated. In addition, the results from a previous full scale experiment is presented.

### 2.10.1 Commonly used damping levels

First, a look into the work done on the dynamics of floating Bridges. Langen and Sigbjörnsson (1980) started to look at the stochastic dynamic response of the Salhus Bridge outside Bergen. Here, the structural damping was seen to be small compared to the hydrodynamic damping and was therefore neglected. In recent years, researchers at the department of structural engineering at NTNU have continued this work. Viuff, Leira et al. (2016) looked at the dynamic response of another floating bridge in Norway. In this study, the damping ratio was assumed to be 2% and Rayleigh damping was used.

One year later, a study using a operation modal analysis was performed on the same bridge by Kvåle et al. (2017). However, the structural damping was not separated from the hydrodynamic damping. The most promising for finding an estimate for the structural damping used on floating bridges was in Viuff, Xiang et al. (2018). Here, a comparison of an analysis using Simo-Riflex and Orcaflex floating bridge concept across Bjørnafjorden was made. For both analysis, Rayleigh damping is used. Mass proportional damping was set to 0.0025 and the stiffness proportional damping is set to 0.2. This results in a damping ratio of  $\zeta < 0.2$  in the frequency

---

range of both the natural periods and the wave-excitation.

Another possible source of insight on the structural damping is seismic response of tall steel buildings. The seismic waves on these buildings will have longer periods than wind loads and can therefore be in the range of interest for marine applications, i.e 1-10 second. In Suda et al. (1996), data from full scale measurements were compared. When looking at the damping ratio, compared to parameters such as natural period and building height there was a trend of the damping ratio being reduced as the building got taller, e.g for buildings that approached 300 meters the damping ratios approached 1 %. However, there was a lot of scatter in the measurements. In addition, the amount of available data was not satisfactory for making a good statistical model. Soil foundation was pointed out as an important factor for the damping ratio, which makes the result not applicable to floating structures.

A later study on buildings in Japan looked at damping measurements (Satake et al., 2003). As before, there was a trend of the damping reducing with the height and natural frequency of the building. However, it should be noted that 2% damping is pointed out as the normal design damping used for tall steel framed buildings. The same value is assumed for the steel deck of a bridge in in Qin and Lou (2000).

As mentioned, soil foundations can be a cause of uncertainty. In addition, the use of bolted connections will give a larger interfacial coulomb damping compared to welded connections. Bolted connections are more commonly used in civil engineering, than naval architecture. In marine structures, stiffened panels are normally used. The structural damping of ship hulls are normally assumed to be small (i.e  $\zeta \ll 1$ ), as in the vibration analysis done by Yucel and Arpaci (2013).

## 2.10.2 Previously conducted experiments

A similar experiment to the one in this thesis was conducted by Ehnes (2003). Here, measurements on a stiffened plate panel was done to establish the damping in welds on war ships. Both free vibration and forced vibration was measured and Rayleigh damping was used as the mathematical model. The panel used was a 1/4 scale of a generic warship panel. The plate was 1.2192m by 2.5908m and had a thickness of 2.8mm, a flat plate was used for comparison. For the free vibration test, the logarithmic decrements was used. The half-power bandwidth method was used for forced vibration. It was noted that the free vibration results were not cohesive and therefore dropped.

The conclusion was that the welds seemed to contribute to the damping, and that Rayleigh damping was an appropriate model. Another important finding was that the increase in damping was in the whole structure, and not a local phenomena. The largest damping was found for low frequencies. The most important statement was that compared to a flat plate, the damping was not significantly increased.

The findings above show that the knowledge about the "step" from material damping to the damping of whole structures is still relying on measured data. There is also a clear lack of research on the field. The mentioned experiment is seen as the most

---

relevant for the current project. However, the scope is somewhat different as the current experiment will be used along a FE model.

# Chapter 3

## Experiment

During Spring 2022, a series of experiments were conducted on a cantilever beam at the Department of Marine Technology in Trondheim. In the following chapter, a description of the beam, welding and hardware will be presented. In addition, there is a description of the performed tests and possible error sources.

### 3.1 Context and hypothesis

The goal of the experiment was to establish methods for estimation of damping in full scale steel structures. By conducting an experiment with a cantilever I-beam, the damping levels were to be determined at different support configurations using the logarithmic decrement and half-power point method. In addition to the material damping described in Section 2.3, a hypothesis is that there was additional damping caused by the relative motion at the interface between the beam and the plate. It was expected that the damping levels found from only one beam would be small, however given that the hull of a VLFS contains a large number of welded plates the total effect might be significant.

### 3.2 Experimental setup

The setup consisted of a 1.53 m cantilever I-beam welded to a thick plate, which again was bolted to a testing rig. The beam had an I-profile. At the beam tip, an exciter was placed. There were fillet welds connecting the beam to the plate at each side of the web and on the top flanges and bottom flanges. The thickness of the web was 5.3 mm. Top and bottom flanges taper from 7.5 mm close to the web to 7.0 mm on the flange edge. The setup and measurements are shown in the following figure and table.

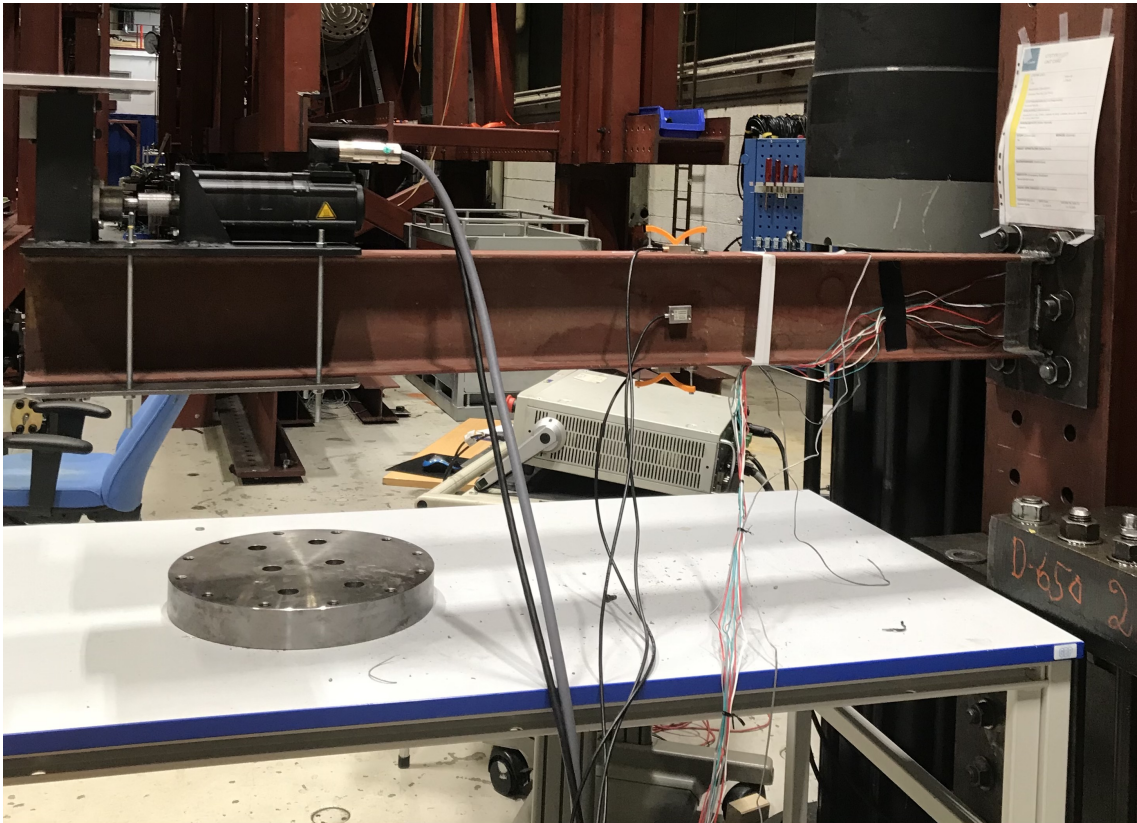


Figure 3.1: Cantilever beam with exciter

Part	Dimension [mm]	Comment
Beam length	1512	
Beam height	160	
Flange width	80	
Flange thickness	7.5-7	Tapering from centre
Web thickness	5.3	

Table 3.1: Beam dimensions

### 3.3 Welding

Fillet welds were used as the welding technique. During the project, the welds were elongated one time. The first setup had two welds on the top flange and two on the bottom flanges. In addition there were two on each side of the web. This setup will be referred to as *weld configuration 1*. Figure 3.2 and Figure 3.3 show the welds and numbering.

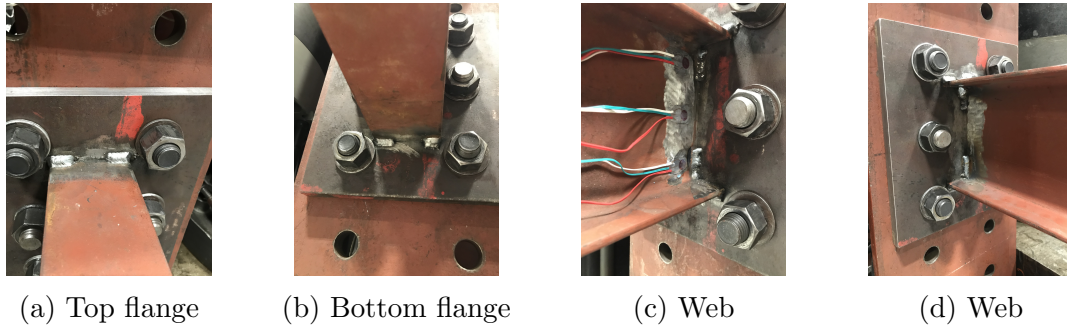


Figure 3.2: Weld configuration 1

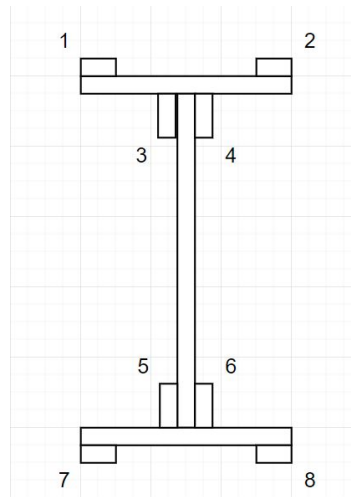


Figure 3.3: Sketch with numbering of welds as seen from tip towards clamped end.

Measurements of the length and throat(a-measurement) of the welds are given in the following table.

Weld number	Length, $L$ [mm]	Throat, $a$ [mm]
1	24	4.6
2	26	6
3	34	5.3
4	36	4.8
5	37	5.6
6	36	4.6
7	27	4.5
8	22	8

Table 3.2: Weld measurements, weld configuration 1

As the welds had uneven thickness, Table 3.2 show the average a-measurements, which were measured at each end and in the middle of the welds. The welds were made with minimal burn-in as a result of the dimensions of the flanges and web.

---

With too much burn-in the metal would be continuous between the beam and the plate, i.e. there would not be a steel-on-steel contact between the beam and the plate.

After conduction test on the beam with smaller welds a continuous weld was made around the beam end. The new arrangement will be referred to as *weld configuration 2* and can be seen in the following figure.

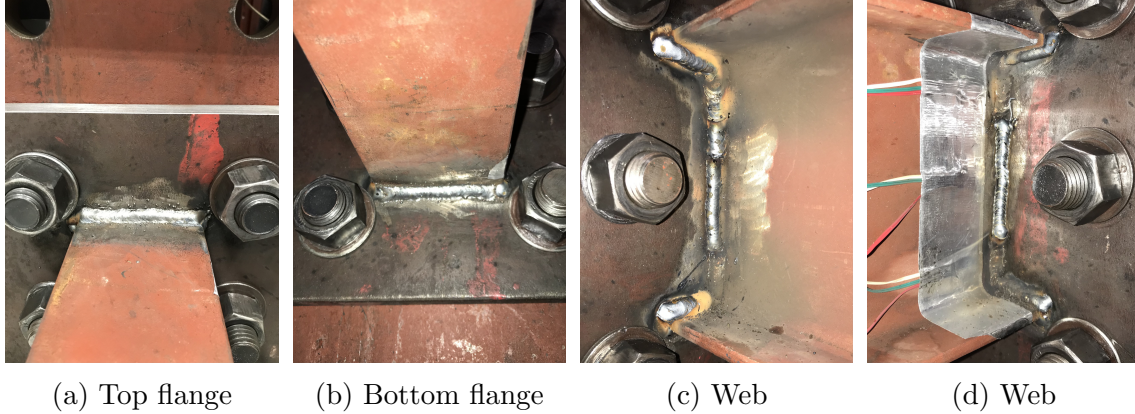


Figure 3.4: Welds along all of beam

### 3.4 Hardware

The servomotor shown in Figure 3.1 was a *Lenze MCS-09H60-RS0B0-B14N-ST5S00N-ROSU*. This had maximum rotational frequency of 6000 rpm, which corresponds to 628.3 rad/s. The weight of the exciter and servomotor was  $m_e = 19.8$  kg. A control unit enabled the motor to be adjusted to the desired frequency. The motor was clamped to the end of the beam by two plates, where the length of the plates were 0.4 m. The three acceleration sensors were of type *KAS903-02A*. They were placed on the top flange, the bottom flange and on the web 0.733 m from the clamped end. The sensors can be seen in Figure 3.5.





Figure 3.5: Acceleration sensors

The strain gauges were one *Tokyo Measurement Instruments Lab general use strain gauge* at the top flange 0.4 m from the welds and one at bottom flange 0.4 m from the clamped end. In addition there were three *Tokyo Measurement Instruments Lab rosettes* located 0.0215 m from the welds at the web. The placement of hardware on the beam is shown in the following figure.

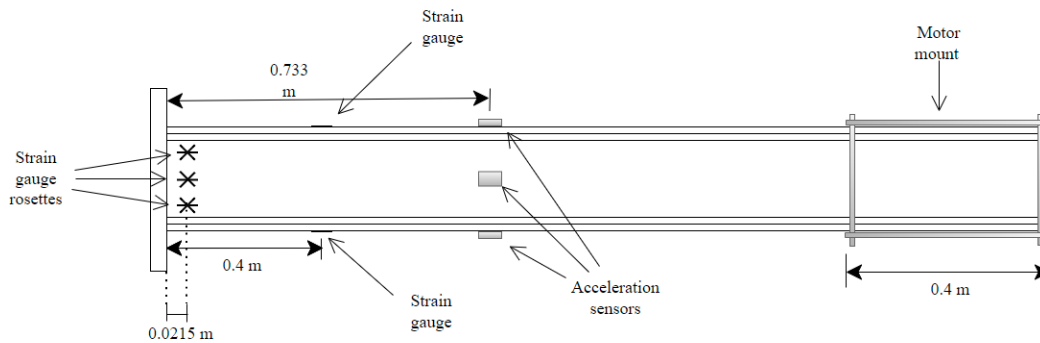


Figure 3.6: Sketch of beam with hardware

All signals from acceleration sensors and strain gauges were sent through amplifiers and gathered using catman®Easy software. This software enable for live visualization of the sensors. In addition the data could be exported to excel for further editing. During testing the sample rate was set to 1200 Hz. This was done on the basis of initial test were the natural frequency of the beam was measured to

---

around 34 Hz, a ratio of 35.3 between the sampling rate and vibrations of interest was considered adequate.

## 3.5 Experimental methods

### 3.5.1 Static deflection

An import part of establishing the properties of the system was to investigate the bending stiffness,  $EI$ , and the rotational stiffness,  $k_\theta$ , of the cantilever beam as described in Equation 2.4. This was done by a static deflection tests where three weights were placed in order on top of the motor as described Table 3.3. The radius of the weights were 8 cm, and they were placed with the edge flush to the beam tip. Furthermore, the relative deflection was measured at a distance of 55 mm from the beam tip using an analogue micrometer. The procedure is shown in Figure 3.7.

Step	weight [kg]
1	2.43
2	4.87
3	7.26

Table 3.3: Weights

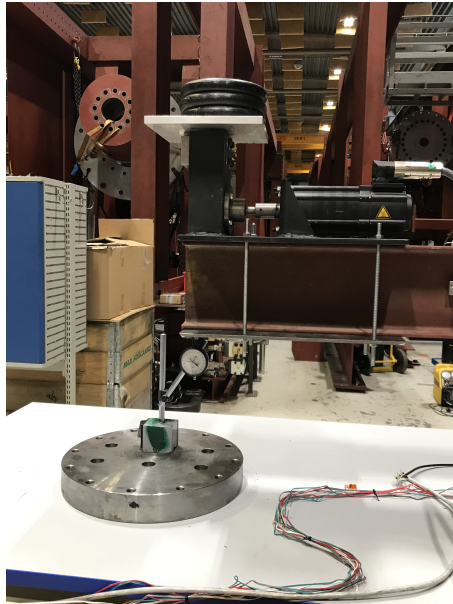


Figure 3.7: Measurement of tip deflection

The strains in the flanges was obtained by measuring for one second with a sample rate of 1200 Hz. Measurements of each step was performed three times, with reset of the strain gauges after each run. Both the deflection and strain measurements were done simultaneously for consistency. It should be noted that all the deflection tests

---

were performed with the motor mounted. This was done for practical reasons, and was considered as not important as only the difference in deflection was of interest.

### 3.5.2 Free vibration

In order to establish the natural frequency of the beam and to estimate the damping by the logarithmic decrement a free vibration test was performed. The logarithmic decrement is described in Section 2.9.1. In order to produce free vibration, the beam was hit at the top flange with a hammer. During the test, measurements were done for 5 s with a sample rate of 1200 Hz. In total, six tests were conducted for each weld configuration. Three were performed before any other testing, the latter three was performed in between other tests in order to investigate possible changes in the natural frequency.

### 3.5.3 Forced vibration

Damping levels of the beam were also found using the half-power point method described in Section 2.9.2. These tests were conducted by running the exciter at different frequencies. The load frequency was controlled manually where the frequency increment was 0.1 Hz. With help from live visualization of the results it was possible to see when steady state was achieved, further identification of steady state was done during post processing. From observations it was noted that steady state was usually achieved rather quickly. The sampling rate was 1200 Hz.

## 3.6 Post processing

The raw data from all sensors were stored in excel files, which enabled for easy editing. In order to reduce computational time, the files were edited so only the steady state response was saved. The excel files were then imported to Python and treated there. The relevant codes are found in B. Before further processing a butterworth lowpass filter was used on all the measurement. This filter was set at 100 Hz on the basis of the measured natural frequency during initial testing. Looking at the mechanical transfer function given in Equation 2.62 the resulting  $\beta = \frac{100}{35}$  would give about  $\frac{1}{7}$  of the undamped resonant response of the system.

### 3.6.1 Static deflection

The strains during static loading was found by taking the average of the measured strain at the top flange. For comparison the analytical strain was calculated using Equation 2.5. The measured deflection was found by taking the average of the measured deflections from multiple tests. After a an adequate number of deflection

---

measurements were acquired, the beam stiffness and rotational stiffness could be calculated using Equation 2.1 and Equation 2.4.

### 3.6.2 Natural frequency

The natural frequency of the beam was found by considering the free vibration initiated by the hammer hit. By performing a fast fourier transform the natural frequency was identified as the maximum of the response spectrum.

### 3.6.3 Logarithmic decrement

For the logarithmic decrement the data was extracted in the same way as previously described. Afterwards the built-in function *Scipy.signal.find\_peaks()* was used to find the peaks of the signal. Furthermore the positive peaks of the response were identified in order to obtain the damping as described in Equation 2.95. During post processing of the results, it was observed that the damping ratio was dependent on the number of positive peaks counted. This led to a convergence study with a limit of 5% deviance between the calculated damping ratios.

### 3.6.4 Half-power point

From the raw data captured during forced vibration the steady state response was identified from the time series, and transient displacement was deleted. The response amplitudes used for the half-power point method was then found by dividing the absolute value of the max and minimum steady state response by two. This was done for each load frequency. The half-power point and corresponding damping was calculated as described in Equation 2.101. This procedure was done for the strain at the flanges and for the vertical acceleration.

## 3.7 Sources of error

Different sources of error could effect the accuracy of the obtained results. In the following section, uncertainties in the experimental setup and methods will be mentioned. Discussion of the specific effect these could have on the results will be discussed in chapter 5.

### 3.7.1 Material and geometry

Firstly, the materials and geometry of the beam contained some uncertainties. With limited knowledge of the steel alloy of the beam and plate a Young's modulus of  $E=210$  GPA and Poisson ratio of  $\nu = 0.3$  was assumed. The accuracy of the bending

---

stiffness  $EI$ , could have effected both static response and the dynamic response as can be seen in e.g. Equation 2.2 and Equation 2.25.

The geometry of the beam could also have affected the results, especially if the flanges and web were bent. This would result in a transverse load and possible torsional movement of the beam. This effect could be present both during the free vibration and forced vibration. The beam end not being perfectly even could also have a consequence for contact behaviour at the interface. Irregularities in the surface could make the contact area between the beam and plate smaller than expected.

### 3.7.2 Welds

Another uncertainty in the experiment were the geometry of the welds. First, the weld shape was irregular which made taking accurate measurements with calipers challenging. The length and a-measurement was therefore used as these were the easiest to obtain. For the a-measurement, the average of the depth at each end and center was used as previously mentioned. The uneven welds could have lead to torsional movement during loading and uneven stresses around the weld.

Cracking was observed in the welds near the flanges during testing. A cracked weld could result in torsional movement as one side of the flange would not be held in place when the given flange was in tension. Given that the damping calculations were made from vertical measurement this could effect the results. As a result of cracking, it was decided to reconstruct weld number 2 and weld number 7. These welds can be seen in Figure 3.3. All presented results are from tests conducted after this reconstruction. Note that possible internal cracks in other welds could still have been present in the remaining welds. Consequently, both the response of the beam and the stresses in the weld could be effected.

### 3.7.3 Measurements

In an attempt to keep the errors in the measurements to a minimal, resetting of the gauges and acceleration sensor were conducted after each test. It should be noted that after resetting the channels, live update of the sensors still showed some fluctuations in the signal. This noise creates uncertainty in the accuracy of the signal given the small magnitude of measured strain and acceleration. This uncertainty was prominent during static deflection test and free vibration test where the magnitude of the deflection was small.

For the static deflection the measurement using a micrometer could have been uncertain as a result of inaccurate reading. Possible errors are the micrometer being at an angle and small movements in the base of the micrometer. These uncertainties were reduced by taking the average of multiple measurements.

The way the free vibration tests were conducted also include some inherent uncertainties. As the test was performed by hitting the beam with a hammer, both the

---

force and contact points were uncertain. The force could have been inconsistent for each hit, resulting in a different magnitudes of the response. This could have lead to different damping values if the decay of the beam was dependent on amplitude. In the case of an off-center hammer hit, torsional movement could have resulted in wrong damping ratios if the vertical vibration was effected.

For the forced vibration, the main source of error is believed to be not achieving steady state. While changing frequencies it was observed a transient with larger response than the following steady state. This effect was especially critical close to resonance as unnecessary testing on these frequencies was avoided. Misalignment of the motor could also introduce torsional movement. The mentioned cracking of welds were also important during this test, given the high stresses during resonant testing.

# Chapter 4

## Finite element analysis

The FEA software Simulia Abaqus CAE 2019 was utilized for modelling the beam in weld configuration 1. In order to obtain greater understanding of the Abaqus model, a description of the model and procedures is presented in the following chapter. The accuracy of the model is discussed in Section 5.5.3.

### 4.1 Model description

The model consisted of two parts, a plate and a beam. The plate had dimensions 0.2m x 0.2m with a thickness of 30 mm. Welds were modeled as triangular prisms, where the size was the average sizes found from the experimental setup. This led to different sizes for the horizontal and vertical welds. The vertical welds had height and width of 6 mm and length 35 mm. The horizontal welds had height and width 8 mm mm and length 25 mm. Sketches of the weld profiles are given in Figure 4.1.

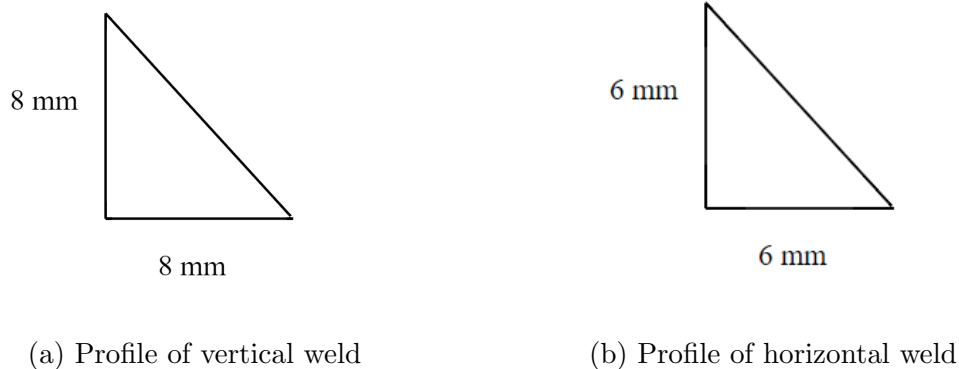


Figure 4.1: Profile of welds

In order to capture the movement in the interface between the plate and the beam, the two parts had to be merged together as if the steel was continuous from the plate, through the welds and into the beam. This was to be achieved by merging

---

the welds to the plate, and later using the *Tie* constraint to connect the beam to the welds. More on the *Tie* constraint in Section 4.5.

The beam was a 1.512 m long I-beam with the almost the same measurements as given in Table 3.1. Only difference was the size of the flanges, instead of tapering the thickness was 7.25 mm. This was done to ease the meshing.

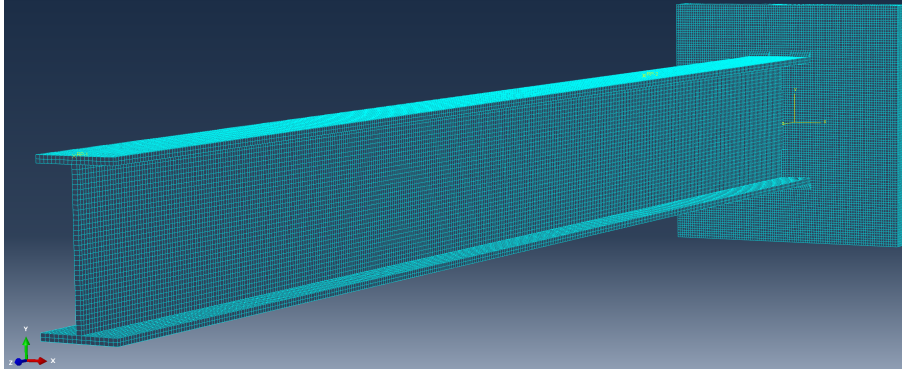


Figure 4.2: FE model

## 4.2 Elements

For the Abaqus analyses a proper element had to be used in order to achieve the highest possible accuracy in the analysis. In Abaqus, solid elements can be used for both linear -and nonlinear analysis. They are categorized by the shape and number of nodes. The elements have either first-order(linear) interpolation or second-order(quadratic) interpolation. The order denotes the shape function of the element. Second order elements provide higher accuracy, and are better at catching stress concentrations than first order elements. However, they have a longer running time (MIT, 2021c).

Reduced integration uses a lower-order quadrature rule to integrate over the element. This is done for the stiffness matrix, however the mass matrix is fully integrated. By using this method the running time will be reduced, especially in three dimensions. After talking to the supervisors quadratic reduced integration elements are seen as the most suitable for this analysis. This element is named *C3D20R* in Abaqus. During the end of the master thesis work it was noticed that the elements in plate were set to first order by mistake, which could effect the results. As the dynamic analyses are quite extensive there was no time to run the analyses again, meaning this could be a source of inaccuracy in the results. There was time to run the static analyses with *C3D20R* elements in both the plate and the beam.

## 4.3 Mesh

The mesh is made such that there are two elements over the flange thickness in order to obtain accurate stress and pressure. For the web there is only one element across



---

the width. This is seen as adequate since the loading was purely vertical, i.e the stress and pressure differences across the web height are captured. The mesh was kept simple by using the same mesh size for the rest of the parts. This is done in order to avoid distorted elements. The resulting mesh has a characteristic length of 3.333 mm, and the complete model had 141495 elements. The following figure show the mesh near the welds.

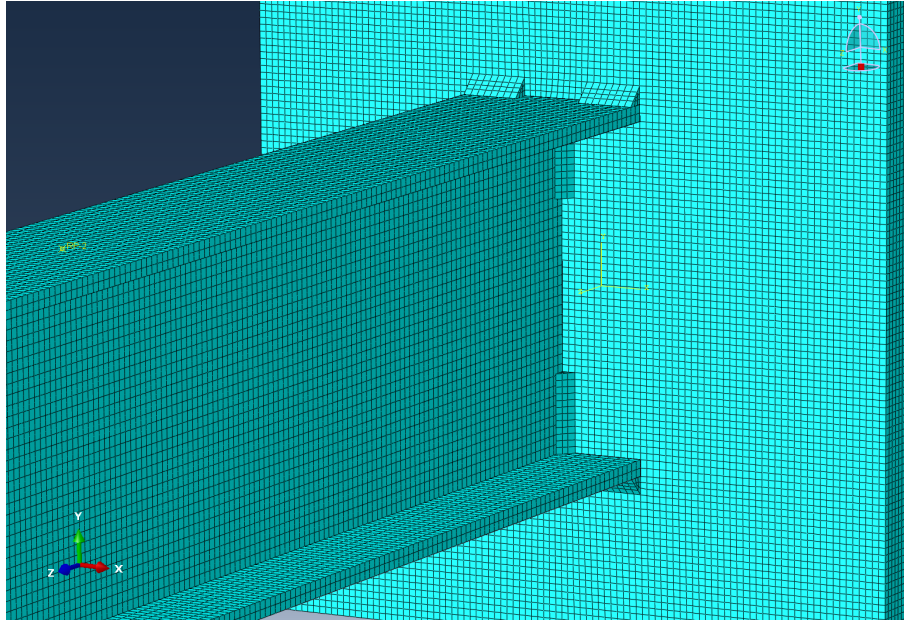


Figure 4.3: Mesh near clamped end

## 4.4 Dynamic analysis

In Abaqus there is the possibility to choose between implicit and explicit time integration. Both come with their advantages and disadvantages (MIT, 2021b). First, the run-time has to be considered. In implicit dynamic analysis a set of nonlinear equilibrium equations and the integration operator matrix is inverted and solved at each time increment. In an explicit dynamic analysis there is no forming or inverting of global mass and stiffness matrices, making each time-increment relatively inexpensive compared to the increments in an implicit integration scheme. However, the implicit operators are unconditionally stable for linear systems. Consequently the time step can be larger compared to the central difference scheme used in explicit analysis. Initial testing of using explicit analysis showed time steps around  $10^7$  s. This was with automatic regulation of the time step in Abaqus. Since the available computational power was a computer with 10 processors, the lower computational cost of each explicit increment did not make the total analysis time practical. Consequently, it was decided to use implicit analysis in this project. However, this decision was made early in the project in order to focus on the contact formulation. Explicit analysis should therefor not be excluded as a viable option.

In Abaqus, the default time integration for implicit is Hilber-Hughes-Taylor time integration (Hilber et al., 1977). This method has some numerical damping, luck-

---

ily this can be avoided by editing the numerical parameters associated with the operator. By setting  $\alpha = 0$  there should be no numerical damping.

## 4.5 Constraints

Constraints on the degrees of freedom can be used to bind different surfaces together. This can be useful as the intent of the model is to connect the plate and beam by the weld. The *tie* connection fuses two surfaces together, even if the meshes are unequal (MIT, 2021d). In order to connect the welds to the beam the tie constraint is found the most useful as it ensures that the same displacement is maintained for connecting parts (Abdul Kudus, 2020). The reason for the welds to be merged into one part with the plate was convergence difficulties that likely came from two constraints on the welds, i.e two different tie constraints on neighbouring nodes.

## 4.6 Damping in Abaqus

Rayleigh damping is used for material damping in direct integration dynamic analysis in Abaqus. It is possible to define  $\alpha_1$  and  $\alpha_2$ . During analysis the stiffness proportional damping found by solving Equation 2.82 for  $\alpha_2$  given  $\alpha_1 = 0$ . Here the damping level needs to be known, meaning that this feature could be useful in a parametric study.

## 4.7 Contact formulation

The interaction between the beam and plate needs to be modelled as precisely as possible in order to obtain the behaviour of the steel-on-steel friction. This is particularly important for the normal direction of the surfaces. Codes that can handle contact problems mainly use either the penalty method or the Lagrangian multiplier method (Wriggers, 1995). The penalty formulation introduces a spring stiffness between the two contacting bodies. The result is that the final equations do not contain additional variables, simplifying the implementation. However, one drawback of the method is that the accuracy of the approximate solution depends strongly on the penalty number (Huněk, 1993). In addition, the constraint conditions are only approximately satisfied, meaning penetrations are unavoidable.

The Lagrange multiplier method fulfills the contact condition exactly. Here, an additional constraint equation allows no contact to occur (Jiang and Rogers, 1988). However, this increase in size of the equation system leads to increased computational time.

A third option for normal contact constraint is the augmented Lagrange method. Information regarding this formulation in Abaqus was found in MIT (2022) and goes as follows. Simply put this method uses an augmentation iteration scheme in order

---

to reduce the penetration distance between the contact surfaces. For each increment the following sequence takes place. First, the solver uses the penalty method in order to find a converged solution. Furthermore, the penetration between the surfaces is checked. If the penetration of the surfaces is not within a given tolerance the contact pressure is augmented and more iterations are conducted until another convergence. This procedure is continued until the penetration is within the tolerance.

It was attempted to use the Lagrangian multiplier during the project work. However there was problems getting the solutions to converge. It should be mentioned that Abaqus CAE prints a warning about possible convergence issues while using Lagrangian multipliers. Penalty formulations are recommended instead. A lot of time had been spent during the project work trying to use Lagrangian multipliers. Consequently, it was therefore decided to use augmented Lagrange contact formulation in the normal direction close to the end of the project. This lead to a somewhat limited number of analyses. The tangential contact formulation is not critical when it comes to penetration. It was therefore decided to use penalty as frictional contact in order to simplify the calculations.

Different choices and parameters had to be decided for the augmented contact formulation. Given the somewhat limited time, default parameters were decided on as a start. Firstly, the choice was made the option *surface-to-surface* contact discretization. As explained in MIT (2021a), the *surface-to-surface* formulation uses a master slave relationship between the contact surfaces. Here, the method enforces contact conditions in an average sense over regions nearby slave nodes. Each contact constraint will predominantly consider one slave node but will also consider adjacent slave nodes in the region of averaging, which is centered approximately on slave node.

Another parameter is the tracking approach. There are two options in Abaqus, where *Finite-sliding tracking approach* is the most general approach (MIT, 2021a). This approach allows for contact between all points on both surfaces. The other option is the *Small-sliding* approach. This sets a limit to the tracking of the surfaces, which in turn reduces computational cost. Since the sliding in the interface of the beam was unknown it was decided that the best option was to use *finite-sliding*, even given the extra computational cost.

## 4.8 Analysis procedures

In the following, the specific procedures used for the static deflection and free vibration. The previously mentioned settings are valid for both cases.

### 4.8.1 Static deflection

For a static deflection test a static nonlinear stress analysis is performed in Abaqus. The procedure is done to replicate the tests described in Section 3.5.1. The weights were modelled as a pressure force on top of the beam using the *total force* option

---

which divides the input force across a given surface. The area had dimension 16 cm x 8 cm, equal to the diameter of the weights. Gravity is set to be  $g=9.81 \text{ m/s}^2$  when calculating the force. The load can be seen in the following figure.

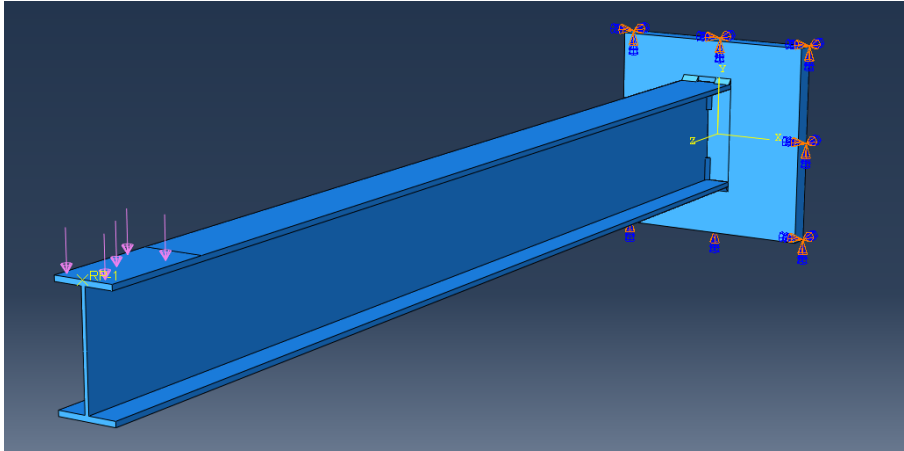


Figure 4.4: Beam with static pressure load

The static analysis had a duration of 0.5 s where the load was applied linearly over the whole step. The suggested initial time step was set to  $5 \cdot 10^{-7}$  s with a minimal allowed step of  $1 \cdot 10^{-7}$  s. If the time step was not sufficiently small during initial contact, there was trouble with convergence. Abaqus regulated the size of time-step in order to reduce run-time of the analysis. In order to reduce the time for each analysis, a maximum allowed time-step 0.1 s was used.

## 4.8.2 Numerical eigenfrequency

In order to obtain the natural frequency of the beam a the Lanczos eigensolver was used. Here the mass of the motor is modelled as inertia in a node 54893, located 19.747 cm from the tip. As the real center of gravity is unknown for the motor this was an assumption as the motor length was 40 cm.

## 4.8.3 Numerical free vibration

For the free vibration a combination of a static load step and dynamic implicit vibration step was used. During the static step, deflection in the form of a boundary condition at the tip was introduced. The displacement of the tip was set to 1 mm downward. The use of a boundary condition instead of a load was from convergence considerations. This static step had a length of 0.4 s.

The static step was followed by a implicit dynamic step. This step involved no load, only a inertia located as the same position as previously mentioned. The time steps will be discussed in Section 5.5.3.

---

## 4.9 Methodology

Abaqus is a comprehensive CAE software providing many options during analyses. The main goal of the numerical model is to investigate if it is possible to obtain and identify the damping from different sources for welded steel structures. A summary of the methodology and decisions that were taken during work on the model are presented below.

1. Establish the properties of the model that was kept constant during further investigation. While working with the model it was decided that the parts, assembly, mesh and boundary were to be kept constant due to limited time. The same goes for the contact properties. As mentioned, Lagrangian multipliers lead to convergence issues. Consequently it was decided that Augmented Lagrange contact formulation was to be used in the normal direction and penalty formulation in the tangential direction.
2. The loading for the different procedures were decided on. These are described in Section 4.8.
3. A static analysis was conducted in order to verify the accuracy of the model and contact formulation. This was done by comparing the numerical deflection to analytical results and experimental results.
4. For the dynamic analysis multiple input options available for the contact surface and damping. The experimental results could not indicate if the damping in the beam was from material damping or steel-on-steel friction. The task of identifying the different contributions to the damping was therefore quite hard. The way this was done was to first run an analysis without using material damping. Afterwards the damping was obtained for this basic model using the same methods as for the experimental tests, i.e logarithmic decrement. It was planned to use the difference in the damping results to indicate the magnitude of damping from material damping and damping from movement.

# Chapter 5

## Results and discussion

Presented in this section are the results and discussion from the three different tests. First, the analytical results, experimental results and numerical results for the static deflection test. Afterwards, the experimental results from free vibration and forced vibration. Lastly, results and discussion of the numerical simulations are presented.

### 5.1 Static deflection

#### 5.1.1 Analytical results

As a check for the quality of the beam setup, analytical calculations were conducted in order to obtain the deflection of the beam. As described in Section 2.1, simple hand calculations can be done for both the deflection and strain at various positions. The following dimensions and material properties were used in the calculations.

Dimensions and properties	Size
Young's modulus, $E$	$210 \text{ GPa}$
Moment of inertia, $I$	$9.9 \cdot 10^6 \text{ mm}^4$
Density, $\rho$	$7850 \text{ kg/m}^3$
Area, $A$	$2008 \text{ mm}^2$

Table 5.1: Dimensions

The analytical end deflections and corresponding weights were calculated using Equation 2.2 and Equation 2.5. The following results were obtained.

---

Weight [kg]	$\delta[m]$	$\Delta\delta[m]$	$\varepsilon[-]$	$\Delta\varepsilon[-]$
2.43	$13.21 \cdot 10^{-6}$	0	$1.020 \cdot 10^{-6}$	0
4.87	$26.48 \cdot 10^{-6}$	$13.27 \cdot 10^{-6}$	$2.044 \cdot 10^{-6}$	$1.024 \cdot 10^{-6}$
7.26	$39.47 \cdot 10^{-6}$	$12.99 \cdot 10^{-6}$	$3.048 \cdot 10^{-6}$	$1.004 \cdot 10^{-6}$

Table 5.2: Analytical results for static loading.  $\delta$  is the analytical deflection at the tip.  $\varepsilon$  is the analytical strain 0.4m from the clamped end.

The calculated strains were small in magnitude. Note that the calculations were conducted without weight from the motor. For practical reasons, the measurement of static deflections and strains were impossible to do without the exciter on the beam, as the assembly process would effect the measurements. In addition, the magnitudes are so small that the response can be assumed to be linear, making the difference due to the weights relevant.

## 5.1.2 Experimental results

The static deflection of the beam was measured as described in Section 3.5.1. The strains were measured as described in Section 3.6.1. The following results were obtained.

Weight [kg]	$\delta_1[m]$	$\Delta\delta_1[m]$	$\delta_2[m]$	$\Delta\delta_2[m]$
2.43	$27 \cdot 10^{-6}$	0	$18.33 \cdot 10^{-6}$	0
4.87	$53 \cdot 10^{-6}$	$26 \cdot 10^{-6}$	$35 \cdot 10^{-6}$	$16.67 \cdot 10^{-6}$
7.26	$77 \cdot 10^{-6}$	$24 \cdot 10^{-6}$	$52.67 \cdot 10^{-6}$	$17.67 \cdot 10^{-6}$

Table 5.3: Deflection 5.5 cm from tip.  $\delta_1$  is the deflection for weld configuration 1.  $\delta_2$  is the deflection for weld configuration 2.  $\Delta\delta_1$  and  $\Delta\delta_2$  are the changes in deflection.

Weight [kg]	$\varepsilon_1 [-]$	$\Delta\varepsilon_1[-]$	$\varepsilon_2 [-]$	$\Delta\varepsilon_2[-]$
2.43	$1.347 \cdot 10^{-6}$	0	$8.605 \cdot 10^{-7}$	0
4.87	$2.957 \cdot 10^{-6}$	$1.61 \cdot 10^{-6}$	$2.645 \cdot 10^{-6}$	$1.7845 \cdot 10^{-6}$
7.26	$3.958 \cdot 10^{-6}$	$1.001 \cdot 10^{-6}$	$4.092 \cdot 10^{-6}$	$1.447 \cdot 10^{-6}$

Table 5.4: Strain in top flange 0.4 m from clamped end.  $\varepsilon_1$  is the strain for weld configuration 1.  $\varepsilon_2$  is the strain for weld configuration 2.  $\Delta\varepsilon_1$  and  $\Delta\varepsilon_2$  are the changes in strain.

Table 5.3 and Table 5.4 show the average tip deflection and strains at the top flange for three different test. The tip deflection of the beam decreased when changing to weld configuration 2, which is the reasonable as the latter was a more firmly welded beam. The main source of error for this test are thought to be the position and angle

of the micrometer. In order to obtain accurate results from both weld configurations, the placement was marked during testing on weld configuration 1. However, given the small scale of the deflections, even small inaccuracies in the placement for weld configuration 2 could effect the results.

The strain measurements showed a relative increase in magnitude when going from weld configuration 1 to weld configuration 2. An uncertainty here could be from noise in the signal. The increase in deflection and reduction in strains when going from weld configuration 1 to weld configuration 2 indicates that rotation in the clamped end was more prominent for the first configuration. Consequently, the deflection for weld configuration 2 might have been dominated by beam bending. The same behaviour can be expected for the dynamic test, which might have lead to more relative movement in the beam plate interface for weld configuration 1.

### 5.1.3 Numerical results

The numerical static deflection were found as descried in Section 4.8.1. Horizontal strain measurements were done at node 18300 located 0.402932 m from the plate on the top flange. The tip deflection was measured at node 65787, located 55.86 mm from the beam tip at the bottom flange.

Weights [kg]	$\varepsilon[-]$	$\Delta\varepsilon$	$\delta[m]$	$\Delta\delta$
2.43	$1.150 \cdot 10^{-6}$	0	$15.15 \cdot 10^{-6}$	0
4.87	$2.305 \cdot 10^{-6}$	$1.155 \cdot 10^{-6}$	$30.37 \cdot 10^{-6}$	$15.22 \cdot 10^{-6}$
7.26	$3.436 \cdot 10^{-6}$	$1.131 \cdot 10^{-6}$	$45.28 \cdot 10^{-6}$	$14.91 \cdot 10^{-6}$

Table 5.5: Results, numerical static deflection for weld configuration 1

The first observation is that the numerical response of the beam was close to linear as the loads were applied.

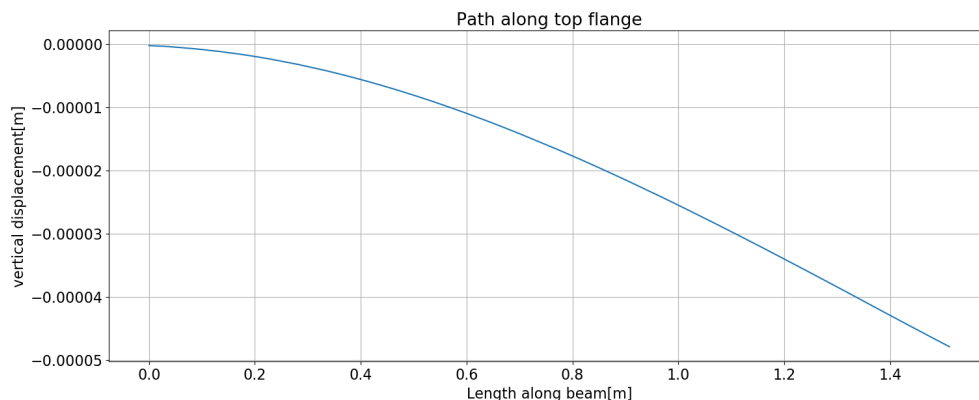


Figure 5.1: Displacement along beam with all weights

Figure 5.1 shows the vertical displacement at the top flange along the length of



---

the beam. The parabolic shape are thought to be a good representation of beam bending for a cantilever beam. It is also noted that the deflection is close to zero at the clamped end, meaning the *Tie* constraints seem to merge the parts together.

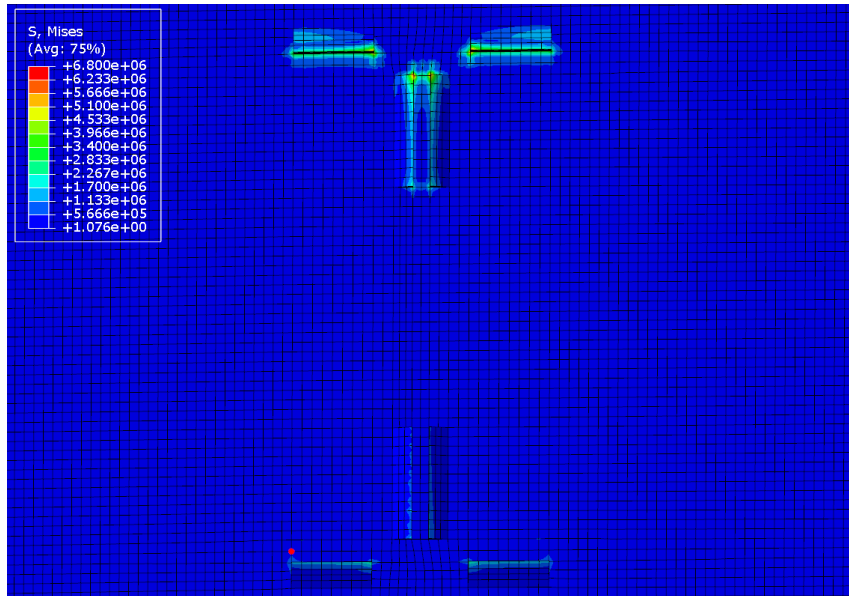


Figure 5.2: Stress in weld during static loading, weld configuration 1

The plate stress contours in Figure 5.2 show that the largest stress were at the welds in the top flange, indicating the beam was kept in place at the top by the constraint. In order to investigate the accuracy of the constraint behaviour, the displacement of *nodes 476* and *node 113889* were considered. These nodes are located on the beam and the weld and can be seen in the following figure.

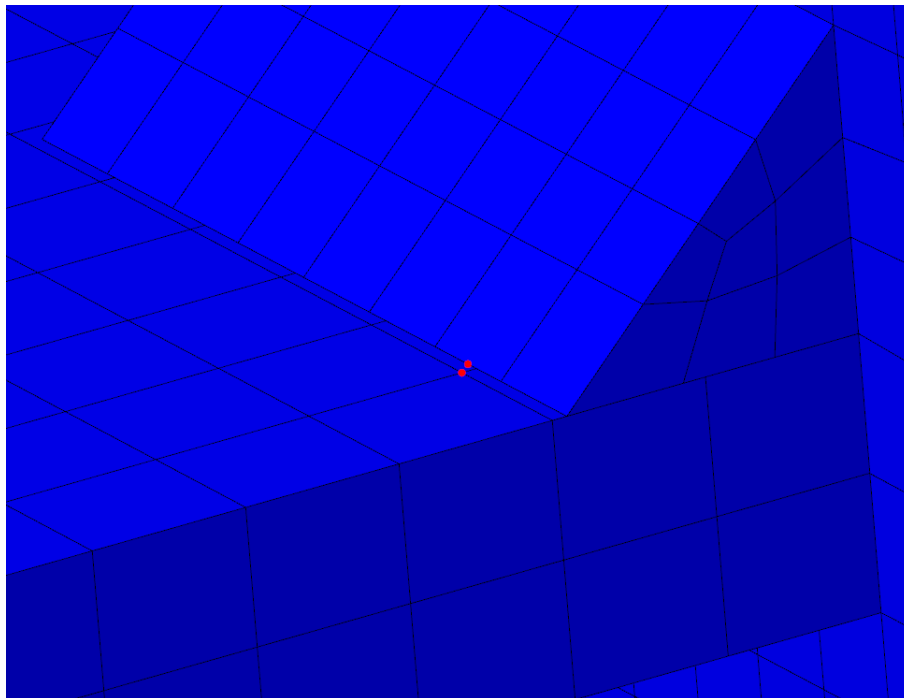


Figure 5.3: Weld at top flange

The measured horizontal displacements are given in the following table.

Node	Horizontal displacement[m]
476	$144.749 \cdot 10^{-9}$
113889	$140.84 \cdot 10^{-9}$
Difference [m]	$3.909 \cdot 10^{-9}$

Table 5.6: Horizontal displacement at weld

The weld displacement was slightly smaller than the beam displacement, as seen in Table 5.6. The reason for the difference could have been that node 476 was placed on a larger element, further away from the clamped end. However, a more likely reason is that *Tie* constraint has some deviation to it. As the difference were  $10^{-9}$ , the constraint can be seen as fairly accurate in modelling of a welded connection.

Another aspect in the interaction between the beam and the plate was the contact formulation. The contact openings at *node 11122* and *node 11049* are presented in the following table. The nodes were located in the middle of the top flange 76.39 mm from the web middle and located in the middle of the bottom flange 76.38 mm.

Node	Location	Opening[m]
11122	Top flange	$171.245 \cdot 10^{-9}$
11049	Bottom flange	$-19.1254 \cdot 10^{-12}$

Table 5.7: Contact opening at top flange and bottom flange

The penetration can be assessed by looking at the opening for the bottom flange. It is clear that there was some movement in the node, if this was from penetration or contraction in the metal is hard to conclude on. It is known that the contact formulation can have some penetration, making it plausible that this is the cause.

In order to get an overview of the static behaviour of the beam, results from all methods are gathered in the following figure.

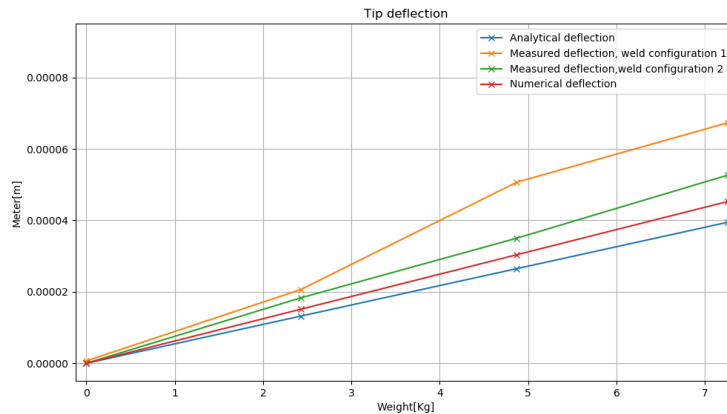


Figure 5.4: Static deflection, 5.5 cm from tip

---

The deflections were close to linear for all cases except for the experimental results for weld configuration 1. The reason for this deviation might have been some rotation at the clamped end. In addition, there was less deflection from the numerical result for weld configuration 1 than the experimental results for weld configuration 2. This might have been from the uncertainty in the material properties of the beam. As the experimental results had assumed material properties and possible imperfections in geometry, there is reason to believe that the consistent geometry and homogeneous material in the numerical beam could effect the results. Another possible error source was the rather coarse mesh in the numerical calculations, especially around the welds.

The static tests were conducted in order to verify the behaviour of the beam. This evaluation was intended as a supplement to the dynamic analyses and the meshes were therefore kept the same. In order to reduce computation the number of elements were kept as low as possible, leading to a coarse mesh. There is reason to believe that a finer mesh around the welds would have improved the accuracy of the static results. In addition, there was uncertainty in the analog experimental measurements. However, the procedure was repeated three times meaning that the results should be fairly accurate. The use of heavier weights might have improved the accuracy, as the effects of errors in material properties and geometrical properties would have been smaller compared to the measurements.

## 5.2 Damping during free vibration

During the free vibration test the natural frequency and the logarithmic damping were established. Results including analytical natural frequency, experimental natural frequency and experimental damping are presented and discussed in this section.

### 5.2.1 Analytical natural frequency

An estimate for the natural frequency for weld configuration one was found by combining the measured deflections with the 2-DOF system presented in Section 2.2.1. By using Equation 2.4 in the matrices presented in Section 2.2.1

Knowing the rotational stiffness of the system one can find the coupled natural frequency of the system as described in Section 2.2. The resulting average rotational stiffness is  $k_{\theta} = 1.7214095 \cdot 10^6$ .

This results in a natural frequency of 50.49 Hz. The main source of this deviation is thought to be the rotational stiffness,  $k_{\theta}$ . The measurements of static deflection are prone to some errors as previously mentioned. The small magnitude of deflection makes the rotational stiffness quite sensitive, thus leading to uncertainty in result.

For weld configuration 2, the end is assumed to be fully clamped. The eigenfrequency was therefore calculated using the matrices described in Section 2.2. The resulting

---

natural frequency was  $f_n = 36.84$  Hz. As the latter is the frequency for a stiffer system, the two results do not seem to give realistic values.

## 5.2.2 Experimental natural frequency and damping

The following time series were recorded during a hit of a hammer at the top flange for weld configuration 1. A Butterworth filter with cutoff 100 Hz. All the presented results are from the vertical acceleration sensor on the weld. This was chosen as the amplitude of the signal is larger further away from the web, which should have reduced the influence of noise in the signal.

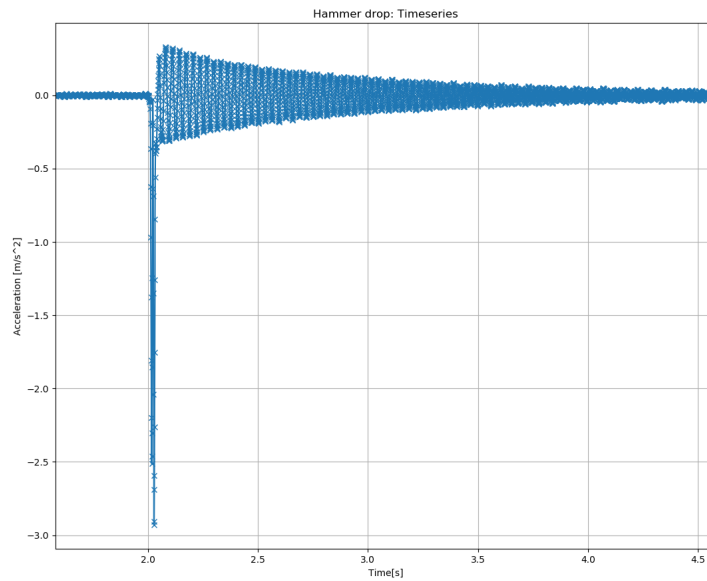


Figure 5.5: Time series of vertical acceleration

The hammer hit can clearly be seen as the large peak in acceleration right after  $t = 2$  s in Figure 5.5. By conducting a discrete Fourier analysis on the vertical vibration, it was also possible to identify the natural frequency of the system. The following figure show the transform for vertical acceleration.

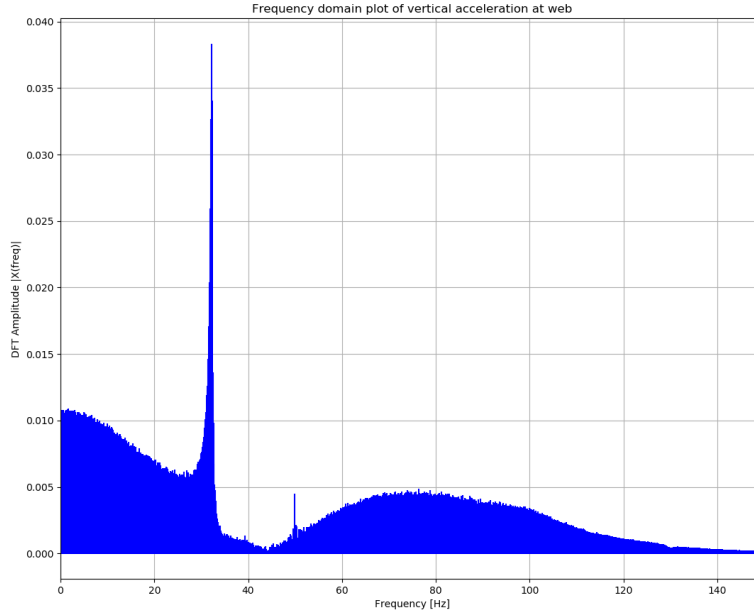


Figure 5.6: Frequency domain plot of acceleration

The natural frequency is found by identifying the peak of the transform. Three test were initially conducted in weld configuration 1, before running the forced vibration tests. Three additional free vibration tests were performed in between the forced vibration testing in order to observe possible changes in the natural frequency. All the measured natural frequencies are given below.

Test number	Vertical $f_n$ [Hz]
1	32.154
2	32.105
3	32.27
4	31.83
5	30.71
6	23.6

Table 5.8: Measured natural frequency, weld configuration 1

Even while considering the mentioned sources of error such as off center hit with the hammer and signal noise, it is observed that the measured natural frequency from the three first test are cohesive and subsequently regarded as valid. For the three tests conducted in between the forced vibration tests, a decline in the natural frequency was observed. The most likely source of this decline is thought to be cracking in some of the welds. Before the presented test were conducted, cracks were observed as mentioned in Section 3.7.2.

In order to calculate the damping of the system the peaks of the response had to be

identified. The following figure show the positive peaks that were identified during post-processing. These were later used in the damping analysis.

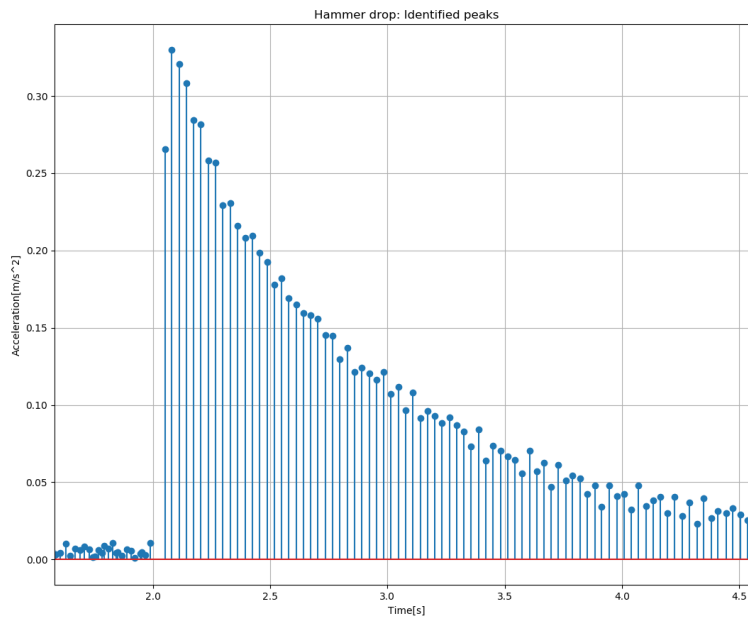
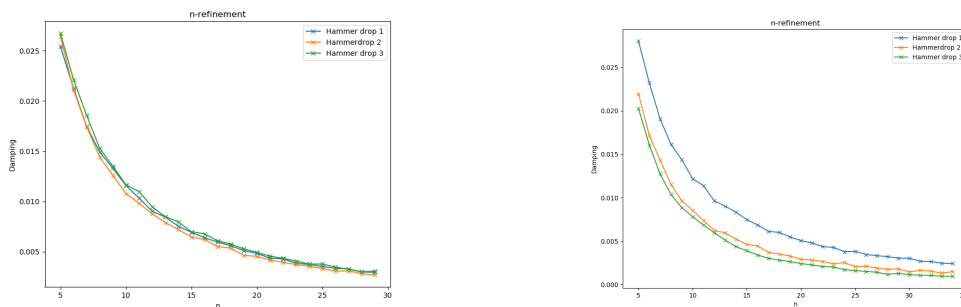


Figure 5.7: Identified peaks, test 1

As seen in Figure 5.7, the decay of the peaks followed a trend but there was some fluctuation between neighbouring peaks. This error could be from signal noise.

The damping levels found from the measured results were observed to be dependent on the counted number of peaks. The following figure show the results from two convergence studies where damping levels were compared to counted number of peaks.



(a) No suspected cracks

(b) Suspected cracks

Figure 5.8: Convergence, weld configuration 1

Figure 5.8a show the damping levels for test 1 – 3 in Table 5.8. It can be seen that the damping levels are close to each other and that there is convergence when the

number peaks  $n$  increases. Even though the results are from the hammer test with the given inaccuracies of procedure this compliance in the results may be interpreted as an confirmation of the accuracy of the logarithmic decrement as an measurement of damping. the results are diverging after the suspected cracking of welds. This can be seen in Figure 5.8b. The correlation in damping and natural frequency could be an indication of a relation between damping and stiffness of the system. The following table all results for the hammer test conducted for weld configuration 1. The maximum strains,  $\varepsilon_m$  are also included.

Test number	$f_n$ [Hz]	$n$	$\zeta$ [-]	$\varepsilon_m$ [-]
1	32.154	22	0.004285	$15.82 \cdot 10^{-6}$
2	32.105	16	0.006217	$17.88 \cdot 10^{-6}$
3	32.27	16	0.006781	$15.18 \cdot 10^{-6}$
4	31.83	18	0.006001	$10.82 \cdot 10^{-6}$
5	30.71	13	0.005943	$16.25 \cdot 10^{-6}$
6	23.6	23	0.002022	$16.95 \cdot 10^{-6}$

Table 5.9: Measured natural frequency and damping, weld configuration 1

Table 5.9 show the results from different hammer hits. The first test show lower damping than test 2 and test 3. The difference in peaks counted before convergence can reveal the possible source of this difference to be noise in the signal, again this can be from the small amplitudes of the response during the hammer hit. Same can be said about the results from test 6. The strains in the flange are also small for all test, making signal noise an important factor. The average damping before reduction in the natural frequency was  $\zeta = 0.005761$ . If the damping was dominated by material damping or friction is impossible to conclude with from this result only. However, the level is low compared to damping normally used in structures.

For weld configuration 2 the same test were conducted. The resulting acceleration plots, peaks plots and frequency domain plots were similar to those for weld configuration 1. All result plots can be seen in Appendix C.

Similarly to weld configuration 1, a convergence study was conducted for weld configuration 2.

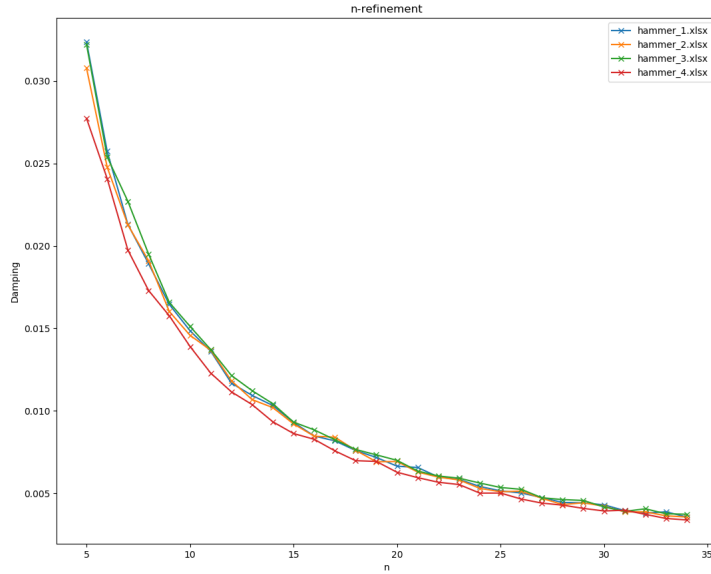


Figure 5.9: Convergence, weld configuration 2

As seen in Figure 5.9, the convergence were similar for all the conducted tests. The results are given in the following table.

Test number	$f_n$ [Hz]	$n$	$\zeta$ [-]	$\varepsilon_m$
1	37.76	17	0.008182	$9.76 \cdot 10^{-6}$
2	37.92	14	0.01020	$10.35 \cdot 10^{-6}$
3	37.72	19	0.00733	$10.86 \cdot 10^{-6}$
4	37.84	16	0.008277	$8.70 \cdot 10^{-6}$
5	36.02	16	0.008608	$9.945 \cdot 10^{-6}$
6	35.90	16	0.008924	$10.83 \cdot 10^{-6}$
7	35.53	16	0.0060107	$9.03 \cdot 10^{-6}$
8	34.98	17	0.008003	$8.92 \cdot 10^{-6}$

Table 5.10: Measured natural frequency and damping, weld configuration 2.  $f_n$  is the natural frequency.  $n$  is the number of peaks counted.  $\zeta$  is the damping ratio.  $\varepsilon_m$  is the maximum measured strain.

Compared to weld configuration 1, there was an increase in the measured damping increased when the end was more firmly welded. Again, there were some discrepancies in the result that did not seem to be directly linked to the natural frequency. The measured strains are also relatively small giving uncertainty from signal noise. The average damping ratio before reduction in the natural frequency was  $\zeta = 0.008497$ .

The increase in damping ratio between weld configuration 1 and weld configuration 2 could suggest that the movement at the beam and plate interface does not have substantial damping for this beam. When more welds were introduced, its reasonable



---

to assume less movement, which again means that the increase in damping for weld configuration 2 likely come from other sources. The main suspect here is an increase in material damping.

### 5.3 Damping during forced vibration

The results from test were the half-power point method was used are presented in the following section. Note that the presented figures are for only one test, plot from remaining test are given in Appendix C.

#### 5.3.1 Experimental results

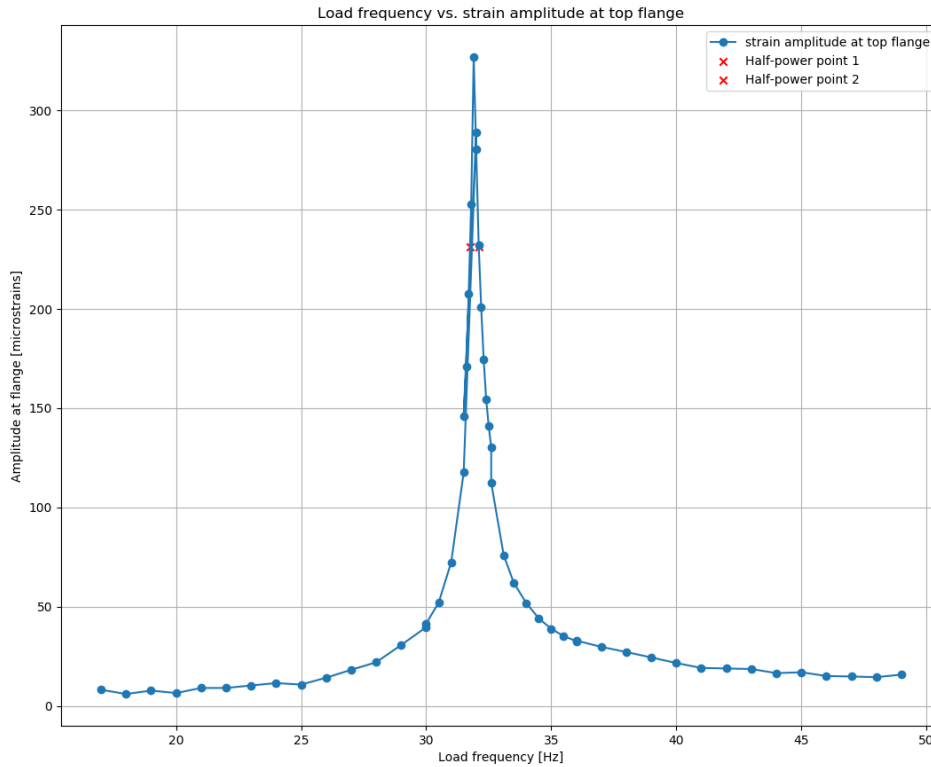


Figure 5.10: Vertical acceleration, max strain at 31.9 Hz

Figure 5.10 show the vertical acceleration at the web during forced vibration. A clear peak is observed near the resonance frequency. Note that the peak load frequency was not necessarily the resonance frequency. The peak of the response is subsequently named *frequency of max strain*. Even for a step length of 0.1 Hz, the response is increased substantially at peak compared to nearby frequencies. This lead

to interpolation between load frequencies being used in order to find the half-power point.

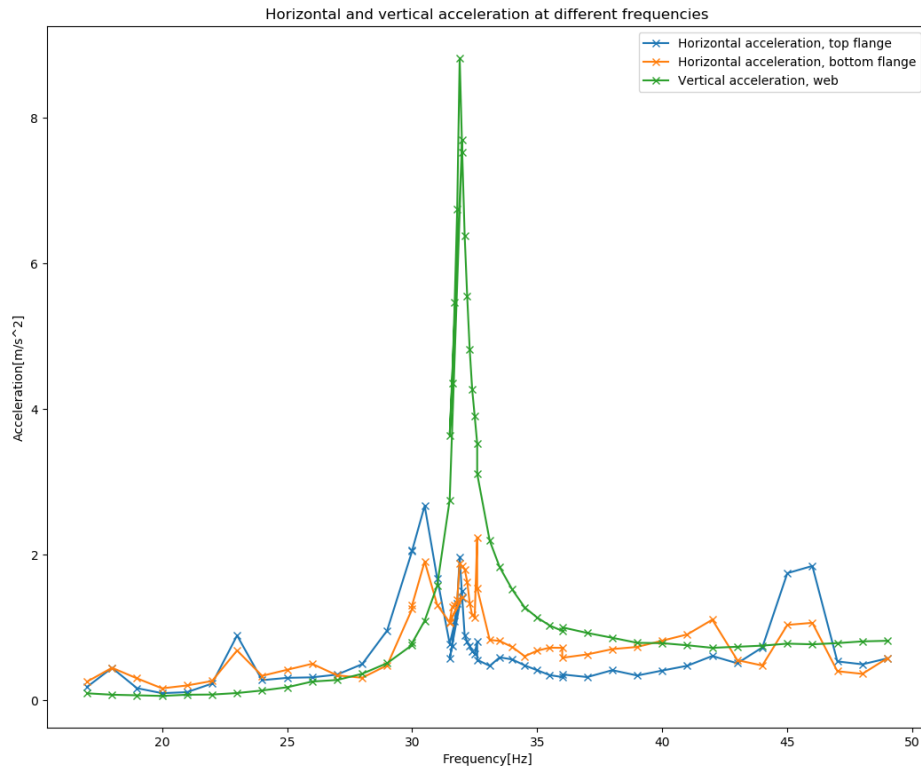


Figure 5.11: vertical -and horizontal acceleration, max strain at 31.9 Hz

Figure 5.11 show the vertical acceleration and horizontal acceleration of the top and bottom flange. The magnitude of the vertical acceleration was large compared to the horizontal for all load frequencies. The damping in the beam can therefore be assumed to be mainly from the vertical movement of the beam. However, it should be noted that the horizontal acceleration at the bottom flange seem to be somewhat larger than at the top flange for near resonance. The main suspects for this asymmetry are beam geometry, weld geometry or weld cracking.

The following table contain the numerical results for all the conducted damping test for weld configuration 1. These are presented in the same order as the test were conducted.

Frequency of maximum strain [Hz]	Strain gauge	Maximum strain, $\varepsilon_m$ [-]	$\zeta$ [-]	Damping from acceleration [-]
31.9	Top flange	$326.90 \cdot 10^{-6}$	0.00504	0.005593
	Bottom flange	$320.76 \cdot 10^{-6}$	0.005542	
30.2	Top flange	$268.25 \cdot 10^{-6}$	0.009756	0.008750
	Bottom flange	$262.88 \cdot 10^{-6}$	0.009815	
29.7	Top flange	$243.00 \cdot 10^{-6}$	0.007171	0.005943
	Bottom flange	$238.68 \cdot 10^{-6}$	0.007259	
27.9	Top flange	$180.71 \cdot 10^{-6}$	0.006743	0.005774
	Bottom flange	$182.95 \cdot 10^{-6}$	0.006702	
27.2	Top flange	$153.68 \cdot 10^{-6}$	0.009345	0.008039
	Bottom flange	$152.86 \cdot 10^{-6}$	0.009284	
24.6	Top flange	$91.64 \cdot 10^{-6}$	0.007097	0.007382
	Bottom flange	$91.07 \cdot 10^{-6}$	0.006638	
22.6	Top flange	$78.57 \cdot 10^{-6}$	0.011973	0.011444
	Bottom flange	$79.16 \cdot 10^{-6}$	0.011444	

Table 5.11: Results: Weld configuration 1

The damping levels were between values of 0.55% and 1.1%, where the overall average damping was  $\zeta = 0.007561$ . Another observation is the correlation in decreased strain,  $\varepsilon_{max}$  and decreased frequency of maximum strain. This observation corresponds to decrease observed in Section 5.2.2. Note that  $\varepsilon_{max}$  is given at the strain gauge 0.4 m from the clamped end. The measurements of vertical acceleration were used in the calculation of damping as the large magnitude of the signal reduced the influence from noise.

As seen in Table 5.11, the damping values for the test with maximum strain at 30.2 Hz has some deviation from nearby test.

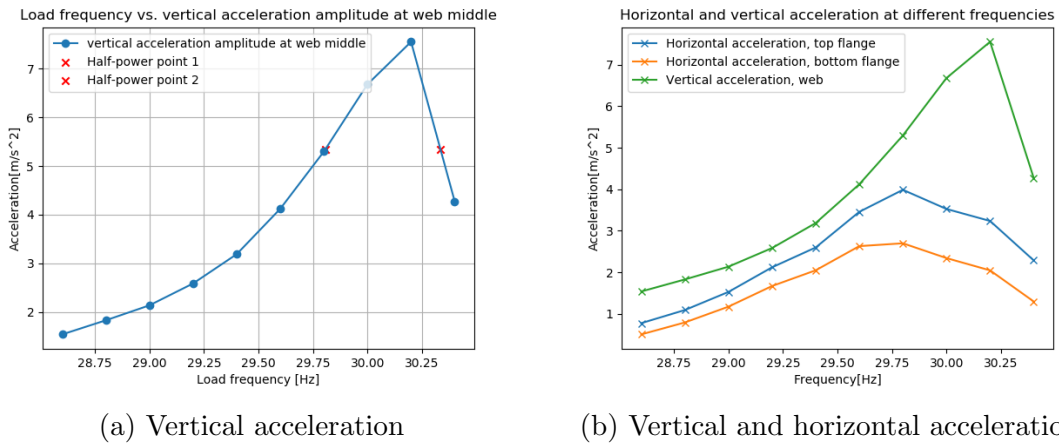


Figure 5.12: Maximum strain at 30.2 Hz

Figure 5.12a show that the response peak for the mentioned test. There were only

two measured point between the half-power points, introducing some uncertainty in the results. The horizontal accelerations were observed to be substantial when compared to the vertical for this test. This can be seen in Figure 5.12b. The large horizontal acceleration introduce some uncertainty in the damping result as the damping was calculated from the vertical acceleration. The measured damping could therefore be smaller than the real damping of the beam as torsional movement may increase the energy dissipation i.e damping, by increased movement of the beam.

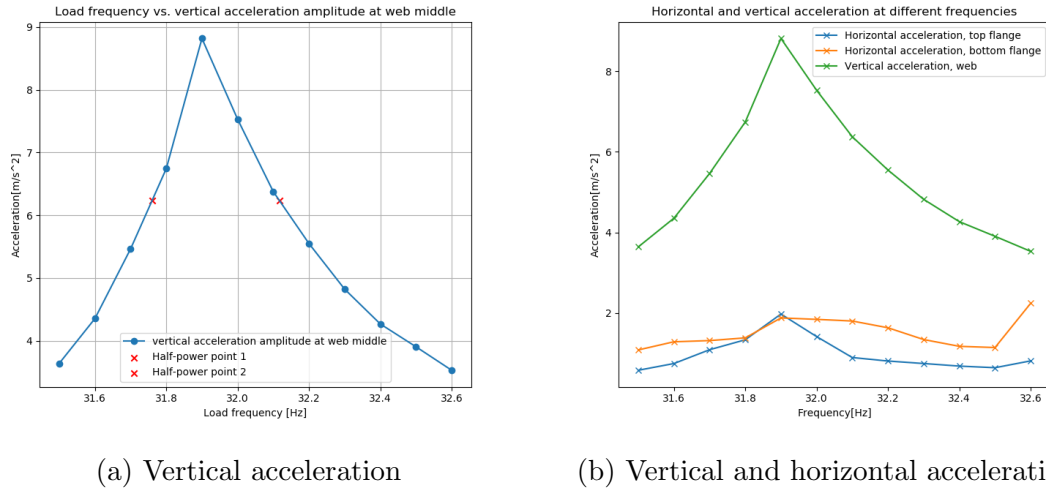


Figure 5.13: Maximum strain at 31.9 Hz

The results given Figure 5.13 show a more symmetric peak of the vertical response. In addition, the horizontal acceleration were relatively low, meaning the damping results are thought to be more accurate.

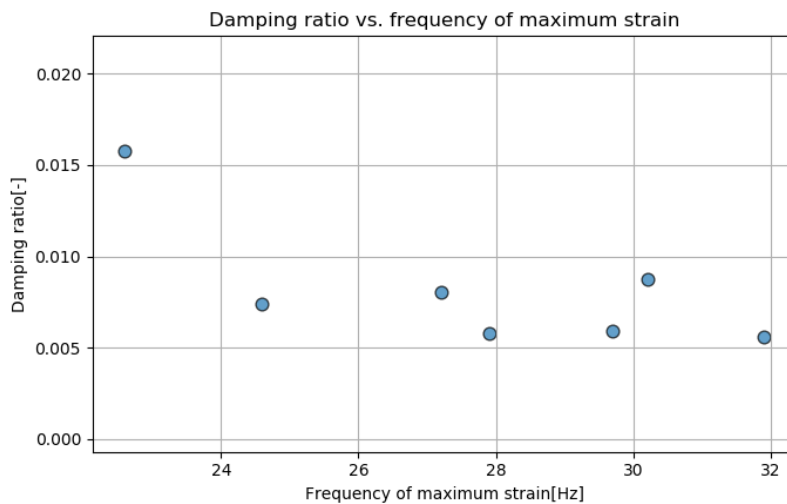


Figure 5.14: Damping rations for weld configuration 1

All damping ratios for weld configuration 1 are shown in Figure 5.14. The plot shows an increase in the damping as the load frequency of maximum strain was

---

reduces. For the lowest frequency the damping is drastically increased. The increase in damping for lower frequencies can come from an increase in the relative motion in the interface between the beam and plate. However, since there was no trend leading up to this damping level in other tests, there is no substantial evidence for this being the case.

For weld configuration 2 changes in beam behaviour were observed. First, during loading near and above resonance there was a slowly varying vibration of about 1 Hz. In addition, there was an increase in the maximum response compared to weld configuration 1. The slowly varying vibration disappeared at high load frequencies. This behaviour can be seen in the following figure.

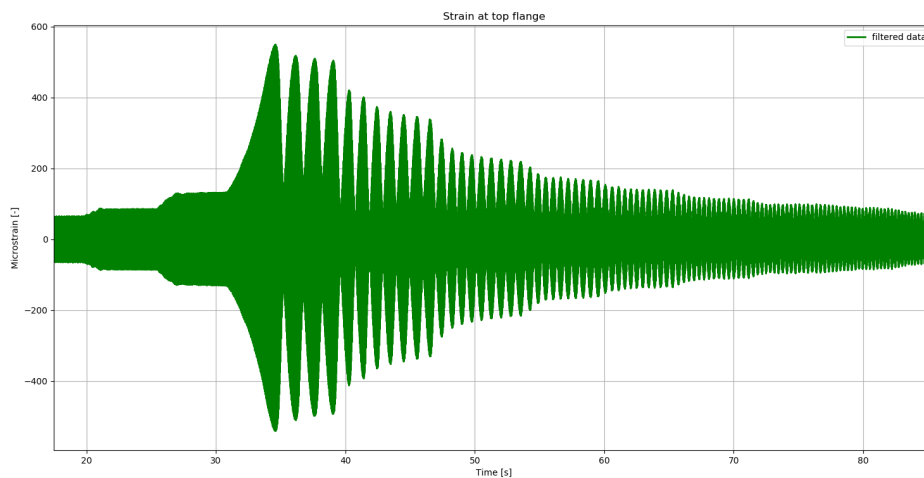


Figure 5.15: Time-series during forced vibration

The cause of this behaviour was most likely the weld as they were the only change when coming to weld configuration 2. As the old welds were not removed before elongating the welds, old cracks could be the source of this behaviour. The results were still regarded as useful since the calculation of the half-power point used the peak amplitude at each load frequency. On the contrary this behaviour should be kept in mind when considering the validity of the result for this configuration. Rotational movement could also introduce friction in beam to plate interface resulting in deviation from the numerical model.

When considering the response for different load frequencies the torsional movement was more prominent compared to the vertical response. This can be seen in the following figure.

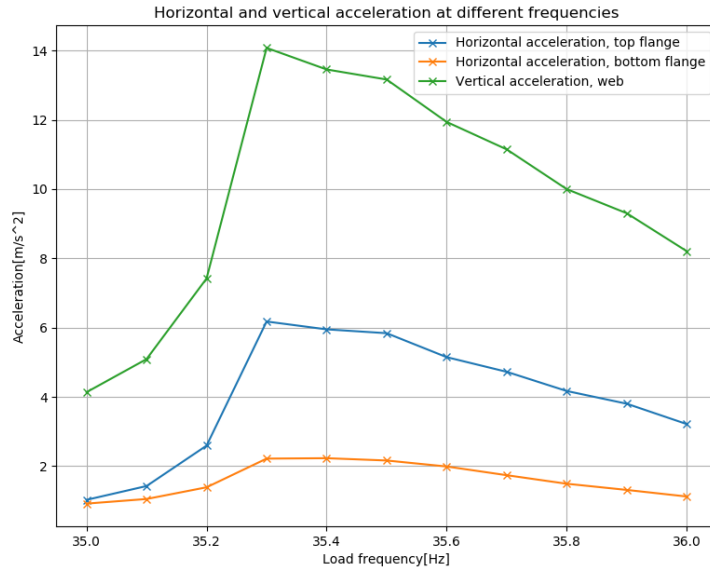


Figure 5.16: Horizontal and vertical acceleration

As seen in Figure 5.16 the horizontal acceleration is greater for this weld configuration. The shape of the response peak for the vertical movement was also changed with larger response past resonance. The same behaviour was observed for the strain, as seen in Figure 5.17.

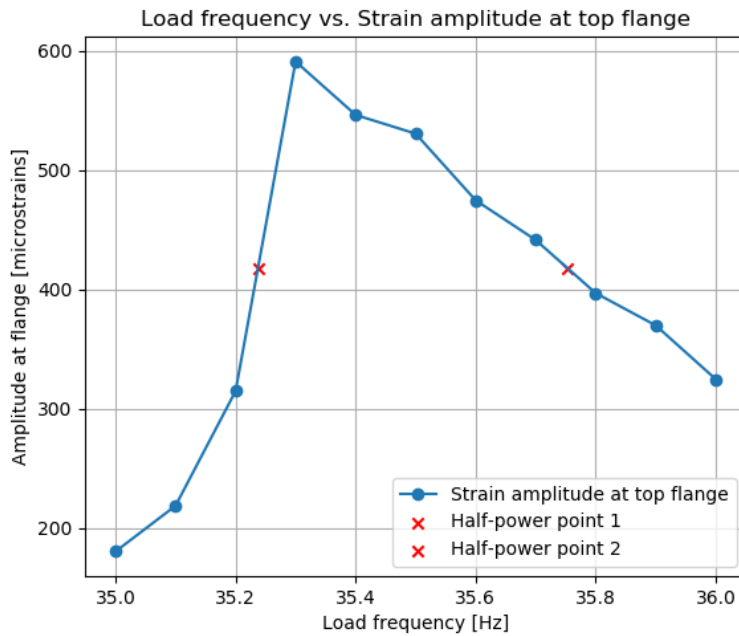


Figure 5.17: Strain at top flange

Furthermore, the results from different runs are presented in the following table.

Frequency of maximum strain [Hz]	Strain gauge	Maximum strain, $\varepsilon_m$ [-]	$\zeta$ [-]	Damping from acceleration [-]
36.5	Top flange	$510.99 \cdot 10^{-6}$	0.0088864	0.0091
	Bottom flange	$513.86 \cdot 10^{-6}$	0.0088865	
35.3	Top flange	$592.38 \cdot 10^{-6}$	0.007298	0.00805
	Bottom flange	$591.22 \cdot 10^{-6}$	0.007297	
34.6	Top flange	$584.02 \cdot 10^{-6}$	0.008492	0.009698
	Bottom flange	$595.21 \cdot 10^{-6}$	0.008492	
34.5	Top flange	$574.62 \cdot 10^{-6}$	0.007818	0.008420
	Bottom flange	$586.04 \cdot 10^{-6}$	0.009284	
34.2	Top flange	$570.83 \cdot 10^{-6}$	0.007675	0.008124
	Bottom flange	$560.62 \cdot 10^{-6}$	0.007664	
34.1	Top flange	$559.62 \cdot 10^{-6}$	0.007495	0.008268
	Bottom flange	$548.98 \cdot 10^{-6}$	0.007526	
33.8	Top flange	$536.95 \cdot 10^{-6}$	0.006494	0.006813
	Bottom flange	$527.01 \cdot 10^{-6}$	0.006489	
33.6	Top flange	$461.90 \cdot 10^{-6}$	0.007831	0.007820
	Bottom flange	$451.73 \cdot 10^{-6}$	0.0078406	
33.4	Top flange	$491.19 \cdot 10^{-6}$	0.003537	0.003597
	Bottom flange	$481.13 \cdot 10^{-6}$	0.003537	
32.9	Top flange	$490.86 \cdot 10^{-6}$	0.005542	0.005425
	Bottom flange	$480.58 \cdot 10^{-6}$	0.005562	

Table 5.12: Results weld configuration 2

As for weld configuration 1, the frequency of max strain decreases as more tests are conducted. There was also a decrease in the measured strain over the course of the tests. Cracks in the welds are again assumed to be the cause of this behaviour. The comparison between frequency and damping is shown in Figure 5.18. The average damping ratio for the three first tests was  $\zeta = 0.008949$ . The three first test are regarded as the most accurate as cracks in the welds were thought to be less prominent. Damping ratios in this figure are found from the vertical acceleration.

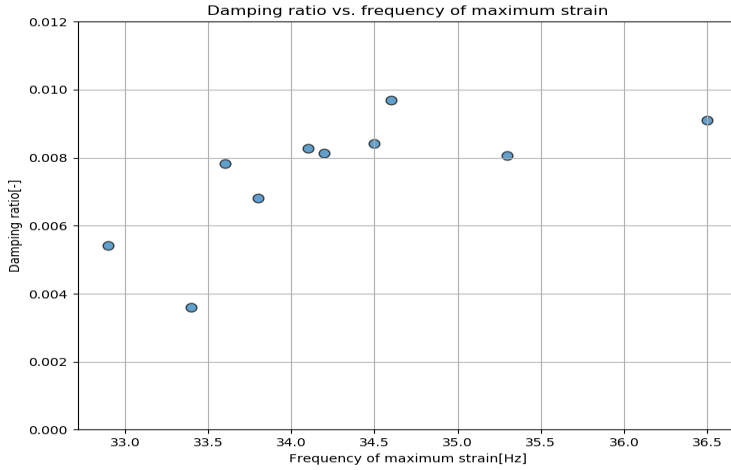


Figure 5.18: Frequency vs. damping

There was a slight increase in the observed damping ratios as the load frequency of maximum strain increased. This is opposite behaviour of weld configuration 1, where the damping increased as the frequency decreased. When considering the hypothesis of damping from movement of the beam and plate interface, the behaviour should be the opposite, i.e as the beam was welded more firmly the damping should have decreased.

On the contrary, this increase in damping when introducing more welds could be from the material damping in the metal. As mentioned in Section 2.3.4, there will be an increase in plastic strain damping in the material when the material is closer to yield. The local plastic strain can give large damping, and even though Lazan (1968) states that this form of damping is not as relevant structural material because of fatigue considerations, there is reason to believe that these high stresses were present during resonant runs in the experiment.

Comparing the experimental damping ratios from the free vibration and forced vibration one can see that for both types of tests the damping increased for weld configuration 2. During free vibration for weld configuration 1, the average damping was  $\zeta = 0.005761$  before substantial reduction in the frequency of maximum strain. The damping results from the three first tests of the half-power method had similar magnitude. Given that both tests show nearly the same damping, there is evidence to believe that the damping level was around 0.5% – 0.6%.

The same can be said about weld configuration 2, where the free vibration tests show  $\zeta = 0.008497$ . The first three tests for the half-power point method show values around  $\zeta = 0.009$ . A damping level between 0.8% – 0.9% for weld configuration 2 is therefore plausible. The damping levels can therefore be thought to increase as more welds are introduced. As a result of this there is no substantial evidence for an increase in damping due to more relative movement at the interface when the welds are intact. The only increase were found when the welds were cracked and there was substantial increase in the movement of the clamped end.



---

## 5.4 Assessment of repeatability

The repeatability of the preformed tests were seen as somewhat unsatisfactory. The resulting damping are inconsistent when repeating the test even though there are trends in some of the results as shown above. The change in natural frequency during testing also makes repeating the results difficult. The most consistent tests were the hammer tests, even with uncertainties in the method. The half-power point method showed changes in the behaviour during testing which were thought to be from cracks in the welds.

## 5.5 Numerical damping results

In the following section the numerical damping levels are established and compared to the experimental results. The numerical analysis was only conducted for weld configuration 1 as there was limited time after deciding not to move forward with the Lagrangian multipliers in the contact formulation.

### 5.5.1 Numerical eigenfrequency

The natural frequency of the beam is found as described in chapter 4. The resulting eigenfrequency was  $f_n = 42.08$  Hz for weld configuration 1, where the shape of the bending mode can be seen in the following figure.

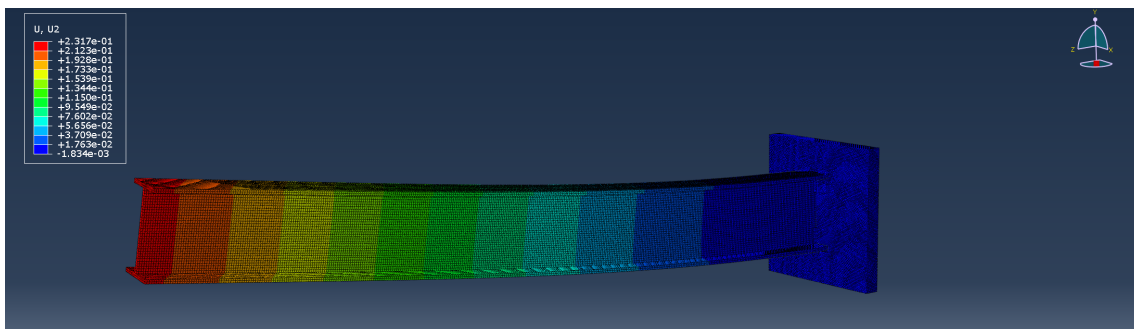


Figure 5.19: Natural frequency in bending mode

This numerical eigenfrequency was somewhat higher than the experimental results which were around 32 Hz during initial testing. However, as seen from the static deflection in Figure 5.4, the behaviour of the beam was stiffer in the numerical analysis. This might explain the increase in the increase in natural frequency, however this reasoning is not consistent with the analytical static results which in turn were stiffer than the numerical. There is therefore some uncertainty in the numerical eigenfrequency.

---

## 5.5.2 Numerical free vibration for weld configuration 1

The time series and identified peaks for the numerical free vibration are shown in the following figure.

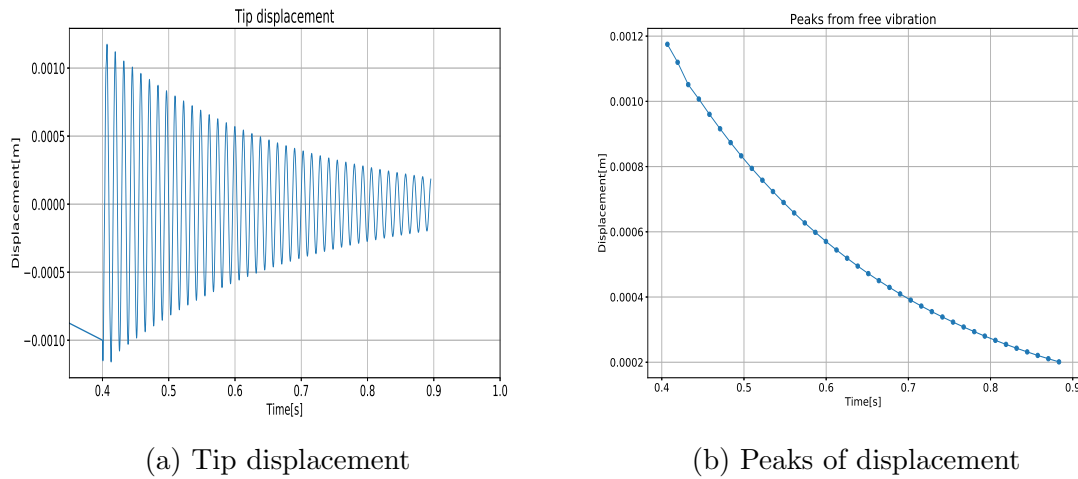


Figure 5.20: Transition between static and implicit dynamic analysis

In Figure 5.20 we can see that there was some damping in the system as the peaks of the response were reduced during the vibration. When the analysis transitions from static to implicit dynamic at 0.4 s, an increase in the response is observed. This behaviour can be seen in the following figure.

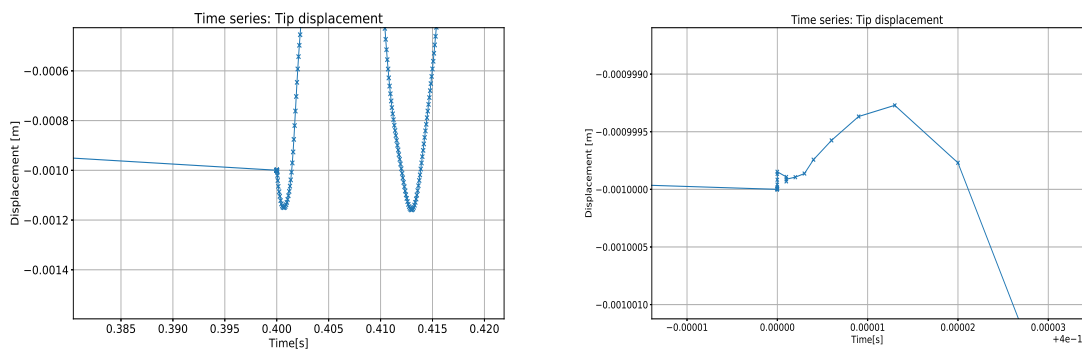
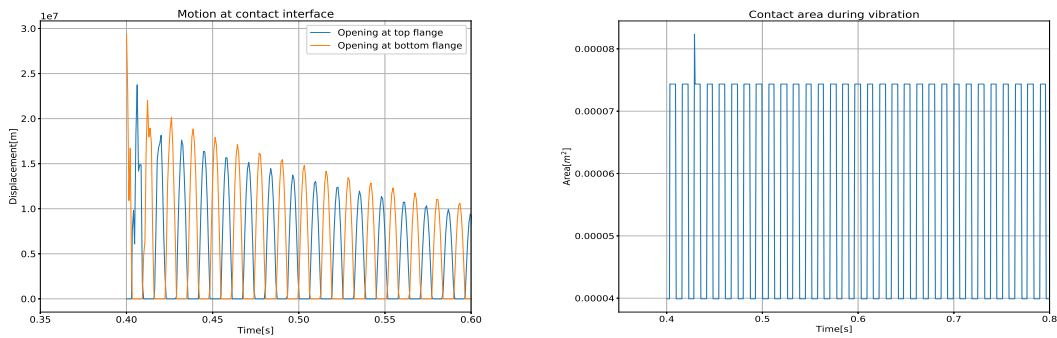


Figure 5.21: Transition between static and implicit dynamic analysis

The reason for this increase are unknown, and without experimental tests with the same method for inducing vibration it can not be concluded if this behaviour is natural or not.

The damping numerical damping ratio was identified as  $\zeta = 0.005666$  and it converged after counting 25 peaks. This results is quite similar to the one obtained by the experimental free vibration test which was at  $\zeta = 0.005761$  for weld configuration 1. As there was no material damping or numerical damping this suggests

that all damping during the free vibration test was a results of movement of the interface. The following figure shows the movement of the opening at the top and bottom flanges, in addition to the total contact are.



(a) Opening at top flange an bottom flange

(b) Contact area at interface

Figure 5.22: Opening and contact area

As seen in Figure 5.22a the contact opening decays as during the vibration. Note that the bottom opening had a peak at the start of the free vibration, which are though to correspond to peak in Figure 5.20a. The bottom opening was a somewhat larger than the top opening which could be a result of the mesh not being perfectly symmetrical around the node. However, the movement are regarded as fairly accurate as there was very small penetration of the surface. Looking at total contact area in Figure 5.22b

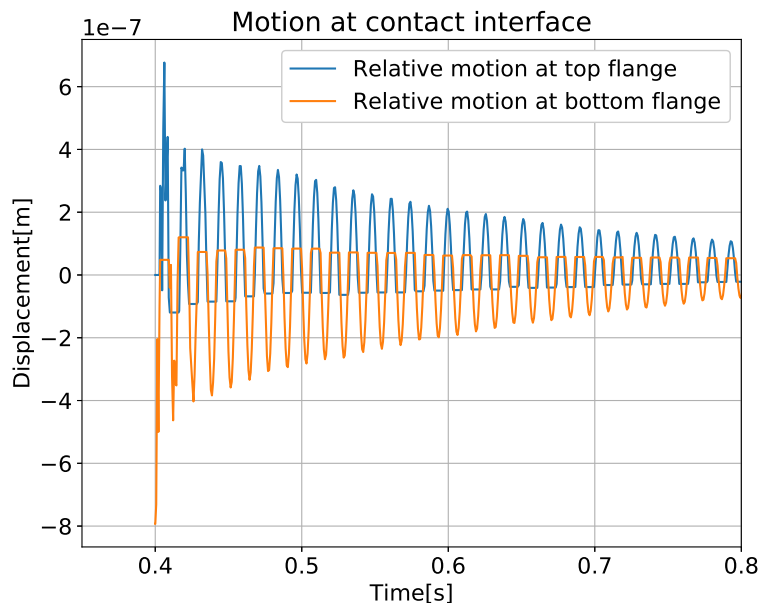


Figure 5.23: Vertical motion of top and bottom

First, looking at the tangential vertical motion of nodes at the top flange middle and bottom flange middle, there was large motion initially before a gradual decay. The

top and bottom were also in opposite phases during vibration. It is also noted that the motion is constant at some point during each oscillation. The reason for this is thought to be the horizontal stopping the vertical movement of the beam end.

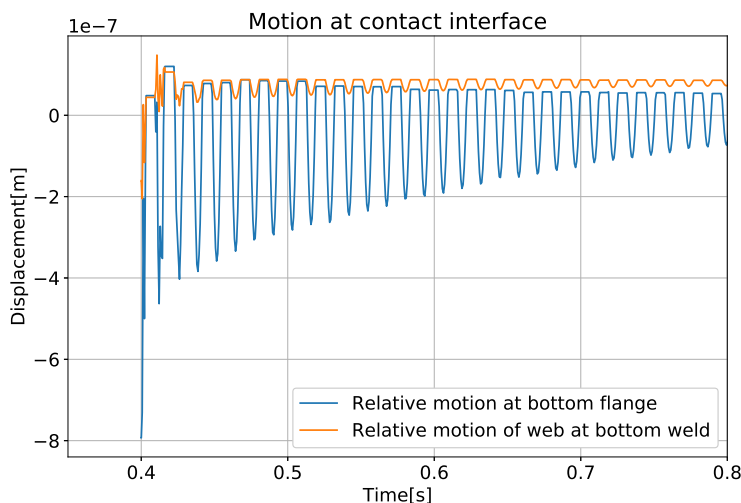


Figure 5.24: Vertical motion of bottom flange and web at bottom weld

As seen in Figure 5.24, the vertical motion of the web is small compared to the motion of flange meaning that the *Tie* constraints held the web in place fairly well.

The results found above indicate that almost all damping found from the experimental free vibration test come from the steel on steel contact in the clamped end. From the forced vibration test the average damping were also around the same level for the weld configuration. On the contrary, by looking at the results from the static test its suggested that the numerical model behaves more firmly than the experimental. One can therefore assume that there would be more damping if material damping was introduced. This would require more testing with both full weld and a parametric study of the material damping.

### 5.5.3 Accuracy of FE analyses

The uncertainty in the finite element model comes from different choices that were made regarding methods and parameters. First, the geometry of the model has some simplifications. The flanges were modelled with constant thickness in order to ease the meshing. However, the largest geometrical uncertainty is seen to be the weld shapes. As the real welds were uneven in both a-measurement and length, an average size of the physical welds were used for respectively the web and flange welds. As previously discussed, there is also the possibility of the numerical results deviating from the experimental as imperfections in the physical beam are likely.

There was also some uncertainty in the sensitivity of the time step. Figure 5.25 show a comparison of the measured peaks for both  $\Delta t = 0.00075$  s and time step

---

$\Delta t = 0.000075$  s. The first time step was selected as it was close to the sample rate of the experimental test.

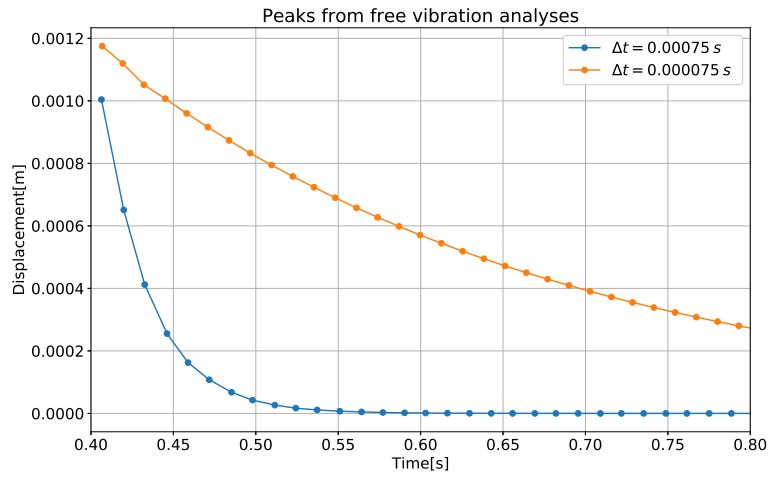


Figure 5.25: Measured peaks for different time steps

The response was clearly effected by the the reduction in time step, which a larger decay observed for the longer step. Unfortunately there was neither time or available computational power to reduce the time step further. For reference, the computation of 0.5 s of free vibration using time step  $\Delta t = 0.000075$  s took 118 hours and produced and 202.9 GB output file. It was seen as impractical to use smaller time steps without access to a more powerful computer. This makes the given damping level  $\zeta = 0.00576$  uncertain for the given results.

# Chapter 6

## Conclusion and further work

### 6.1 Conclusion

This main objective of this work was to investigate structural damping in welded structures and possible numerical models for calculation of damping levels. After reviewing relevant literature it is clear that there is a knowledge gap between the internal material damping and damping of full scale structures. The micromechanisms and mathematical qualifications of the internal damping of structural materials are seen as well established. The mathematical models for evaluating the response of full scale structure are also adequate. Here, modal analysis is widely used and consistent with field data. It is clear that assuming damping ratios are the only ways of establishing the damping matrix needed to perform these analyses. Unfortunately, the damping has previously been shown to be impossible to predict within plus minus 30 %

Full scale experiments were conducted on a weld cantilever I-beam in order to establish its damping levels. Tests were performed for different support conditions in terms of a partly welded clamped end and a clamped end with welds all around the cross section. The partly welded beam was later modelled in Abaqus CAE with the goal of separating the material damping from other sources of energy dissipation. The finite element model was made so that the beam and plate were connected through welds, creating steel on steel contact between the beam end and the plate. Augmented Lagrange contact formulation was used for the interface between the beam and the plate.

First, the result analytical results, experimental results and numerical results from a static deflection test were gathered. The results were fairly consistent, with the largest deflection found in the experimental result. The numerical model displayed stiffer behaviour than the real beam for similar weld geometry. This find was most likely related to meshing or geometrical imperfections as the constraints and contact formulation seemed to be accurate.

Damping levels were established during free vibration and forced vibration by utilizing the logarithmic decrement and half-power point method. The experimental

---

results indicated an increase in the damping ratio when going from a partly welded clamped end to a fully welded clamped end. Rough estimates for the respective weld configurations were 0.5% – 0.6% and 0.8% – 0.9%. The source of this increase could be more material damping in the beam as the fully welded configurations had higher stress levels during testing. The accuracy of the free vibration results were seen as the most consistent. However, possible errors due to signal noise and inaccuracies in experimental method, one can only use the mentioned damping levels as estimates.

The numerical damping result during free vibration was consistent with the observed experimental free vibration damping result. As the numerical model did not contain any material damping this could indicate that all the damping in that configuration was from friction. However, as the model contained uncertainties from meshing, geometry and time step size this hypothesis should only be seen as plausible. Thus, the overall evaluation of the model is that it can be useful as a simplification and be useful as the starting point for further work.

## 6.2 Recommendations for further work

The work done in this project can be useful as a start for numerical modelling of structural damping in welded structures. The following is recommended topic for further work.

First, possible further work for the analytical and experimental methods:

- Perform analytical calculations of material damping in order to obtain more insight in its importance in structural damping.
- Conduct experiments with more consistent beam and weld geometry. Special attention to cracking of weld could also be useful.
- Improve the methods for inducing free vibration, e.g. by having a more consequent hammer drop. Investigation of other methods for measuring damping could also be useful.

The following are recommendations for work on the FE model:

- Further investigate the use of Lagrangian multiplier methods as contact formulation.
- Investigate the use of explicit analysis.
- Further investigation of the uncertainty related to time step size in implicit analysis
- Conduct a parametric study of material damping in the numerical model.

# Bibliography

- Abdul Kudus, Sakhiah (May 2020). ‘Modal Analysis of Corrugated Plate by Finite Element Analysis’. In: *International Journal of Integrated Engineering* 12.4, pp. 252–258. URL: <https://publisher.uthm.edu.my/ojs/index.php/ijie/article/view/5413>.
- Caughey, T. K. (June 1960). ‘Classical Normal Modes in Damped Linear Dynamic Systems’. In: *Journal of Applied Mechanics* 27.2, pp. 269–271. ISSN: 0021-8936. DOI: 10.1115/1.3643949. URL: <https://doi.org/10.1115/1.3643949>.
- Caughey, T. K. and M. E. J. O’Kelly (Sept. 1965). ‘Classical Normal Modes in Damped Linear Dynamic Systems’. In: *Journal of Applied Mechanics* 32.3, pp. 583–588. ISSN: 0021-8936. DOI: 10.1115/1.3627262. URL: <https://doi.org/10.1115/1.3627262>.
- Chopra, Anil K. and Frank McKenna (2016). ‘Modeling viscous damping in nonlinear response history analysis of buildings for earthquake excitation’. In: *Earthquake Engineering & Structural Dynamics* 45.2, pp. 193–211. DOI: <https://doi.org/10.1002/eqe.2622>.
- Cuevas-Arteaga, C. et al. (Jan. 2012). ‘Comparison of Corrosion Resistance of Carbon Steel and Some Stainless Steels Exposed to LiBr-H<sub>2</sub>O Solution at low Temperatures’. In: *International journal of electrochemical science* 7, pp. 445–470.
- Dwairi, Hazim (June 2004). ‘Investigation of the Equivalent Viscous Damping Approach’. In.
- Ehnes, Charles W. (June 2003). ‘Damping in stiffener welded structures’. MA thesis. Naval Postgraduate School, Monterey, California.
- Grigoriev, I.S. et al. (1997). *Handbook of Physical Quantities*. CRC-Press. ISBN: 9780849328619.
- Hall, John F. (2006). ‘Problems encountered from the use (or misuse) of Rayleigh damping’. In: *Earthquake Engineering & Structural Dynamics* 35.5, pp. 525–545. DOI: <https://doi.org/10.1002/eqe.541>. URL: <https://onlinelibrary.wiley.com/doi/abs/10.1002/eqe.541>.



- 
- Hilber, Hans M., Thomas J. R. Hughes and Robert L. Taylor (1977). ‘Improved numerical dissipation for time integration algorithms in structural dynamics’. In: *Earthquake Engineering & Structural Dynamics* 5.3, pp. 283–292. DOI: <https://doi.org/10.1002/eqe.4290050306>. URL: <https://onlinelibrary.wiley.com/doi/abs/10.1002/eqe.4290050306>.
- Horn, J., J. Amdahl and S. Haver (2015). ‘Dynamic Amplification of Drag Dominated Structures in Irregular Seas’. In: URL: <https://ntnuopen.ntnu.no/ntnu-xmlui/handle/11250/2388655>.
- Huněk, I. (1993). ‘On a penalty formulation for contact-impact problems’. In: *Computers & Structures* 48.2, pp. 193–203. ISSN: 0045-7949. DOI: [https://doi.org/10.1016/0045-7949\(93\)90412-7](https://doi.org/10.1016/0045-7949(93)90412-7).
- Jacobsen, L.S. (1930). *Steady Forced Vibration as Influenced by Damping: An Approximate Solution of the Steady Forced Vibration of a System of One Degree of Freedom Under the Influence of Various Types of Damping*. Transactions of the American Society of Mechanical Engineers. ASME, pp. 169–181.
- Jiang, Lei and Robert J. Rogers (1988). ‘Combined Lagrangian multiplier and penalty function finite element technique for elastic impact analysis’. In: *Computers & Structures* 30.6, pp. 1219–1229. ISSN: 0045-7949. DOI: [https://doi.org/10.1016/0045-7949\(88\)90187-3](https://doi.org/10.1016/0045-7949(88)90187-3).
- Kareem, A. and K. Gurley (1996). ‘Damping in structures: its evaluation and treatment of uncertainty’. In: *Journal of Wind Engineering and Industrial Aerodynamics* 59.2. Meeting on Structural Damping International Wind Engineering Forum and Additional Papers, pp. 131–157. ISSN: 0167-6105. DOI: [https://doi.org/10.1016/0167-6105\(96\)00004-9](https://doi.org/10.1016/0167-6105(96)00004-9). URL: <https://www.sciencedirect.com/science/article/pii/0167610596000049>.
- Kvåle, Knut Andreas, Ole Øiseth and Anders Rønquist (Oct. 2017). ‘Operational modal analysis of an end-supported pontoon bridge’. In: *Engineering Structures* 148, pp. 410–423. DOI: [10.1016/j.engstruct.2017.06.069](https://doi.org/10.1016/j.engstruct.2017.06.069).
- Langen, Ivar and Ragnar Sigbjörnsson (1979). *EXCERPT FROM DYNAMISK ANALYSE AV KONSTRUKSJONER*. Tapir.
- (1980). ‘On stochastic dynamics of floating bridges’. In: *Engineering Structures* 2.4, pp. 209–216. ISSN: 0141-0296. DOI: [https://doi.org/10.1016/0141-0296\(80\)90002-4](https://doi.org/10.1016/0141-0296(80)90002-4). URL: <https://www.sciencedirect.com/science/article/pii/0141029680900024>.
- Lanzi, Armando and J. Enrique Luco (2017). ‘Caughey Damping Series in Terms of Products of the Flexibility Matrix’. In: *Journal of Engineering Mechanics* 143.9, p. 04017089. DOI: [10.1061/\(ASCE\)EM.1943-7889.0001306](https://doi.org/10.1061/(ASCE)EM.1943-7889.0001306).
- Lazan, B.j (1968). *Damping of materials and Members in Structural Mechanics*. Pergamon Press.
-

- 
- Liao, Yabin and Valana Wells (2011). ‘Modal parameter identification using the log decrement method and band-pass filters’. In: *Journal of Sound and Vibration* 330.21, pp. 5014–5023. ISSN: 0022-460X. DOI: <https://doi.org/10.1016/j.jsv.2011.05.017>.
- Liu, Man and D.G. Gorman (1995). ‘Formulation of Rayleigh damping and its extensions’. In: *Computers & Structures* 57.2, pp. 277–285. ISSN: 0045-7949. DOI: [https://doi.org/10.1016/0045-7949\(94\)00611-6](https://doi.org/10.1016/0045-7949(94)00611-6). URL: <https://www.sciencedirect.com/science/article/pii/0045794994006116>.
- Mallhotra, Anil K. and Joseph Penzien (1970). ‘Nondeterministic Analysis of Off-shore Structures’. In: *Journal of the Engineering Mechanics Division* 96.6. URL: <https://doi.org/10.1061/JMCEA3.0001331>.
- MIT (2022). *Contact constraint enforcement methods in Abaqus/Standard*. URL: <https://abaqus-docs.mit.edu/2017/English/SIMACAEITNRefMap/simaitn-c-contactconstraints.htm#simaitn-c-contactconstraints-auglagrange> (visited on 26th May 2022).
- (2021a). *Contact formulations in Abaqus/Standard*. URL: <https://abaqus-docs.mit.edu/2017/English/SIMACAEMATRefMap/simamat-c-dampingopt.htm> (visited on 28th May 2021).
- (2021b). *MIT-ABAQUS Documentation, About dynamic analysis procedures*. URL: <https://abaqus-docs.mit.edu/2017/English/SIMACAEANLRefMap/simaanl-c-dynamicproc.htm> (visited on 27th Nov. 2021).
- (2021c). *MIT-ABAQUS Documentation, Solid(continuum) elements*. URL: <https://abaqus-docs.mit.edu/2017/English/SIMACAEELMRefMap/simaelm-c-beamelem.htm#simaelm-c-beamelem-t-TimoshenkoShearFlexibleBeams-sma-topic4> (visited on 21st Oct. 2021).
- (2021d). *MIT-ABAQUS Documentation, Understanding constraints*. URL: <https://abaqus-docs.mit.edu/2017/English/SIMACAECAERefMap/simacae-c-itnconstraint.htm> (visited on 6th Dec. 2021).
- Mobron, Emiel et al. (2021). ‘Design of Havfarm 1’. In: pp. 99–111.
- Morison, J.R., J.W. Johnson and S.A. Schaaf (May 1950). ‘The Force Exerted by Surface Waves on Piles’. In: *Journal of Petroleum Technology* 2.05, pp. 149–154. ISSN: 0149-2136. DOI: 10.2118/950149-G. eprint: <https://onepetro.org/JPT/article-pdf/2/05/149/2238818/spe-950149-g.pdf>. URL: <https://doi.org/10.2118/950149-G>.
- Olmos, Bertha A. and Jose M. Roesset (2010). ‘Evaluation of the half-power bandwidth method to estimate damping in systems without real modes’. In: *Earthquake Engineering & Structural Dynamics* 39.14, pp. 1671–1686. DOI: <https://doi.org/10.1002/eqe.1010>.
-

- 
- Orban, F (Jan. 2011). ‘Damping of materials and members in structures’. In: 268. DOI: 10.1088/1742-6596/268/1/012022. URL: <https://doi.org/10.1088/1742-6596/268/1/012022>.
- Papagiannopoulos, George A. and George D. Hatzigeorgiou (2011). ‘On the use of the half-power bandwidth method to estimate damping in building structures’. In: *Soil Dynamics and Earthquake Engineering* 31.7, pp. 1075–1079. ISSN: 0267-7261. DOI: <https://doi.org/10.1016/j.soildyn.2011.02.007>.
- Qin, Q. and L. Lou (2000). ‘EFFECTS OF NON PROPORTIONAL DAMPING ON THE SEISMIC RESPONSES OF SUSPENSION BRIDGES’. In.
- Rayleigh, J.W.S.B. and R.B. Lindsay (1945). *The Theory of Sound*. Dover Books on Physics Series v. 1. Dover Publications. ISBN: 9780486602929.
- Satake, Naoki et al. (2003). ‘Damping Evaluation Using Full-Scale Data of Buildings in Japan’. In: *JOURNAL OF STRUCTURAL ENGINEERING. ASCE / APRIL 2003*, pp. 470–477. DOI: 10.1061/(ASCE)0733-9445(2003)129:4(470). URL: <https://ascelibrary.org/doi/abs/10.1061/%5C%28ASCE%5C%290733-9445%5C%2003%5C%29129%5C%3A4%5C%28470%5C%29>.
- Suda, Kenichi et al. (1996). ‘Damping properties of buildings in Japan’. In: *Journal of Wind Engineering and Industrial Aerodynamics* 59.2, pp. 383–392. ISSN: 0167-6105. DOI: [https://doi.org/10.1016/0167-6105\(96\)00018-9](https://doi.org/10.1016/0167-6105(96)00018-9). URL: <https://www.sciencedirect.com/science/article/pii/0167610596000189>.
- Tweten, Dennis J., Zach Ballard and Brian P. Mann (2014). ‘Minimizing error in the logarithmic decrement method through uncertainty propagation’. In: *Journal of Sound and Vibration* 333.13, pp. 2804–2811. ISSN: 0022-460X. DOI: <https://doi.org/10.1016/j.jsv.2014.02.024>.
- Viuff, Thomas, Bernt Leira et al. (Jan. 2016). ‘Dynamic Response of a Floating Bridge Structure’. In: pp. 181–189. DOI: 10.2749/stockholm.2016.0181.
- Viuff, Thomas, Xu Xiang et al. (June 2018). ‘Code-to-Code Verification of End-Anchored Floating Bridge Global Analysis’. In: V11AT12A031. DOI: 10.1115/OMAE2018-77902.
- Wilson, E. L. and J. Penzien (1972). ‘Evaluation of orthogonal damping matrices’. In: *International Journal for Numerical Methods in Engineering* 4.1, pp. 5–10. DOI: <https://doi.org/10.1002/nme.1620040103>. URL: <https://onlinelibrary.wiley.com/doi/abs/10.1002/nme.1620040103>.
- Wriggers, P. (1995). ‘Finite Element Algorithms for Contact Problems’. In: DOI: <https://doi.org/10.1007/BF02736195>.

---

Yucel, Adil and Alaeddin Arpacı (Sept. 2013). 'Free and forced vibration analyses of ship structures using the finite element method'. In: *Journal of Marine Science and Technology* 18. DOI: 10.1007/s00773-012-0210-1.

---

# Appendix

## A Theory

### Mass and stiffness matrix for beam model

$$\mathbf{K} = \frac{2EI}{l^3} \begin{bmatrix} 6 & -3l & -6 & -3l \\ -3l & 2l^2 & 3l & l^2 \\ -6 & -6l & 6 & 3l \\ -3l & l^2 & 3l & 2l^2 \end{bmatrix}$$

$$\mathbf{K} = \frac{ml}{420} \begin{bmatrix} 156 & -22l & 54 & 13l \\ -22l & 4l^2 & -13l & -3l^2 \\ 54 & -13l & 156 & 22l \\ 13l & -3l^2 & 22l & 4l^2 \end{bmatrix}$$

### Consistent mass matrix

$$\begin{aligned} m_v &= \rho A \int_0^L \phi_v \phi_v dx = \frac{9m}{L^6} \int_0^L \left( \frac{1}{2}Lx^2 - \frac{1}{6}x^3 \right)^2 dx \\ &= \frac{9m}{L^6} \int_0^L \left( \frac{1}{2}Lx^2 - \frac{1}{6}x^3 \right)^2 dx \\ &= \frac{9m}{L^6} \int_0^L \left( \frac{1}{4}L^2x^4 - \frac{2}{12}Lx^5 + \frac{1}{36}x^6 dx \right) \\ &= \frac{9m}{L^6} \left[ \frac{1}{20}L^2x^5 - \frac{2}{72}Lx^6 + \frac{1}{252}x^7 \right]_0^L \\ &= \frac{99}{420}mL \end{aligned}$$

$$\begin{aligned} m_\theta &= \rho A \int_0^L \phi_\theta \phi_\theta dx = \frac{9m}{L^2} \int_0^L \left( \frac{x^2}{2} - \frac{x^3}{6L} - \frac{L}{3}x \right)^2 dx \\ &= \frac{9m}{L^2} \int_0^L \left( \frac{x^2}{2} - \frac{x^3}{6L} - \frac{L}{3}x \right) \left( \frac{x^2}{2} - \frac{x^3}{6L} - \frac{L}{3}x \right) dx \\ &= \frac{9m}{L^2} \int_0^L \left( \frac{1}{4}x^4 - \frac{1}{12L}x^5 - \frac{1}{6}x^3L - \frac{1}{12L}x^5 + \frac{1}{36L^2}x^6 \right. \\ &\quad \left. + \frac{1}{18}x^4 - \frac{1}{6}x^3 + \frac{1}{18}x^4 + \frac{1}{9}L^2x^2 \right) dx \\ &= \frac{9m}{L^2} \left[ \frac{13}{180}x^5 - \frac{1}{36L}x^6 - \frac{1}{12}x^4 + \frac{1}{252L^2}x^7 + \frac{1}{27}x^3L^2 \right]_0^L \\ &= \frac{2}{105}mL^3 \end{aligned}$$

---


$$\begin{aligned}
m_{v\theta} &= m_{\theta v} = \rho A \int_0^L \phi_\theta \phi_v dx \\
&= \left(\frac{3}{L^3}\right) \left(\frac{-3}{L}\right) m \int_0^L \left(\frac{x^2 L}{2} - \frac{x^3}{6}\right) \left(\frac{x^2}{2} - \frac{x^3}{6L} - \frac{Lx}{3}\right) dx \\
&= \frac{-9m}{L^4} \int_0^L \left(\frac{7^L x^4}{36} - \frac{x^5 L}{6} - \frac{x^3 L^2}{6} + \frac{x^6}{36L}\right) dx \\
&= \left(\frac{-9m}{L^4}\right) \left[\frac{x^5 L}{20} - \frac{x^6}{72} - \frac{x^4 L^2}{24} - \frac{x^6}{72} + \frac{x^7}{252L} - \frac{x^5 L}{90}\right]_0^L \\
&= \frac{67}{280} L^2
\end{aligned}$$

### Frequency response function

First, the load is expressed on compact form:

$$F_0 \cos(\omega t + \theta) = \text{Re}[(X_R + iX_I)(\cos(\omega t) + i\sin(\omega t))] = \text{Re}[X \cdot e^{i\omega t}]$$

$$X_R = F_0 \cos(\theta)$$

$$X_I = F_0 \sin(\theta)$$

The response also needs to be a harmonic function:

$$u = \text{Re}[u_0 e^{i\omega t}]$$

$$\dot{u} = \text{Re}[i\omega u_0 e^{i\omega t}]$$

$$\ddot{u} = \text{Re}[-\omega^2 u_0 e^{i\omega t}]$$

The equation of motion given in 2.43 can now be rewritten:

$$\begin{aligned}
m\ddot{u} + c\dot{u} + ku &= F(t) \\
(-m\omega^2 + ic\omega + k)u_0 e^{i\omega t} &= X e^{i\omega t} \\
(-m\omega^2 + ic\omega + k)u_0 &= X \\
u_0 &= \underbrace{(-m\omega^2 + ic\omega + k)^{-1}}_{H(\omega)} X
\end{aligned}$$

The result is the frequency response function:

---


$$\begin{aligned}
H(\omega) &= (-m\omega^2 + ic\omega + k)^{-1} \\
&= (m\omega_n^2 - m\omega^2 + i\omega(2m\omega_n\zeta))^{-1} \\
&= \frac{1}{m}(\omega_n^2 - \omega^2 + i\omega(2\omega_n\zeta))^{-1} \\
&= \frac{1}{m\frac{1}{\omega_n^2}(\omega_n^2 - \omega^2 + i\omega(2\omega_n\zeta))} \\
&= \frac{1}{k(1 - \beta^2 + i(2\zeta\beta))}
\end{aligned}$$

Above, the following relations are introduced:

$$\zeta = \frac{c}{2m\omega_n} \qquad \omega_0^2 = \frac{k}{m} \qquad \beta = \frac{\omega}{\omega_n}$$

For a given load  $F(t) = \text{Re}[X \cdot e^{i\omega t}]$ , the response will be:

$$u_0 = |H(\omega)| \cdot |X|$$

---

## B Python code

import\_data.py

```
#-----  
#Purpose: Importing raw data from Excel files.  
#-----  
#Input parameters:  
#Directory: File location  
#Filename: file name  
#sensor: Identification of acceleration sensor  
#          and strain gauges  
  
import pandas as pd  
import numpy as np  
  
def import_data(directory,filename,sensor):  
    direct=directory + filename  
    print(direct)  
    time=pd.read_excel(direct, header=38,usecols='A')  
    time_n=time.to_numpy()  
  
    if sensor =='acc_vert':  
        data=pd.read_excel(direct,header=38,usecols='B')  
        data_n=data.to_numpy()  
  
    if sensor =='acc_hor_top':  
        data=pd.read_excel(direct,header=38,usecols='C')  
        data_n=data.to_numpy()  
  
    if sensor =='acc_hor_bot':  
        data=pd.read_excel(direct,header=38,usecols='D')  
        data_n=data.to_numpy()  
  
    if sensor=='sg1':  
        data=pd.read_excel(direct,header=38,usecols='S')  
        data_n=data.to_numpy()  
  
    if sensor=='sg2':  
        data=pd.read_excel(direct,header=38,usecols='T')  
        data_n=data.to_numpy()  
  
    if sensor=='sg3':  
        data=pd.read_excel(direct,header=38,usecols='U')  
        data_n=data.to_numpy()  
  
    if sensor=='sg4':
```



---

```
data=pd.read_excel(direct,
                   header=38,usecols='V')
data_n=data.to_numpy()

if sensor=='sg5':
    data=pd.read_excel(direct,
                       header=38,usecols='W')
    data_n=data.to_numpy()

if sensor=='sg6':
    data=pd.read_excel(direct,header=38,usecols='X')
    data_n=data.to_numpy()

if sensor=='sg7':
    data=pd.read_excel(direct,header=38,usecols='Y')
    data_n=data.to_numpy()

if sensor=='sg8':
    data=pd.read_excel(direct,header=38,usecols='Z')
    data_n=data.to_numpy()

if sensor=='sg9':
    data=pd.read_excel(direct,header=38,usecols='AA')
    data_n=data.to_numpy()

if sensor=='sg10':
    data=pd.read_excel(direct,header=38,usecols='AB')
    data_n=data.to_numpy()

if sensor=='sg11':
    data=pd.read_excel(direct,header=38,usecols='AC')
    data_n=data.to_numpy()

dataset=np.hstack((time_n,data_n))
return dataset
```

---

## lowpass\_filter.py

```
#-----#
#Purpose: Establish lowpass filter and filter data
# Source: https://www.delftstack.com/howto/python/low-pass-filter-python/
#
# Downloaded: 02.02.2022
#-----#
#Input parameters:
#data: raw data sample
#cutoff: cutof frequency of filter
#fs: samplerate
#order: order of polynomial

#-----#

from scipy.signal import find_peaks,butter, lfilter

#-----Lowpass filter-----
def butter_lowpass(cutoff,fs,order):
    nyq=0.5*fs
    normal_cutoff=cutoff/nyq
    b, a=butter(order,normal_cutoff,btype='low',analog=False)
    return b, a

def butter_lowpass_filter(data, cutoff, fs, order):
    b, a = butter_lowpass(cutoff, fs, order=order)
    y = lfilter(b, a, data)
    return y
```

---

## static\_deflection.py

```
#-----#
#Purpose: Calculate analytical deflection for
# a cantilever beam and corresponding strain. Gather and
#calculate the average mean static strain. Calculate the
# rotational stiffness from measurements.
#-----#

import numpy as np
from matplotlib import pyplot as plt
from import_data import *
from lowpass_filter import *

cutoff = 100      #cutoff frequency
order = 8        # Order of ploynomial in filter
#filter and find mean from measurments
def mean_deflection(directory,file,sensor, cutoff,samplerate,order):
    #Raw data from experiments
    data=import_data(directory,file,sensor)

    #Lowpass filter
    data_low=butter_lowpass_filter(data[:,1],cutoff,samplerate,order)
    #Find mean of filtered signal
    mean_deflect=np.mean(data_low)
    return mean_deflect

res_point=np.zeros([4,1]) #Results, weld configuration 1
res_full=np.zeros([4,1]) #Results, weld configuration 2

#Files with raw data, weld configuration 1
file_point_weld_0=['','']
file_point_weld_1=['','']
file_point_weld_2=['','']
file_point_weld_3=['','']

#Files with raw data, weld configuration 2
file_full_weld_0=['','']
file_full_weld_1=['','']
file_full_weld_2=['','']
file_full_weld_3=['','']

#Calculate mean deflection for all weights, weld configuration 1
for i in file_point_weld_0:
    mean=mean_deflection(directory,i,sensor,cutoff,samplerate,order)
    res_point[0,0]+=mean

for i in file_point_weld_1:
```

---

```

    mean=mean_deflection(directory,i,sensor,cutoff,samplerate,order)
    res_point[1,0]+=mean

for i in file_point_weld_2:
    mean=mean_deflection(directory,i,sensor,cutoff,samplerate,order)
    res_point[2,0]+=mean

for i in file_point_weld_3:
    mean=mean_deflection(directory,i,sensor,cutoff,samplerate,order)
    res_point[3,0]+=mean

#Mean strain of experimental results [-]
res_point_mean=res_point/len(file_point_weld_0)

#Calculate mean deflection for all weights, weld configuration 2
for i in file_full_weld_0:
    mean=mean_deflection(directory,i,sensor,cutoff,samplerate,order)
    res_full[0,0]+=mean

for i in file_full_weld_1:
    mean=mean_deflection(directory,i,sensor,cutoff,samplerate,order)
    res_full[1,0]+=mean

for i in file_full_weld_2:
    mean=mean_deflection(directory,i,sensor,cutoff,samplerate,order)
    res_full[2,0]+=mean

for i in file_full_weld_3:
    mean=mean_deflection(directory,i,sensor,cutoff,samplerate,order)
    res_full[3,0]+=mean

#Mean strain of experimental results [-]
res_full_mean=res_full/len(file_full_weld_0)

Weights=np.array([0.00001,2.43,4.87,7.26]) #Weights [kg]
#Note. First element in the array above is
#set to a small value to avoid dividing by zero

#-----Calculation of strains at flange-----#
load=Weights*9.81 #Force from weights [N]

EI=2.079*10**6 #Bending stiffness [Nm4]

length=1.512 #Lenght of beam [m]

#Placement of strain gauge on top flange[m]
placement_weight=length-0.4

```

---

---

```

#Analytical strain at top flange[-]
strain=((0.08/EI)*placement_weight*load)

print('Analytical strain',strain)
print('Measured strain',res_point*10**-6)#print with conversion
#to microstrain

#-----End deflection-----#
#Analytical end deflection
end_deflection=np.array(((length**3)/(3*EI))*load)#[m]
#measured end deflection, weld configuration 1[10^-6 m]
measured_deflection=np.array([(0+2+0)/3,(20+22+20)/3,\
(54+53+45)/3,(74+64+64)/3])
#Measured end deflection, weld configuration 2[10^-6 m]
measured_deflection_full=np.array([0.001,(20+18+17)/3,\
(36+35+34)/3,(55+52+51)/3])

#-----Beam stiffness-----#

#Analytical stiffness[N/m]
stiffness=np.divide((load*length**2),end_deflection)

#Measured stiffness, weld configuration 1[N/m]
stiffness_measured=np.divide((load*length**2),\
measured_deflection*10**-6)

#Measured stiffness weld configuration 2[N/m]
stiffness_measured_full=np.divide((load*length**2),\
measured_deflection_full*10**-6)

rot_stiffness_calculated=np.zeros(len(load))
rot_stiffness_measured=np.zeros(len(load))
rot_stiffness_measured_new=np.zeros(len(load))

#Measured rotational stiffness[N/theta]
for i in range(len(stiffness)):
    rot_stiffness_measured[i]=stiffness_measured[i]-(3*EI)/length

```

---

## Eigenfrequency.py

```
from cmath import pi
import numpy as np
import math
EI=2.079*10**6 #[Nm^2]
l=1.53 #[m]
l_e=l-0.2 #[m], placement of motor
m_e=19.2 #[kg]
m=7850*2008*10**(-6) #[kg/m]

kr=1488010

#rotational stiffness [N/rad]
K=np.array([[EI*(l**3))/3, ((l**2)*EI)/6],
            [((l**2)*EI)/6, ((EI*l)/3)+kr]])

M_tot=(m*l*99/420)+m_e
M_coupling=(67/280)*m*l**2
I=m*(2/105)*l**3
#(121/840)*l**3

M=np.array([[M_tot,M_coupling],[M_coupling,I]])

omega_power_1=((K[0,0]*M[0,0]+I*K[1,1])- \
math.sqrt((K[0,0]*M_tot+I*K[1,1])**2-\
4*M_tot*I*(K[0,0]*K[1,1]-K[0,1]*K[1,0]))) \
/(2*M_tot*I)

omega1=math.sqrt(omega_power_1)

f1=omega1/(2*pi)

omega_power_2=((K[0,0]*M_tot+I*K[1,1])+ \
math.sqrt((K[0,0]*M_tot+I*K[1,1])**2-\
4*M_tot*I*(K[0,0]*K[1,1]-K[0,1]*K[1,0]))) \
/(2*M_tot*I)

omega2=math.sqrt(omega_power_2)
#print(4*EI/l)

f2=omega2/(2*pi)
print("Stiffness matrix:", K)
print("Lumped mass matrix:",M)
print("First eigenfrequency 2DOF:",f1)
print("Second eigenfrequency 2DOF:",f2)

#print(math.sqrt((3*EI)/(m_e*(l**3)))/6.28)
```

---

```
#print(3.5186*math.sqrt((EI)/(m*l**4))/6.28)
```

## logarithmic\_decrement.py

```
#-----#
#Purpose: Calculate damping from experimental results
#using the logarithmic decrement.
#-----#

import math
from cmath import pi
import numpy as np
from matplotlib import pyplot as plt
from import_data import *
from lowpass_filter import *
from scipy.signal import find_peaks

#Find the peaks and time of peak in array
def peaks(time_series,displacement):
    peaks=find_peaks(displacement)
    time=np.zeros(len(peaks[0]))
    res=np.zeros(len(peaks[0]))
    index=0
    for i in peaks[0]:
        res[index]=displacement[i]
        time[index]=time_series[i]
        index+=1
    return time,res

#Find only positive values of time series
def pos_values(time,dataset):
    time_raw_tot=np.zeros((len(time)))
    res_raw_tot=np.zeros((len(dataset)))
    idx=0
    for t,i in enumerate(dataset):
        if i<=0:
            continue
        res_raw_tot[idx]=i
        time_raw_tot[idx]=time[t]
        idx+=1
    res_raw=np.trim_zeros(res_raw_tot)
    time_raw=np.trim_zeros(time_raw_tot)
    return time_raw,res_raw

#Calculating logarithmic damping from given sample
def log_damping(n,sample):
```

---

```

    i_max=np.argmax(sample)
    sample1=sample[i_max+2]
    sample2=sample[i_max+n+2]
    decrement=(1/n)*(np.log(sample1)/np.log(sample2))
    damping=1/(np.sqrt((1+((2*pi)/decrement)**2)))
    return i_max,damping

cutoff = 100      #cutoff frequency
fs = 1200.0      # sample rate, Hz
order = 8        # Order of ploynomial in filter

n=np.arange(5,35) #Number of peaks to count in decrement

#preallocation of arrays
damping_res=np.zeros([len(n)])
natural_frequency=np.zeros([len(files),1])
natural_frequency_rot=np.zeros([len(files),2])
max_strain=np.zeros([len(files),1])

#Import and filter data. Afterwards peaks are identified.
dataset=import_data(directory,file,'acc_vert')
res_lowpass=butter_lowpass_filter(dataset[:,1],cutoff,fs,order)
time_low,res_low=pos_values(dataset[:,0],res_lowpass)
time_peaks_low,res_peaks_low=peaks(time_low,res_low)

i_max_vert=np.argmax(res_peaks_low)#Identify largest peak

for idx, i in enumerate(n):
    i_max, damping=log_damping(i,res_peaks_low)
    damping_res[idx]=damping

strains_res=import_data(directory,file,'sg11')
strains_low=butter_lowpass_filter(strains_res[:,1],cutoff,fs,order)

max_strain=np.amax(strains_low)

#Convergence of damping ratios are found.
for i in range(len(files)):
    for idx, j in enumerate(damping_res[:,i]):
        if 0.95<=damping_res[idx-1]/i <=1.05:
            print('Coverged at: ',n[idx])
            print('Damping: ',damping_res[idx,i])
            break

```

---



---

## Half\_power.py

```
#-----#
#Purpose: Calculate damping from experimental results using
#the logarithmic decrement.
#-----#

import numpy as np
import math
from scipy.signal import find_peaks
import matplotlib.pyplot as plt
from import_data import *
from lowpass_filter import *

#find the response for given load frequency.
def frequency_results(frequencies,dataset,dataset_lowpass):
    m=0
    res=np.zeros((len(dataset[:,1]),len(frequencies[:,0])))
    for count, j in enumerate(frequencies[:,0]):
        for idx,i in enumerate(dataset[:,0]):
            if frequencies[count,1]<= i <=frequencies[count,2]:
                res[m,count]=dataset_lowpass[idx]
                m+=1
    return res

#find peaks or response
def peaks_find(peaks,dataset,data_lowpass):
    idx=0
    peaks_plot=np.empty((len(peaks[0]),2))
    for i in peaks[0]:
        peaks_plot[idx,0]=dataset[i,0]
        peaks_plot[idx,1]=data_lowpass[i]
        idx+=1
    return peaks_plot

#find amplitude of response
def find_amp(frequencies, res):
    append=np.zeros((len(frequencies[:,0]),1))
    tot_res=np.hstack((frequencies,append))
    for idx,i in enumerate(frequencies[:,0]):
        max=np.amax(res[:,idx])
        min=np.amin(res[:,idx])
        amp=(np.abs(max)+np.abs(min))/2
        tot_res[idx,3]=amp
    return tot_res

#find halfpower given frequencies
def find_halfpower(tot_res,half_power):
```

---

---

```

for i in range(len(tot_res[:,3])):
    if tot_res[(i-1),3] < half_power <= tot_res[i,3]:
        freq_1=(tot_res[(i-1),0]*(tot_res[i,3]-half_power) \
+tot_res[(i),0]* \
(half_power-tot_res[(i-1),3]))/(tot_res[(i),3]\
-tot_res[(i-1),3])

    elif tot_res[(i-1),3] > half_power >= tot_res[i,3]:
        freq_2=(tot_res[(i-1),0]*(tot_res[i,3]-half_power) \
+tot_res[(i),0]* \
(half_power-tot_res[(i-1),3]))/(tot_res[(i),3] \
-tot_res[(i-1),3])
return freq_1,freq_2

```

```

directory=''#directory where result files are stored.

```

```

#Import data from excel file. The time of different frequencies are
#loaded from separate text file.

```

```

def calc_damping_halfpower(sensor):
    file=''#.txt file with time of different frequencies
    dataset=import_data(directory,file_1,sensor) #Import data
    frequencies=np.loadtxt("", skiprows=1, dtype='float')#import
    #frequencies from text file.

```

```

#Lowpass filter requirements.

```

```

order = 8 # Order of ploynomial in filter
fs = 1200.0 # sample rate, Hz
cutoff = 100 # desired cutoff frequency of the filter, Hz

```

```

data_lowpass=butter_lowpass_filter(dataset[:,1], cutoff, fs, order)

```

```

#Finding steady state for each frequency and saving the response.
res=frequency_results(frequencies,dataset,data_lowpass)

```

```

#Find the amplitude at at given load frequency
tot_res=find_amp(frequencies,res)

```

```

#Find max response in order to calculate half-power point

```

```

max_amp=np.amax(tot_res[:,3])
half_power=max_amp/math.sqrt(2)
resonance_idx=np.argmax(tot_res[:,3])
resonance=tot_res[resonance_idx,0]

```

```

#Use linear interpolation to find the other frequencies
freq_1,freq_2=find_halfpower(tot_res,half_power)

```

---

```

    #Find the damping ratio
    damping=(freq_2-freq_1)/(2*resonance)

    return damping, tot_res,freq_1,freq_2,half_power

damping_sg11,tot_res_sg11,freq_1_sg11,freq_2_sg11, \
half_power_vert=calc_damping_halfpower('sg11')

E=210*10**3 #Youngs modulus steel[MPa]

micro_strain=np.zeros(len(tot_res_sg11[:,1])) #Preallocation

micro_strain[:,0]=tot_res_sg11[:,3]

stress=micro_strain*E*10**-6 #Find stress if sensor i strain gauge[MPa]
frequencies=tot_res_sg11[:,0] #[Hz]

num_rows,num_cols=stress.shape
max_stress=np.zeros(num_cols)

for i in range(len(max_stress)):
    max_stress[i]=np.amax(stress[:,i])

max_freq_i_1=np.argmax(tot_res_sg11[:,3])

```

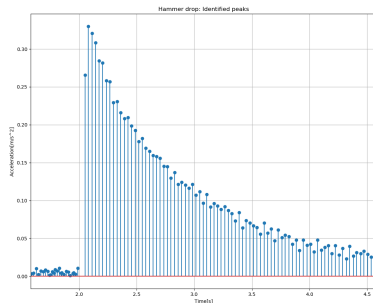
---

## C Experimental results

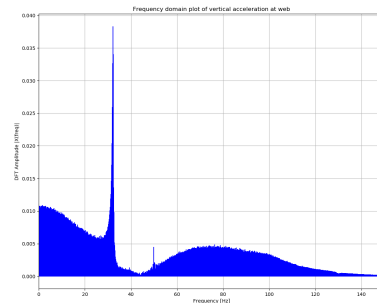
### Logarithmic decrement

n	Test 1, $\zeta[-]$	Test 2, $\zeta[-]$	Test 3, $\zeta[-]$
5	0.02541141	0.02644074	0.02671619
6	0.02126197	0.0211063	0.02212001
7	0.01746185	0.01742792	0.01857339
8	0.01491345	0.01441006	0.01527911
9	0.01331306	0.01260622	0.01351747
10	0.01158739	0.01078992	0.01166679
11	0.01034073	0.00984072	0.01098909
12	0.00903513	0.00876729	0.00947638
13	0.00845015	0.00791016	0.00849714
14	0.00753031	0.00721178	0.00797305
15	0.00693144	0.00646561	0.00699313
16	0.00637800	0.0062171	0.00678062
17	0.00597521	0.00551559	0.00609886
18	0.00559839	0.00536556	0.0057664
19	0.00511157	0.00463888	0.00527782
20	0.00484383	0.00453943	0.00494468
21	0.00436192	0.00418012	0.00455536
22	0.00428516	0.00393644	0.00434563
23	0.00385865	0.0037307	0.00407786
24	0.00373801	0.00354866	0.00377255
25	0.0035413	0.00335155	0.00377727
26	0.00334601	0.00307001	0.0034763
27	0.00328699	0.00308447	0.00325388
28	0.00299183	0.00282373	0.00301157
29	0.00294867	0.00268684	0.00305522

Table C.1: Convergence, weld configuration 1

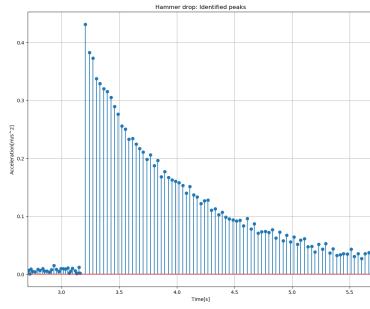


(a) Identified peaks

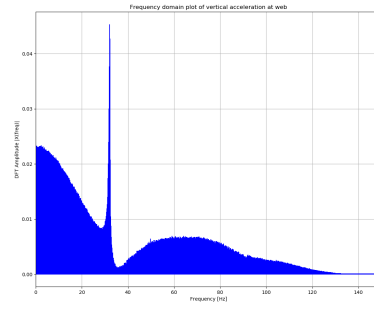


(b) Frequency domain plot of acceleration

Figure C.1: Weld configuration 1, test 1

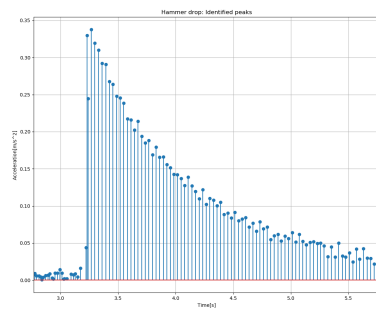


(a) Identified peaks

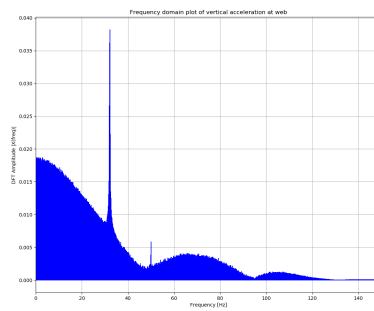


(b) Frequency domain plot of acceleration

Figure C.2: Weld configuration 1, test 2

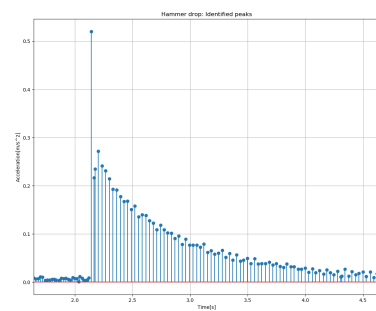


(a) Identified peaks

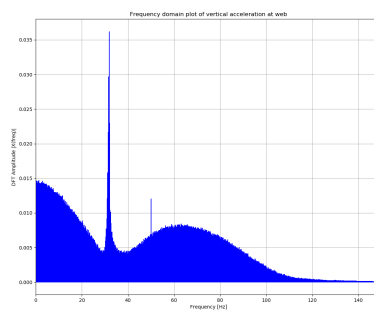


(b) Frequency domain plot of acceleration

Figure C.3: Weld configuration 1, test 3

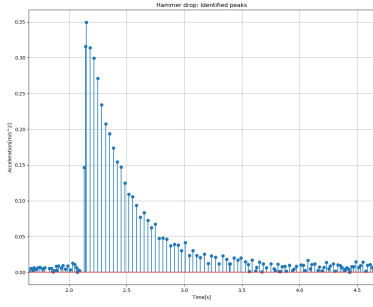


(a) Identified peaks

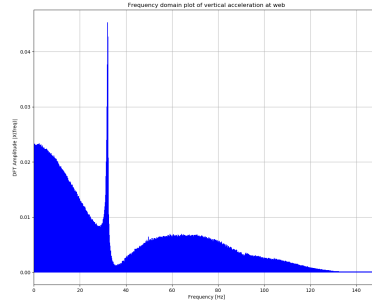


(b) Frequency domain plot of acceleration

Figure C.4: Weld configuration 1, test 4

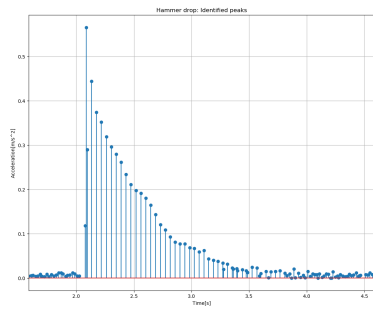


(a) Identified peaks

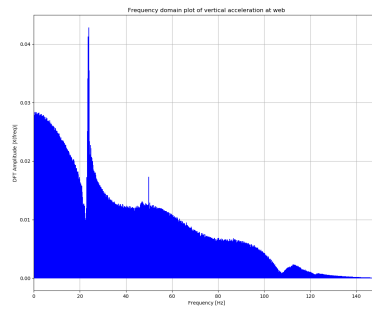


(b) Frequency domain plot of acceleration

Figure C.5: Weld configuration 1, test 5

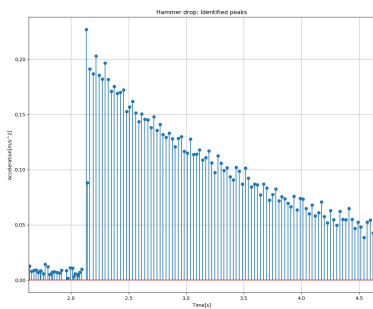


(a) Identified peaks

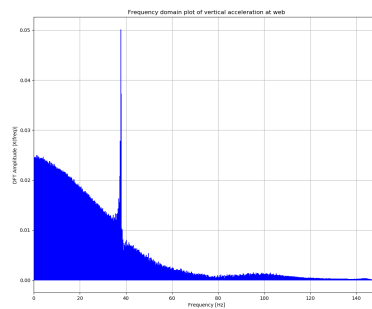


(b) Frequency domain plot of acceleration

Figure C.6: Weld configuration 1, test 6

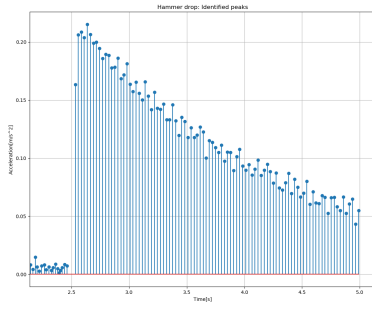


(a) Identified peaks

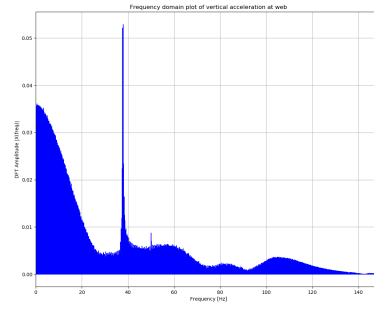


(b) Frequency domain plot of acceleration

Figure C.7: Weld configuration 2, test 1

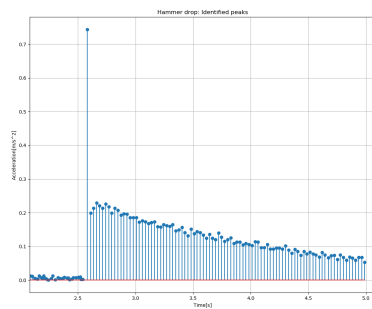


(a) Identified peaks

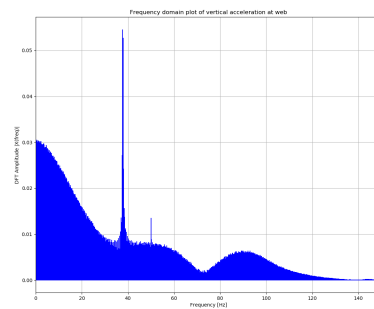


(b) Frequency domain plot of acceleration

Figure C.8: Weld configuration 2, test 2

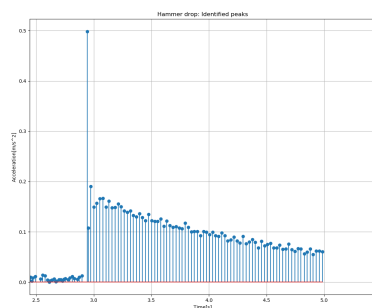


(a) Identified peaks

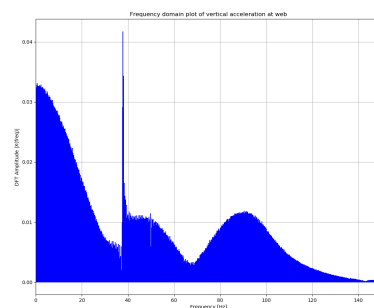


(b) Frequency domain plot of acceleration

Figure C.9: Weld configuration 2, test 3

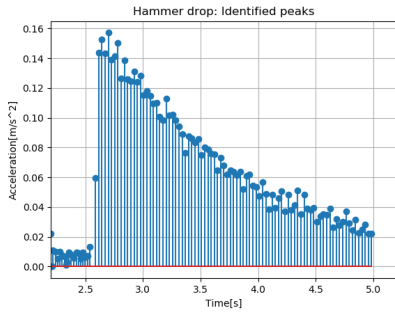


(a) Identified peaks

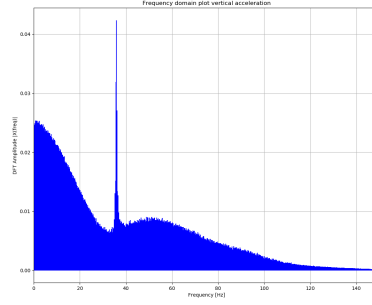


(b) Frequency domain plot of acceleration

Figure C.10: Weld configuration 2, test 4

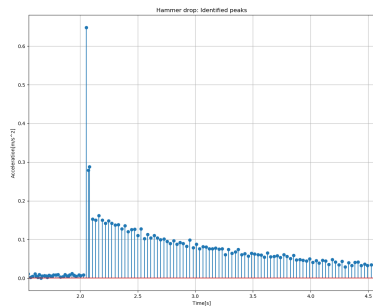


(a) Identified peaks

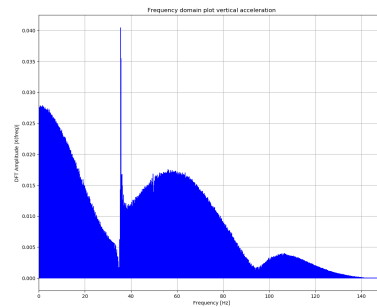


(b) Frequency domain plot of acceleration

Figure C.11: Weld configuration 2, test 5

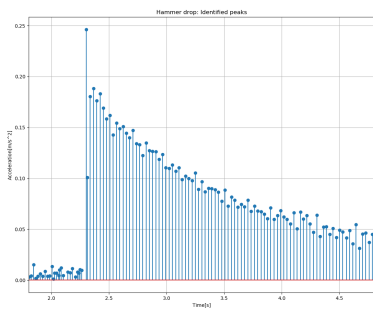


(a) Identified peaks

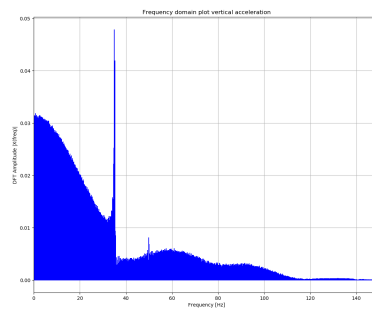


(b) Frequency domain plot of acceleration

Figure C.12: Weld configuration 2, test 6



(a) Identified peaks

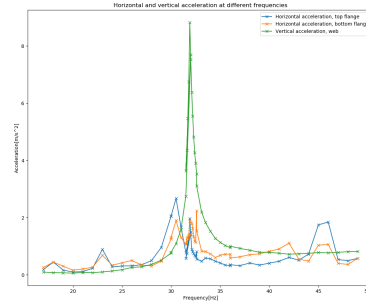
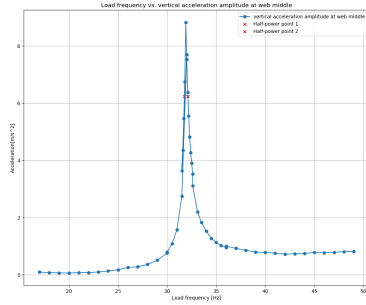


(b) Frequency domain plot of acceleration

Figure C.13: Weld configuration 2, test 7

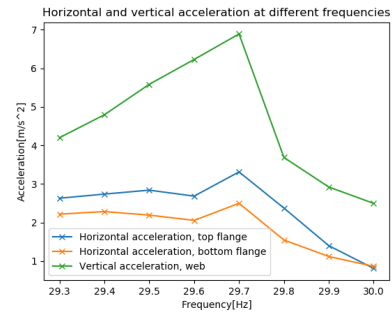
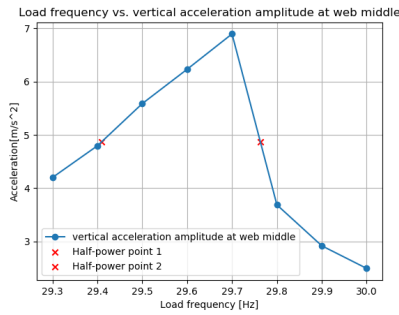


## Half-power point method



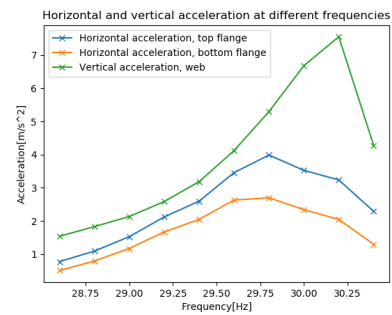
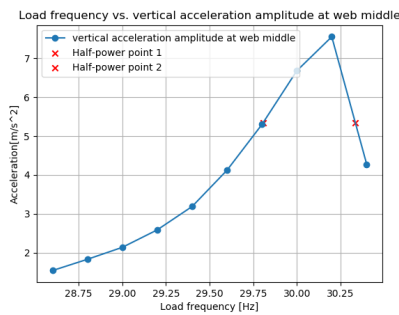
(a) Vertical acceleration amplitude at web (b) vertical -and horizontal acceleration

Figure C.14: Weld configuration 1, test 2



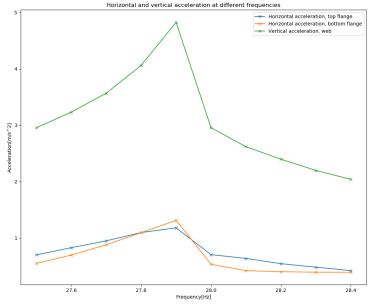
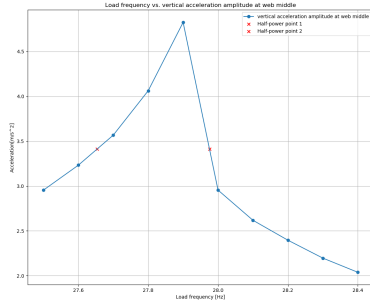
(a) Vertical acceleration amplitude at web (b) vertical -and horizontal acceleration

Figure C.15: Weld configuration 1, test 3



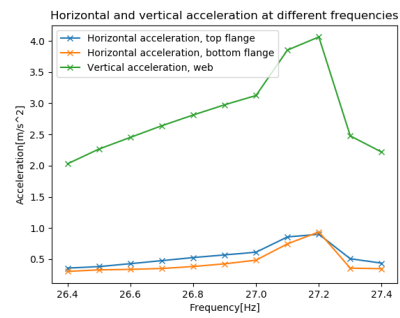
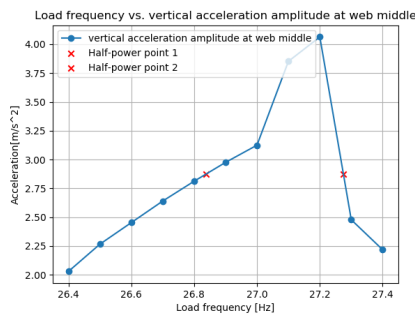
(a) Vertical acceleration amplitude at web (b) vertical -and horizontal acceleration

Figure C.16: Weld configuration 1, test 4



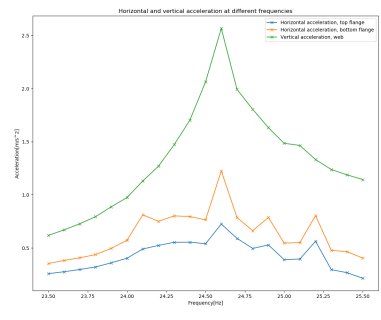
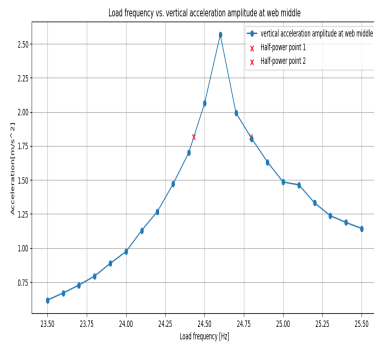
(a) Vertical acceleration amplitude at web      (b) vertical -and horizontal acceleration

Figure C.17: Weld configuration 1, test 5



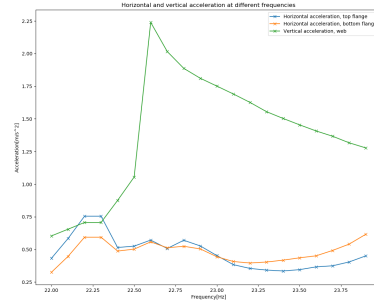
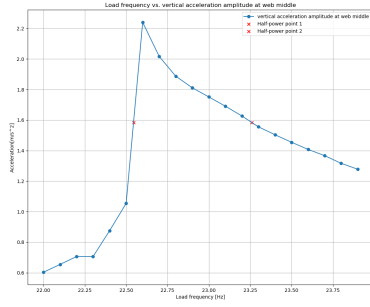
(a) Vertical acceleration amplitude at web      (b) vertical -and horizontal acceleration

Figure C.18: Weld configuration 1, test 6



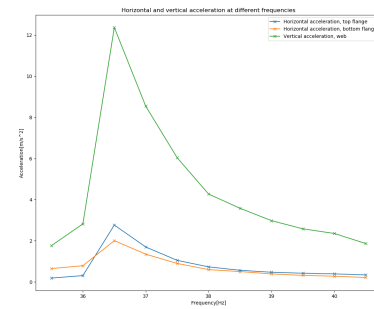
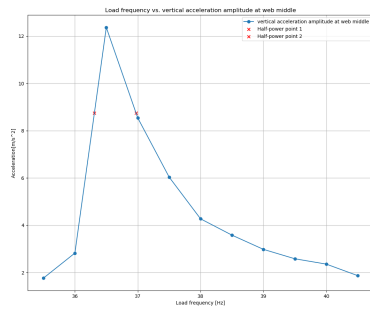
(a) Vertical acceleration amplitude at web      (b) vertical -and horizontal acceleration

Figure C.19: Weld configuration 1, test 7



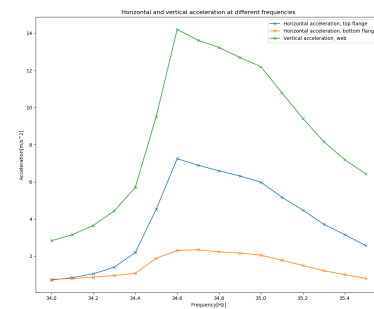
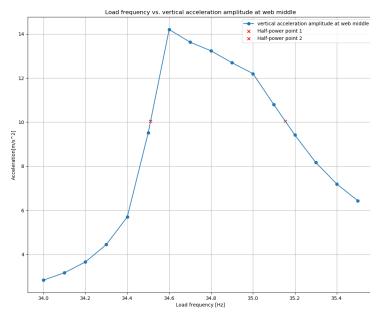
(a) Vertical acceleration amplitude at web (b) vertical -and horizontal acceleration

Figure C.20: Weld configuration 1, test 8



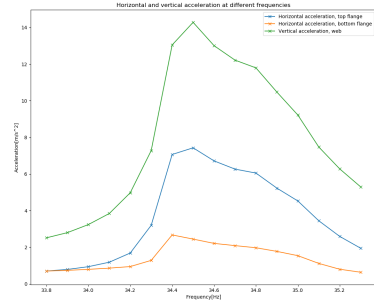
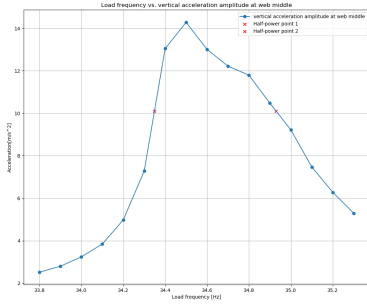
(a) Vertical acceleration amplitude at web (b) vertical -and horizontal acceleration

Figure C.21: Weld configuration 2, test 1



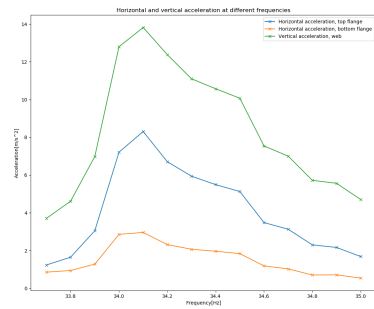
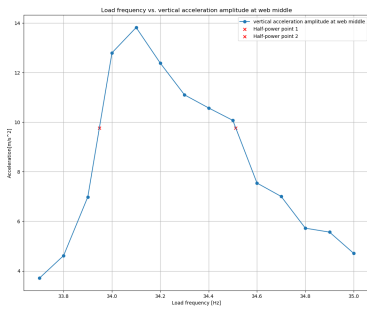
(a) Vertical acceleration amplitude at web (b) vertical -and horizontal acceleration

Figure C.22: Weld configuration 2, test 2



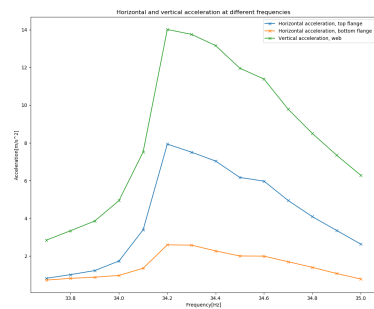
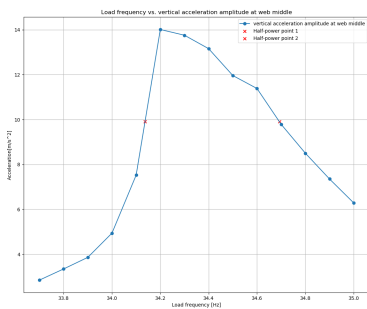
(a) Vertical acceleration amplitude at web (b) vertical -and horizontal acceleration

Figure C.23: Weld configuration 2, test 3



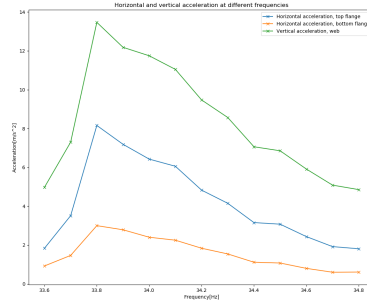
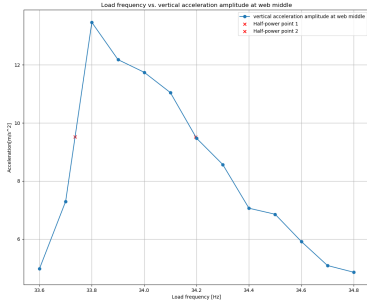
(a) Vertical acceleration amplitude at web (b) vertical -and horizontal acceleration

Figure C.24: Weld configuration 2, test 4



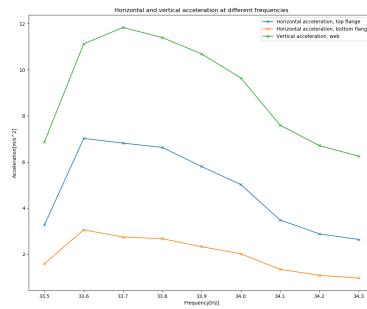
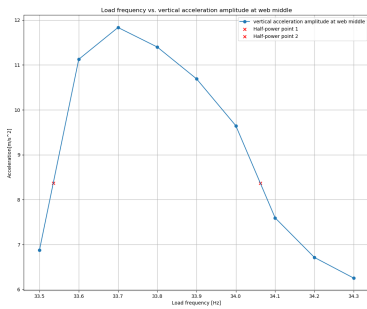
(a) Vertical acceleration amplitude at web (b) vertical -and horizontal acceleration

Figure C.25: Weld configuration 2, test 5



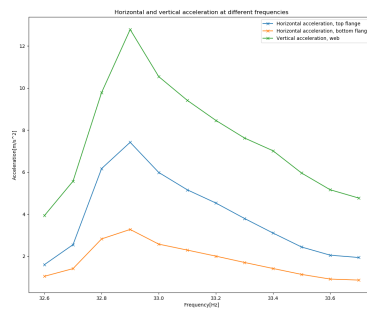
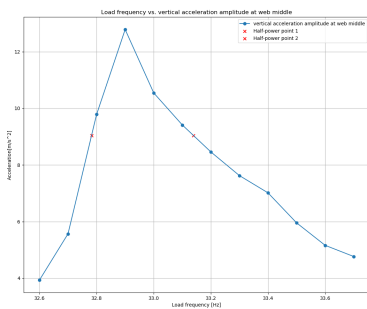
(a) Vertical acceleration amplitude at web (b) vertical -and horizontal acceleration

Figure C.26: Weld configuration 2, test 6



(a) Vertical acceleration amplitude at web (b) vertical -and horizontal acceleration

Figure C.27: Weld configuration 2, test 7



(a) Vertical acceleration amplitude at web (b) vertical -and horizontal acceleration

Figure C.28: Weld configuration 2, test 8

